

UNIVERSITY OF LJUBLJANA
FACULTY OF MATHEMATICS AND PHYSICS
DEPARTMENT OF PHYSICS

Tinkara Troha

**Ultraviolet second harmonic generation in
structured AlN optical waveguides**

Doctoral thesis

Advisor: prof. dr. Marko Zgonik

Ljubljana, 2017

UNIVERZA V LJUBLJANI
FAKULTETA ZA MATEMATIKO IN FIZIKO
ODDELEK ZA FIZIKO

Tinkara Troha

**Frekvenčno podvojevanje svetlobe v
strukturiranih AlN optičnih valovodih v
ultravijoličnem spektralnem območju**

Doktorska disertacija

Mentor: prof. dr. Marko Zgonik

Ljubljana, 2017

Univerza v Ljubljani
Fakulteta za matematiko in fiziko

Izjava o avtorstvu, istovetnosti tiskane in elektronske verzije doktorske disertacije in
objavi osebnih podatkov študentke

Spodaj podpisana študentka

avtorica **doktorske disertacije** (v nadaljevanju: pisnega zaključnega dela študija) z naslovom:

IZJAVLJAM

1. *Obkrožite eno od variant a) ali b)*

- a) da sem pisno zaključno delo študija izdelala samostojno;
- b) da je pisno zaključno delo študija rezultat lastnega dela več kandidatov in izpolnjuje pogoje, ki jih Statut UL določa za skupna zaključna dela študija ter je v zahtevanem deležu rezultat mojega samostojnega dela;

pod mentorstvom

- 2. da je tiskana oblika pisnega zaključnega dela študija istovetna elektronski obliki pisnega zaključnega dela študija;
- 3. da sem pridobila vsa potrebna dovoljenja za uporabo podatkov in avtorskih del v pisnem zaključnem delu študija in jih v pisnem zaključnem delu študija jasno označila;
- 4. da sem pri pripravi pisnega zaključnega dela študija ravnala v skladu z etičnimi načeli in, kjer je to potrebno, za raziskavo pridobila soglasje etične komisije;
- 5. da soglašam, da se elektronska oblika pisnega zaključnega dela študija uporabi za preverjanje podobnosti vsebine z drugimi deli s programsko opremo za preverjanje podobnosti vsebine, ki je povezana s študijskim informacijskim sistemom fakultete;
- 6. da na UL neodplačno, neizključno, prostorsko in časovno neomejeno prenašam pravico shranitve avtorskega dela v elektronski obliki, pravico reproduciranja ter pravico dajanja pisnega zaključnega dela študija na voljo javnosti na svetovnem spletu preko Repozitorija UL;
- 7. [za zaključna dela na 3. stopnji študija, sestavljena iz člankov] da sem od založnikov, na katere sem predhodno izključno prenesla materialne avtorske pravice na člankih, pridobila potrebna soglasja za vključitev člankov v tiskano in elektronsko obliko disertacije. Soglasja UL omogočajo neodplačno, neizključno, prostorsko in časovno neomejeno hranjenje avtorskega dela v elektronski obliki in reproduciranje ter dajanje disertacije na voljo javnosti na svetovnem spletu preko Repozitorija UL;
- 8. da dovoljujem objavo svojih osebnih podatkov, ki so navedeni v pisnem zaključnem delu študija in tej izjavi, skupaj z objavo pisnega zaključnega dela študija.

Kraj:

Podpis študentke:

Datum:

Babici v spomin

Iskreno se zahvaljujem mentorju prof. Marku Zgoniku, da mi je omogočil delo na zanimivem raziskovalnem projektu ter za vodstvo in vzpodbudo pri raziskavah. Za podporo in koristne nasvete pri pisanju disertacije sem hvaležna prof. Ireni Drevenšek. Posebna zahvala gre prof. Normi Mankoč Borštnik, ker si vedno vzame čas za pogovor o kateremkoli fizikalnem problemu. Hvala sodelavcem in članom odseka F7 na Inštitutu Jožef Stefan, ki so mi pomagali pri eksperimentalnem delu in so poskrbeli za prijetno razpoloženje. I would like to thank scientists from NCSU, prof. Z. Sitar, prof. R. Collazo and D. Alden for the exchange of knowledge and our successful collaboration. In nenazadnje, hvala mojim prijateljem in družini za uso ljubezen, ki sem je deležna.

Abstract

Semiconductor nitrides GaN, AlN and mixed AlGaN are considered very promising materials in optoelectronic research fields. Their exceptional property is a wide energy bandgap, which makes it possible to use them both in the visible and ultraviolet spectral range. Typical applications include light detectors, light emitting diodes and lasers. Many efforts have been made towards the fabrication of electrically pumped deep UV laser diodes using the AlGaN system. However challenges in doping, carrier injection and defect control still have to be solved before such applications become widespread.

Within this thesis the potential of AlN for generation of UV light through a non-linear optical process of second harmonic generation (SHG) is investigated. AlN is an excellent candidate since it has a large nonlinear susceptibility and is transparent to 200 nm. High quality thin AlN films can be grown on sapphire substrate forming optical waveguides. The advantage of using waveguides is that light travels without the diffraction, so that high optical intensity needed for efficient SHG is maintained over a long length. The crucial property for achieving high nonlinear conversion efficiency is phase matching between the fundamental and second harmonic waves. Modal dispersion phase matching takes advantage of the fact that waveguide modes of different order obey different dispersion relations. It is achievable that different pump and second harmonic modes have the same propagation constant and therefore phase matching is realized. More interesting approach is quasi phase matching where the phases of the two waves are matched due to the periodicity built into the crystal structure. This is achieved in structured AlN waveguides, where material's crystallographic *c*-axis is periodically inverted and the periodicity determines the conversion wavelength. It enables phase matching along the waveguide between the fundamental waveguide modes of both, pump and second harmonic waves, which leads to the highest attainable conversion efficiency.

Second harmonic generation of short wavelength light in single polar and structured AlN waveguides is presented. The waveguides were produced in North Carolina State University and the nonlinear optical measurements were done in Ljubljana. To explain the experimental results, the appropriate theoretical model was devised based on planar waveguide approximation. Several phase matched peaks in UV spectral region were observed in single polar waveguides in agreement with the theory. By observing second harmonic generation in these waveguides the refractive index dispersion model of AlN was tested, confirming the validity of its extrapolation in the UV range. The first demonstration of SHG into the visible and near UV spectral region was achieved using structured AlN waveguides with 10 μm periodicity. The results and advances obtained during this doctorate study are believed to provide useful information for the fabrication of the highly efficient coherent deep UV light source.

Keywords: AlGaN, optical waveguides, polarity control growth, second harmonic generation, phase matching, end-fire coupling.

PACS: 42.82.-m, 42.65.Ky, 42.65.Wi, 77.55.hd, 78.66.Fd.

Povzetek

Polprevodniki s široko energijsko režo, kot so galijev nitrid (GaN), aluminijev nitrid (AlN) in mešanica AlGaN, so zelo obetavni za uporabo na raziskovalnem področju optoelektronike. Zaradi široke energijske reže so uporabni tako v vidnem kot v ultravijoličnem spektralnem območju. Med pomembnejše aplikacije sodijo detektorji svetlobe, svetleče diode in laserji. Veliko raziskav je usmerjenih v izdelavo električno črpanih laserskih diod v globokem UV območju na podlagi AlGaN sistema. Tehnologija njihove izdelave pa se srečuje z mnogo izzivi, kot so učinkovito dopiranje, dodajanje nosilcev naboja in kontrola defektov, ki zaenkrat še onemogočajo, da bi te aplikacije postale vsesplošno razširjene.

V tem doktorskem delu raziskujem potencial aluminijevega nitrida za generacijo UV svetlobe s pomočjo nelinearnega optičnega procesa, to je optičnega podvajanja frekvence svetlobe. AlN je primeren material, ker ima razmeroma veliko nelinearno susceptibilnost in je prepusten za svetlobo do valovne dolžine 200 nm. Visoko kvalitetne tanke AlN filme lahko gojimo na safirnem substratu, takšna struktura pa za svetlobo tvori optični valovod. Prednost uporabe valovodov je v tem, da svetloba znotraj jedra valovoda potuje brez uklona. Z drugimi besedami, velika intenziteta svetlobe se vzdolž propagacije ohranja, kar je pomembno za učinkovito pretvorbo iz osnovne v frekvenčno podvojeno svetlobo. Najpomembnejša lastnost za učinkovito podvojevanje frekvence pa je fazno ujemanje med osnovnim in podvojenim svetlobnim valom. Fazno ujemanje na podlagi rodovne disperzije je eden od načinov, ki izkorišča dejstvo, da se različni valovodni rodovi propagirajo z različnimi propagacijskimi konstantami. Doseči se da, da se različna rodova pri osnovni in podvojeni frekvenci propagirata z isto propagacijsko konstantno, s čimer dosežemo fazno ujemanje. Drug, bolj zanimiv način, pa je kvazi fazno ujemanje, ki uporabi periodično modulacijo nelinearnega koeficienta v kristalu. S tem dosežemo relativno ujemanje faze v ponavljajočih intervalih, ne da bi se pri tem ujemali fazni hitrosti osnovne in podvojene svetlobe. To dosežemo v strukturiranih AlN valovodih, ki so narejeni tako, da je orientacija kristalografske c-osi vzdolž valovoda periodično invertirana, pri čemer dolžina periode določa frekvenco podvajanja. Ta način omogoča fazno ujemanje med najnižjima rodovoma tako osnovne kot frekvenčno podvojene svetlobe, kar ustreza največjemu izkoristku pretvorbe.

Z uporabo enopolarnih in strukturiranih AlN valovodov smo prikazali frekvenčno podvajanje svetlobe s kratkimi valovnimi dolžinami. Valovodi so bili narejeni v North Carolina State University, meritve nelinearnih optičnih lastnosti pa v Ljubljani. Za razlago eksperimentalnih rezultatov smo uporabili primerne teoretične modele na podlagi približka planarnih valovodov. Z uporabo enopolarnih AlN valovodov smo opazili veliko vrhov v spektru podvojenega valovanja v UV območju, ki se dobro ujemajo s teoretično napovedjo. S tem smo poleg teoretičnega modela preverili in potrdili veljavnost modela disperzije lomnega količnika v AlN kristalu, predvsem njegovo ekstrapolacijo v UV območje. Prvič je bilo demonstrirano frekvenčno podvajanje v vidni in UV del spektra z uporabo strukturiranih AlN valovodov z 10 μm periodo modulacije. Verjamem, da bodo rezultati in napredek pridobljeni tekom nastanka te

doktorske naloge prispevali koristne informacije za izdelavo UV svetlobnih izvorov z visokim izkoristkom.

Ključne besede: AlGaN, optični valovodi, frekvenčno podvajanje svetlobe, fazno ujemanje, sklapljanje svetlobe v valovod s konca.

PACS: 42.82.-m, 42.65.Ky, 42.65.Wi, 77.55.hd, 78.66.Fd.

Contents

1	Introduction	1
1.1	Research objectives	2
1.2	Organization of the dissertation	3
2	Properties and growth of AlN	5
2.1	Material properties	5
2.2	AlN crystal growth	6
3	Optical waveguides	9
3.1	Planar waveguide	9
3.2	TM and TE solutions	11
3.2.1	TM modes	11
3.2.2	TE modes	12
3.3	Losses in optical waveguides	13
4	Second harmonic generation	15
4.1	Nonlinear optics	15
4.2	Second harmonic generation in planar optical waveguides	17
4.3	Modal dispersion phase matching	19
4.4	Quasi phase matching	20
4.4.1	Errors in domain sizes	23
4.5	Second harmonic generation of ultrashort pulses	25
5	Experimental	31
5.1	Laser system	31
5.2	Detection system	32
5.3	Setup	32
6	Second harmonic generation in AlN waveguides	35
6.1	Introduction	35
6.2	Single polar AlN waveguides	35
6.2.1	Measurements	37
6.3	Lateral polar structure-based AlN waveguides	41
6.3.1	Theoretical predictions for 10 μm periodic structured waveguides	41

6.3.2	Topography of the rectangular $10\ \mu\text{m}$ periodic structured waveguides	42
6.3.3	SHG measurements using rectangular $10\ \mu\text{m}$ periodic structured waveguides	46
6.3.4	Measurements using planar $10\ \mu\text{m}$ periodic structured waveguides	51
6.3.5	Theoretical predictions for $1.2\ \mu\text{m}$ periodic structured waveguides	54
6.3.6	Measurements using $1.2\ \mu\text{m}$ periodic structured AlN waveguides	55
6.4	Discussion	56
7	Conclusions	59
8	Extended abstract in Slovene	61
8.1	Uvod	61
8.2	Optični valovodi	62
8.3	Podvajanje svetlobe v optičnih valovodih	64
8.3.1	Fazno ujemanje	65
8.3.2	Meritve frekvenčnega podvajanja v AlN valovodih	66
8.3.3	Zaključek	70

Chapter 1

Introduction

This work is a part of a collaboration project between the Wide-bandgap group at North Carolina State University and University of Ljubljana. The aim of this mutual research effort is to apply knowledge on the nonlinear optics and crystal growth in order to produce a compact laser source emitting in the UV spectral region. A wide variety of possible applications of such UV lasers include water purification, bioagent detection, short-range non-line of sight communications, high density optical data storage, medical diagnosis, UV curing, material processing and more [1–4].

There are many challenges that accompany the technology of lasers emitting UV light, like high threshold pump power, limited choice of transparent and UV-resistant optical materials and the high sensitivity of UV light to material imperfections. Currently available laser systems are either expensive, inefficient, non-portable, large or require frequent maintenance. However, there exist various kinds of ultraviolet lasers which can directly generate UV light: some bulk lasers (e.g. based on cerium-doped crystals such as Ce:LiCAF), fiber lasers (e.g. some low power neodymium-doped fluoride fiber lasers emit at around 380 nm), laser diodes (mostly GaN-based), dye lasers, excimer lasers and free electron lasers [4]. There exist also lasers that access the deep UV wavelengths via frequency multiplication. The solid state, Q-switched Nd-YAG laser together with two nonlinear crystals is used to change the infrared 1064 nm wavelength into the 266 nm wavelength through frequency quadrupling [5]. However, because of the two stage frequency doubling, this system is very inefficient. Furthermore, it requires complex optics and suffers from degradation of the utilized nonlinear crystals due to the very intense UV light, which leads to short lifetimes.

Group III-nitride semiconductors (GaN, AlN and mixed alloy AlGaIn) offer the greatest promise for realizing UV laser sources because of their wide direct optical transition energy covering the region from the near infrared (3.4 eV for GaN) to the deep UV region (6.2 for AlN) [6–9]. In addition, they exhibit excellent physical properties, they are mechanically hard and the devices have long lifetimes. More than two decades passed since a series of fundamental breakthroughs in the area of GaN semiconductor material led to the first demonstration of highly efficient and high brightness blue light emitting diodes (LEDs) [10, 11]. GaN based white LEDs are now quickly replacing other sources of illumination. The full potential of AlN and mixed alloy AlGaIn has not been yet used in commercial products and is still in

a research phase. One of the efforts is the development of LEDs to operate in the UV range by using the alloy AlGaIn, where wavelengths as short as 210 nm have been achieved [12–16]. The realization of laser diodes within the AlGaIn material system remains challenging due to physical limitations like doping, carrier injection, defect control and the complexity of synthesizing material of high crystalline quality [17–22]. For these reasons the shortest emission wavelength for a laser diode reported to date is 336 nm [23].

1.1 Research objectives

This doctorate thesis is a continuation of the research work on the potential of AlGaIn system for generation of blue and UV light through nonlinear frequency conversion. Initial studies were done by the former graduate student M. Rigler and are presented in his dissertation [24]. He had measured the refractive index dispersions of GaN, AlN and AlGaIn thin films and the results are published in Refs. [25, 26]. He also demonstrated second harmonic generation by using GaN waveguides to produce blue light with the wavelength of 450 nm. The manuscript [27] is submitted for publication.

In this work the focus is on generation of shorter wavelengths. We investigate the potential of AlN for generation of UV light through a nonlinear process of second harmonic generation (SHG). Here the incident laser light with frequency ω due to interaction with nonlinear material generates light wave with twice the original frequency 2ω . AlN has unique linear and nonlinear optical characteristics that allow its utilization for nonlinear conversion into UV spectral region. It is transparent down to 200 nm and has a large nonlinear susceptibility. In particular, it has two independent nonlinear coefficients d_{31} and the largest d_{33} , which was experimentally determined to be around $d_{33} = 4.3 \text{ pm/V}$ at $1 \mu\text{m}$ wavelength [28]. Thin AlN films of highest quality are grown on sapphire substrate by metalorganic chemical vapor deposition (MOCVD) by the Wide-bandgap group in North Carolina State University. With appropriate growth technique AlN can be fabricated such that crystallographic c-axis is periodically inverted forming lateral polar structures (LPS) [29]. The resulting AlN thin films on sapphire substrate form an optical waveguide due to the larger refractive index of AlN compared to the sapphire. Therefore during the thesis I will use the expression LPS-based waveguides or the synonym structured waveguides.

The advantage of using waveguides in nonlinear optics is the pump light confinement over longer distances. Therefore high and constant intensity is maintained over the whole interaction length. This is important because the second harmonic (SH) power increases quadratically with the pump power. Conversion efficiency of SH light is efficient only if phase matching between the pump and SH waves is established. Two viable techniques in AlN material are modal dispersion phase matching (MDPM) and quasi phase matching (QPM). Modal phase matching is possible due to the different propagation constants of different waveguide modes [31–34]. Because of the material dispersion, it is impossible to achieve phase matching for pump and SH light to propagate within the same waveguide mode. However, it is achievable

that different pump and SH modes have the same propagation constant and therefore phase matching is realized. The efficiency of this process is determined by the transverse spatial overlap between the interacting waveguide modes. Compared to quasi phase matching this method provides lower efficiencies, however, its benefit includes the facility to fabricate high quality single polar AlN waveguides where c-axis has fixed direction. The second technique is quasi phase matching (QPM) that uses periodic modulation of the optical nonlinear coefficient [35–37]. The efficiency of this method is much higher because the fundamental modes with high overlap at pump and SH frequencies interact. QPM is achieved in LPS-based waveguides with appropriate periodicity, determined by the coherence length, l_c . It depends on the waveguide geometry and refractive index dispersion relations of the waveguide and sapphire. It equals to the distance, over which the pump and SH light remain in phase. In the LPS-based waveguides with periodicity equal to $2l_c$ the pump power converts to SH power over the entire propagation distance.

The major experimental part of my work consisted of the SHG measurements in different AlN waveguides. A femtosecond laser with tunable wavelength was used as a light source. The laser light was coupled in and out of the waveguide by using end-fire coupling system. The generated SH light was spectrally analyzed with a spectrograph and the intensity was measured with a CCD camera. Additionally, morphology and roughness of the surface were analyzed with atomic force microscopy (AFM). The experimental work was performed at the Department of Complex Matter at Jožef Stefan Institute in Ljubljana.

1.2 Organization of the dissertation

After the introduction the thesis continues with Chapter 2, where some relevant properties of AlN are discussed and the growth procedure of the thin AlN films is described. In Chapter 3 the theory of guided waves in planar dielectric waveguides is presented and waveguide losses are qualitatively described. Chapter 4 deals with second harmonic generation in optical waveguides. Two techniques are introduced, modal phase matching and quasi phase matching. Additionally, a brief description of SHG of ultrashort pulses is presented. The experimental technique for measuring SHG signal and the corresponding equipment are described in Chapter 5. Finally, experimental results on SHG in various AlN waveguides are presented in Chapter 6. Chapter 7 summarizes the main findings of the thesis.

Chapter 2

Properties and growth of AlN

The group III-nitrides -(Al, In, Ga)N- are semiconductor materials that possess a number of attractive physical, optical and electronic properties for the fabrication of different optoelectronic devices. They offer a tunable bandgap that covers the whole visible spectrum into deep ultraviolet region. Among them, AlN has the largest bandgap energy, and is as such very suitable material for use in deep UV spectral region.

In this chapter some of the important physical properties of AlN material are presented and the growth of AlN lateral polar structures is described.

2.1 Material properties

AlN is a covalently bonded material. It can crystalize in three structural phases; wurtzite, zincblende and rock-salt [38]. Wurtzite structure, shown in Fig. 2.1.1, is the thermodynamically stable phase at ambient conditions. Each Al atom is surrounded by four N atoms, which are arranged at the edges of a tetrahedron. Likewise, each N atom is surrounded by four Al atoms. The stacking sequence of the wurtzite structure along c-axis is ABAB. Due to the lack of a center of symmetry and the large polarity of the metal-nitrogen bonds, the unit cell of the AlN is distorted from the ideal wurtzite unit cell. This results in strong spontaneous polarization along the c-axis [39]. It is composed of two parts: spontaneous polarization and strain-induced piezoelectricity. Due to strong covalent bond present within AlN, it possesses a high melting point, mechanical strength, chemical stability and good thermal conductivity [38,40]. Some of its properties are displayed in Table 2.1 [38].

AlN is a direct band gap semiconductor. At 300 K its bandgap equals 6.2 eV, which results in the transparency down to 200 nm. In the long wavelength side the transparency window extends to the far IR ($\sim 13 \mu\text{m}$) where the optical phonon modes appear [6,7]. AlN is optically anisotropic (uniaxial) with optical axis parallel to the c-axis of the crystal. Its birefringence is small, around 3 % [25,26]. AlN crystal structure lacks center of inversion, therefore it possesses second order nonlinearity. AlN has three nonzero nonlinear coefficients, d_{15} , d_{31} , and d_{33} being the largest one with experimentally measured value of around 4.3 pm/V [28].

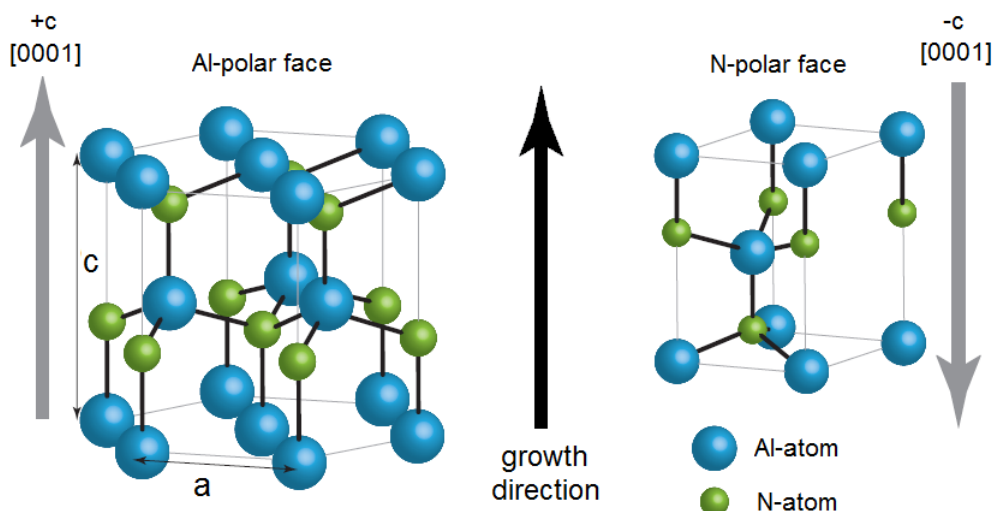


Figure 2.1.1: Wurtzite crystal structure of AlN showing two different polarity orientations. Al-polar (+c orientation) refers to configuration where the crystallographic c-axis is parallel to the growth direction, while the 180° rotated configuration refers to a N-polar (-c orientation).

Property	AlN	GaN
Thermal expansion coefficient ($10^{-6}K^{-1}$)	^a 4.2, ^c 3.17	^a 5.59, ^c 3.17
Thermal conductivity ($Wcm^{-1}K^{-1}$)	2.0	1.3
Melting point ($^{\circ}C$)	> 3000	> 2500
Bond length (\AA)	1.89	1.94
Lattice constant (\AA)	^a 3.11, ^c 4.97	^a 3.18, ^c 5.18
Energy gap (eV)	6.2	3.39

Table 2.1: Properties of wurtzite AlN and GaN [38].

2.2 AlN crystal growth

AlN thin films can be grown in two different configurations, N-polar and Al-polar, as shown in Fig.2.1.1. The case where crystallographic c-axis shows outwards the crystal surface is called Al-polar, whereas the c-axis of N-polar configuration is directed towards the crystal surface. Two different polarities of AlN can be grown side-by-side, thus forming a lateral polar structure (LPS) [29, 41]. In order to minimize waveguiding losses the domains of opposite polarity need to be of equal height, they have to have smooth surfaces and the interface between the domains has to be sharp.

AlN thin films are grown on sapphire substrate by metalorganic chemical vapor deposition (MOCVD). Using nitrogen and/or hydrogen as carrier gas, metalorganic (MO) precursors are used as the metal sources and ammonia (NH_3) is used as a nitrogen source. Both, the metalorganic precursor and NH_3 are transported to the

reaction zone above the substrate to form the desired group-III-nitride compound. Growth temperatures are up to 1500 °C for AlN and 1050 °C for GaN. Reactor pressures may range from 100 Pa to close to 100 KPa. Growth rates as high as 5 $\mu\text{m}/\text{h}$ can be achieved by MOCVD [42].

The details of the growth process resulting in AlN lateral polarity structures are sketched in Fig. 2.2.1. At first, an AlN nucleation layer is deposited on a c-

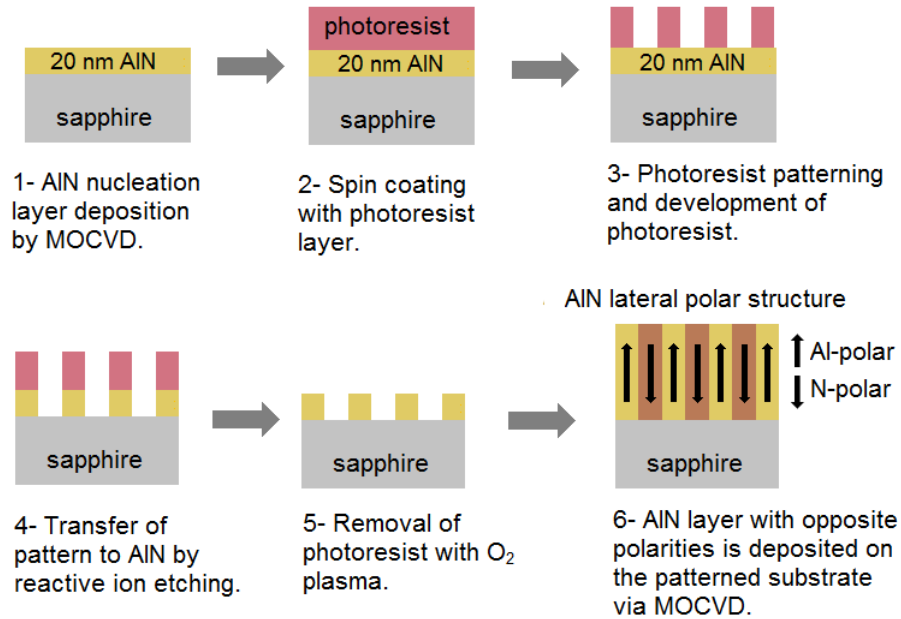


Figure 2.2.1: Scheme of the fabrication process for the polarity controlled AlN growth. In the first step AlN nucleation layer is deposited on c-plane of the sapphire. Second step includes deposition of photoresist by spin coating. In step 3 photoresist layer is exposed to the laser interference periodic pattern and developed. In the step 4 the pattern is transferred to the AlN nucleation layer by reactive ion etching. This is followed by the removal of the residual photoresist by the O_2 plasma. Finally, the substrate is reinserted in the MOCVD chamber and overgrown with an AlN periodic structure of desired thickness [42].

plane of the sapphire substrate. The substrate is then removed from the reactor to be patterned and etched by reactive ion etching (RIE), leaving the bare sapphire exposed to the etched regions and 20 nm low-temperature AlN nucleation layer in the areas covered by the photoresist. The sub-micron patterning is obtained using laser interference lithography. The pattern is transferred to the AlN nucleation layer by RIE, and the remaining photoresist residue is removed by isotropic O_2 plasma. The substrate is then placed in the reactor again where AlN is grown. In this process, N-polar domains grow on bare sapphire regions and Al-polar domains on the AlN nucleation layer.

Chapter 3

Optical waveguides

Optical waveguides are physical structures that guide electromagnetic waves in the optical spectrum. There is a flow of energy only along a guiding structure and not perpendicular to it. Optical waveguides are basic elements for confinement and transmission of light over various distances. Common types include optical fibers and rectangular waveguides. They are used as components in integrated optical circuits or as transmission media in optical communication systems. Furthermore, optical waveguides form key structures in semiconductor lasers, and act as passive and active devices such as waveguide couplers and modulators. In this work optical waveguides are used to maintain high optical intensity needed for efficient light frequency conversion.

This chapter provides the analysis of propagation of light in the simplest but most representative waveguide geometry, a planar dielectric waveguide. The electromagnetic field distributions are called waveguide modes and are found as the solutions of Maxwell equations subject to the appropriate boundary conditions defined by the waveguide structure [43, 44].

3.1 Planar waveguide

The simplest structure in which light is guided only in one direction is a planar waveguide sketched in Fig. 3.1.1. It consists of three layers: waveguide core with the highest refractive index n_2 , sandwiched between two layers with lower refractive indices n_1 and n_3 . A coordinate system is chosen with the z -axis perpendicular to the waveguide surface and light propagates in the x -direction.

In order to find the electric and magnetic field distributions in the proposed structure, Maxwell equations are applied. Inside a homogeneous and isotropic material with dielectric and magnetic constants ϵ and μ , respectively, the standard wave equation can be derived [43]:

$$\nabla^2 \mathbf{E} - \frac{\mu\epsilon}{c_0^2} \frac{\partial^2 \mathbf{E}}{\partial t^2} = 0 \quad \text{and} \quad \nabla^2 \mathbf{H} - \frac{\mu\epsilon}{c_0^2} \frac{\partial^2 \mathbf{H}}{\partial t^2} = 0, \quad (3.1.1)$$

where \mathbf{E} and \mathbf{H} describe electric and magnetic fields, respectively. The solutions

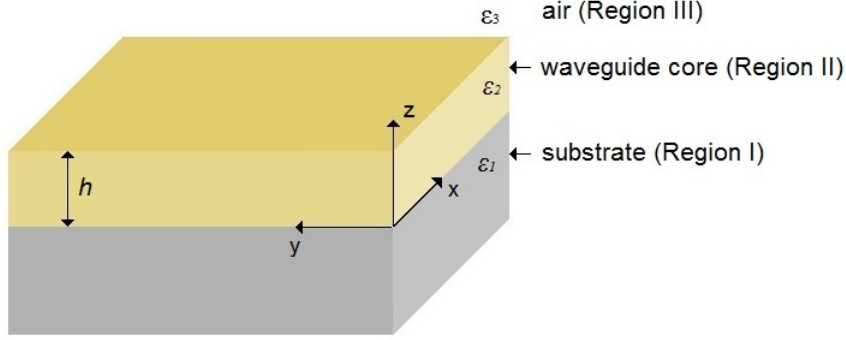


Figure 3.1.1: A planar waveguide consisting of the three regions: the core layer of thickness h , substrate and air. The dielectric constant of the core layer must be larger than the other two dielectric constants, $\varepsilon_2 > \varepsilon_1, \varepsilon_3$.

are well-known plane waves. We look for solutions with a fixed frequency ω that propagate in the x -direction. In this case the ansatz for the \mathbf{E} and \mathbf{H} fields can be expressed as

$$\begin{aligned}\mathbf{E}(x, z) &= \mathbf{E}_0 \psi(z) e^{i(\beta x - \omega t)}, \\ \mathbf{H}(x, z) &= \mathbf{H}_0 \psi(z) e^{i(\beta x - \omega t)},\end{aligned}\quad (3.1.2)$$

where β is the propagation constant, $\psi(z)$ is nondimensional function that describes the transverse distributions of the electromagnetic field, and $\mathbf{E}_0, \mathbf{H}_0$ are the electric and magnetic field polarization vectors, respectively. It is convenient to introduce the effective refractive index n_{eff} as

$$\beta = k_0 n_{\text{eff}}, \quad (3.1.3)$$

where $k_0 = \omega/c_0$ is the vacuum propagation constant. Effective refractive index is a key parameter in guiding structures as it is the analogue of the refractive index for unguided travelling waves. Inserting (8.2.2) into wave equation (8.2.1) and taking into account (8.2.3) yields

$$\left[\frac{\partial^2}{\partial z^2} + k_0^2 (n^2(z) - n_{\text{eff}}^2) \right] \psi(z) = 0. \quad (3.1.4)$$

Equation (3.1.4) governs the transverse behavior of the field. In the case of planar waveguide structure it splits into three equations describing three regions (see Fig. 3.1.1)

$$\begin{aligned}\text{Region I: } & \left(\frac{\partial^2}{\partial z^2} + k_0^2 [n_1^2 - n_{\text{eff}}^2] \right) \psi(z) = 0, \\ \text{Region II: } & \left(\frac{\partial^2}{\partial z^2} + k_0^2 [n_2^2 - n_{\text{eff}}^2] \right) \psi(z) = 0, \\ \text{Region III: } & \left(\frac{\partial^2}{\partial z^2} + k_0^2 [n_3^2 - n_{\text{eff}}^2] \right) \psi(z) = 0,\end{aligned}\quad (3.1.5)$$

where $n_i = \sqrt{\varepsilon_i}$. There are two types of solutions of the Eqs. 3.1.5, exponential and oscillatory. For a guiding mode there is no transverse energy flow, therefore the fields fall off exponentially outside the guiding structure. Inside the core, the solution is oscillatory. Therefore, from (3.1.5) it follows that the effective refractive index of a confined mode lies in the following interval

$$\max(n_1, n_3) < n_{\text{eff}} < n_2. \quad (3.1.6)$$

At the interface layers the tangential components of the fields must match and therefore only discrete number of possible values of n_{eff} are the solutions describing confined modes. The number of confined modes depends on the waveguide thickness h , frequency ω and the indices of refraction n_1, n_2 , and n_3 .

3.2 TM and TE solutions

We now solve the wave equation for the waveguide sketched in Fig.3.1.1. There exist two independent sets of solutions, TE modes with field components E_y, H_x and H_z , and TM modes with components H_y, E_x and E_z .

3.2.1 TM modes

The field components of TM modes are of the form

$$\begin{aligned} H_y(x, z, t) &= H_y^0 \psi(z) e^{i(\beta x - \omega t)}, \\ E_z(x, z, t) &= \frac{\beta}{\omega \varepsilon_0 \varepsilon(z)} H_y^0 \psi(z) e^{i(\beta x - \omega t)}, \\ E_x(x, y, z) &= -\frac{i H_y^0}{\omega \varepsilon_0 \varepsilon(z)} \frac{\partial \psi(z)}{\partial z} e^{i(\beta x - \omega t)}. \end{aligned} \quad (3.2.1)$$

Magnetic field constant H_y^0 is arbitrary, and the transverse mode function $\psi(z)$ is taken as

$$\psi(z) = \begin{cases} C e^{\kappa_1 z} & \text{if } z < 0, \\ C(\cos \kappa_2 z + \frac{\kappa_1}{\kappa_2} \sin \kappa_2 z) & \text{if } 0 < z < h, \\ C(\cos \kappa_2 h + \frac{\kappa_1}{\kappa_2} \sin \kappa_2 h) e^{-\kappa_3(z-h)} & \text{if } h < z. \end{cases} \quad (3.2.2)$$

Waveguide modes are orthogonal [43], and we choose constant C such that they are orthonormalized as

$$\frac{2}{h} \int_{-\infty}^{\infty} \frac{\psi_l(z) \psi_m(z)}{\varepsilon(z)} dz = \delta_{lm}, \quad (3.2.3)$$

where the subscripts l and m denote two waveguide modes. We introduced $\kappa_1, \kappa_2, \kappa_3$ that according to the Eqs.(3.1.5) satisfy the following equalities:

$$\begin{aligned} \kappa_1^2 &= \beta^2 - n_1^2 k_0^2, \\ \kappa_2^2 &= n_2^2 k_0^2 - \beta^2, \\ \kappa_3^2 &= \beta^2 - n_3^2 k_0^2. \end{aligned} \quad (3.2.4)$$

The fields $H_y(z)$ and $E_x(z)$ must be continuous at the two interfaces at both $z = 0$ and $z = h$. Partially, this was taken into account by the choice of the coefficients in Eq. (3.2.2). In addition, it must hold

$$\tan \kappa_2 h = \frac{\kappa_2 n_2^2 (n_1^2 \kappa_3 + n_3^2 \kappa_1)}{\kappa_2^2 n_1^2 n_3^2 - n_2^4 \kappa_1 \kappa_3}. \quad (3.2.5)$$

Propagation constants β that solve the Eqs.(3.2.4) and (3.2.5) are the possible TM modes. In general, there exist more than one solution provided the thickness h is large enough. The solutions are labeled with an integer, denoting the number of magnetic field nodes in the z -direction. The lowest order mode TM0 is called fundamental mode, and the others are higher order modes. Transverse functions $\psi(z)$ for the lowest four TM modes in an AlN waveguide are depicted in Fig. 3.2.1.

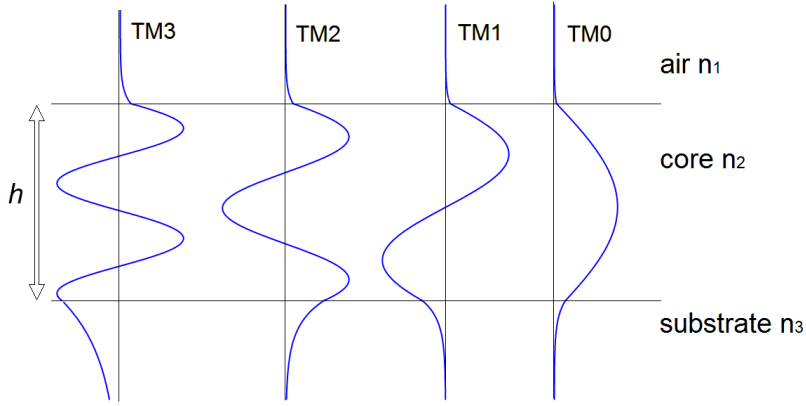


Figure 3.2.1: First four modes in planar waveguide of thickness $h = 1 \mu\text{m}$ and wavelength of light 633 nm. The waveguide consists of sapphire substrate with $n_3 = 1.7$ and AlN core with $n_2 = 2.2$. Upper layer is air with $n_1 = 1$.

3.2.2 TE modes

We repeat the same procedure for the TE modes with nonzero electric field component

$$E_y(x, z, t) = E_y^0 \psi(z) e^{i(\beta x - \omega t)} \quad (3.2.6)$$

The mode function $\psi(z)$ is taken as

$$\psi(z) = \begin{cases} C e^{\kappa_1 z} & \text{if } z < 0, \\ C(\cos \kappa_2 z + \frac{\kappa_1}{\kappa_2} \sin \kappa_2 z) & \text{if } 0 < z < h, \\ C(\cos \kappa_2 h + \frac{\kappa_1}{\kappa_2} \sin \kappa_2 h) e^{-\kappa_3(z-h)} & \text{if } h < z. \end{cases}$$

Similarly as in the case of TM modes, the orthogonality property of TE modes reads

$$\frac{2}{h} \int_{-\infty}^{\infty} \psi_l(z) \psi_m(z) dz = \delta_{lm}, \quad (3.2.7)$$

The continuity of the fields $H_x(z)$ and $E_y(z)$ at the two interfaces lead us to the relation

$$\tan \kappa_2 h = \frac{\kappa_2(\kappa_1 + \kappa_3)}{\kappa_2^2 - \kappa_1 \kappa_3}. \quad (3.2.8)$$

For a given waveguide structure, discrete number of confined modes at the fixed frequency can propagate. There exist a cut-off value λ_c , corresponding to the wavelength in vacuum, below which the mode becomes confined. At the cut-off value the effective refractive index equals the refractive index of the substrate n_3 and the mode extends to $z = -\infty$. Slightly below the cut-off value $\lambda < \lambda_c$, the mode becomes poorly confined. When decreasing λ even more, the value of n_{eff} approaches n_2 and becomes strongly confined to the core layer.

3.3 Losses in optical waveguides

When light propagates through a waveguide it experiences attenuation. This loss is generally attributable to different mechanisms like scattering, absorption and radiation [45]. There are two types of scattering loss, volume and surface scattering. Volume scattering is caused by imperfections such as voids, contaminant atoms and crystalline defects within the volume of the waveguide. The loss due to volume scattering is proportional to the density of imperfections. It also depends in a complicated way on the relative size of the imperfections. Usually, the volume imperfections are so small compared to wavelength, and so few in number, that the volume scattering loss is negligible compared to surface scattering loss. In case of AlN, absorption losses were negligible due to its transparency in the used spectral range of light. The radiation losses take place for modes above cut-off and for the waveguides that are bent.

The major source of losses come from the waveguide surface irregularities and roughness as a consequence of the fabrication process. There exist many papers that describe scattering losses due to the rough waveguides surface. The simplest model derived by Tien [46] is based on the ray optics approach, but nevertheless provides a convenient expression for the scattering loss. More sophisticated theory was derived by Marcuse [47–49] that treats surface scattering as a form of radiation loss in which irregularities in the surfaces of waveguide couple energy from propagating modes into radiation modes and other propagating modes. Using some approximations the exact solutions are found only for TE modes, while TM case is more complicated and the solutions are found numerically [49].

Some guidelines regarding scattering losses due to the rough top waveguide surface can be discussed qualitatively. According to the Rayleigh model, scattering increases with the fourth power of inverse light wavelength. This is true only if the irregularities are much smaller than the wavelength of light. Moreover it can be deduced that scattering intensity is influenced by the amplitude of the electric field at the rough surface. Since the electric field at the boundary increases with increasing mode number, it follows that losses increase with the mode number as well. Simi-

larly one could say that the more confined modes are less influenced by the scattering losses. Of importance is also the refractive index difference between the core and the surrounding layer. By decreasing the index difference, the losses decrease as well, however, one should notice that the last two factors are not completely independent.

To quantitatively describe the magnitude of the optical loss, the exponential attenuation coefficient α is generally used. In that case the optical power at any point along the length of the waveguide is given by

$$P(x) = P_0 e^{-\alpha x}, \quad (3.3.1)$$

where P_0 is the initial optical power at $x = 0$. Usually loss is measured in dB and the relationship between the two coefficients is given by $L = 4.3 \alpha$.

Chapter 4

Second harmonic generation

Nonlinear optics is a branch of optics that describes the nonlinear response of the atoms and molecules to optical radiation fields. Nonlinear response is much weaker than the linear response and the applied values of the electric field have to be comparable to the interatomic fields ($\sim 10^8 V/m$) in order to yield a measurable response. With the advent of lasers that can produce enough power to trigger nonlinear processes in matter this field has become very rich. Second harmonic generation or frequency doubling is one of the nonlinear optical processes, in which the input (pump) wave interacts with a nonlinear material and generates light wave with twice the input frequency. SHG was first observed in a quartz sample using a ruby laser with a wavelength of 694 nm in 1961 by Peter Franken et al. [50]. Since that time SHG technique developed significantly and nowadays a wide variety of applications and nonlinear materials exist [45, 51].

This chapter starts with a short introduction in nonlinear optics. The theoretical formulation of SHG in planar optical waveguides is given where the monochromatic waves are considered. Two techniques, modal phase matching and quasi phase matching, are reexamined. In the last part, the theory is extended to explain second harmonic generation of a broadband optical pulse.

4.1 Nonlinear optics

When light interacts with matter, it induces dipole moments in the individual atoms or molecules in the material. The average of these dipole moments is called polarization. The response of the material can be expressed in a Taylor series expansion. We assume the material is lossless, so that the response is instantaneous. Using Einstein summation convention, the i -th component of the material polarization P_i can be written as [51, 52]

$$P_i = P_i^L + P_i^{NL} = \varepsilon_0 \chi_{ij}^{(1)} E_j + \varepsilon_0 \chi_{ijk}^{(2)} E_j E_k + \varepsilon_0 \chi_{ijkl}^{(3)} E_j E_k E_l + \dots, \quad (4.1.1)$$

where E_i is the i -th component of the instantaneous field. The coefficients $\chi_{ij}^{(1)}$, $\chi_{ijk}^{(2)}$ and $\chi_{ijkl}^{(3)}$ are susceptibilities of the first, second and third order, respectively.

The first term in Eq. (8.3.1) describes linear response and is predominant for small input electric fields. In other words, the fields radiated by the dipoles have the same frequency as the input beam. This give rise to the linear refractive index and linear absorption. On the other hand, if the incident electric field is large and starts to be comparable to the electric field binding the electrons to nucleus, the response becomes nonlinear and induced polarization begins to oscillate anharmonically. Many interesting phenomena and applications exist due to the nonlinear response. We will focus on the second term in Eq.(8.3.1), which is responsible for sum and difference frequency generation and parametric amplification. Second harmonic generation is a special case of sum frequency generation, where the applied optical field of frequency ω induces polarization that radiates at twice the frequency 2ω . This can be easily viewed by considering the nonlinear response to the optical field oscillating with frequency ω

$$E_j^\omega(t) = \frac{1}{2}(E_{0,j}^\omega e^{i\omega t} + c.c.) \quad (j = x, y, z), \quad (4.1.2)$$

Then the i -th component of the induced second order polarization in the material is

$$P_i(t) = \varepsilon_0 \chi_{ijk}^{(2)} \left(\frac{1}{2} E_{0,j}^\omega e^{i\omega t} + c.c. \right) \left(\frac{1}{2} E_{0,k}^\omega e^{i\omega t} + c.c. \right) \quad (4.1.3)$$

$$= \frac{1}{4} \varepsilon_0 \chi_{ijk}^{(2)} E_{0,j}^\omega E_{0,k}^\omega (e^{i2\omega t} + 1) + c.c. \quad (4.1.4)$$

Considering only the second harmonic frequency term we get

$$P_i^{2\omega}(t) = \frac{1}{4} \varepsilon_0 \chi_{ijk}^{(2)} E_{0,j}^\omega E_{0,k}^\omega e^{i2\omega t} + c.c. \quad (4.1.5)$$

Let us now discover the properties of the second order susceptibility tensor $\chi_{ijk}^{(2)}$. In the most general case, $\chi_{ijk}^{(2)}$ has 18 nonzero elements. According to Eq.(8.3.1) there is no difference if the indices j and k in $\chi_{ijk}^{(2)}$ are interchanged. Thus we can replace the subscripts kj and jk by the contracted indices as

$$\begin{aligned} xx = 1, & \quad yy = 2, & \quad zz = 3 \\ yz = zy = 4, & \quad xz = zx = 5, & \quad xy = yx = 6. \end{aligned} \quad (4.1.6)$$

Centrosymmetric materials do not exhibit second order nonlinearity. This follows from the requirement that a reversal of the signs of $E_j^{\omega_1}$ and $E_k^{\omega_2}$ must cause a reversal in the sign of $P_i^{\omega_1+\omega_2}$. Using Eq.(8.3.1) we get $\chi_{ijk}^{(2)} \equiv 0$. On the other hand, for noncentrosymmetric materials the relations between different elements of the tensor are defined by point symmetry group of the crystal. There is additional symmetry due to energy conservation (Kleinman symmetry) that is valid when all frequencies are far away from absorption bands of the material and lie in the same transparency window:

$$\chi_{ijk} = \chi_{ikj} = \chi_{kij} = \chi_{kji} = \chi_{jki} = \chi_{jki}. \quad (4.1.7)$$

In the literature the susceptibility tensor $\chi_{ijk}^{(2)}$ is usually replaced by $d_{ijk} = \chi_{ijk}^{(2)}/2$. Therefore the resulting d_{ijk} components form a 3×6 matrix that operates on the E^2 column tensor to yield \mathbf{P} according to

$$\begin{bmatrix} P_x \\ P_y \\ P_z \end{bmatrix} = \varepsilon_0 \begin{bmatrix} d_{11} & d_{12} & d_{13} & d_{14} & d_{31} & d_{21} \\ d_{21} & d_{22} & d_{23} & d_{32} & d_{14} & d_{12} \\ d_{31} & d_{32} & d_{33} & d_{23} & d_{13} & d_{14} \end{bmatrix} \begin{bmatrix} E_x^2 \\ E_y^2 \\ E_z^2 \\ 2E_y E_z \\ 2E_z E_x \\ 2E_x E_y \end{bmatrix}. \quad (4.1.8)$$

Crystal symmetry can further reduce the number of independent elements. For example, crystals with 6 mm point group symmetry, such as AlN, have five nonvanishing elements with two independent values d_{33} and d_{31} [43]. The tensor d_{ijk} is of the form

$$\begin{bmatrix} P_x \\ P_y \\ P_z \end{bmatrix} = \varepsilon_0 \begin{bmatrix} 0 & 0 & 0 & 0 & d_{31} & 0 \\ 0 & 0 & 0 & d_{31} & 0 & 0 \\ d_{31} & d_{31} & d_{33} & 0 & 0 & 0 \end{bmatrix} \begin{bmatrix} E_x^2 \\ E_y^2 \\ E_z^2 \\ 2E_y E_z \\ 2E_z E_x \\ 2E_x E_y \end{bmatrix}. \quad (4.1.9)$$

4.2 Second harmonic generation in planar optical waveguides

Electromagnetic fields that describe second harmonic generation are the solutions of the Maxwell equations, where the second order nonlinear polarization (Eq. (4.1.4)) is taken into account [34, 53]. In an isotropic material with no free charges the wave equation with a nonlinear term can be derived to get

$$\nabla^2 \mathbf{E}(\mathbf{r}, t) - \frac{\varepsilon}{c_0^2} \frac{\partial^2 \mathbf{E}(\mathbf{r}, t)}{\partial t^2} = \mu_0 \frac{\partial^2 \mathbf{P}^{\text{NL}}(\mathbf{r}, t)}{\partial t^2}, \quad (4.2.1)$$

where μ_0 and $\varepsilon = 1 + \chi^{(1)}$ are magnetic and dielectric constants, respectively. We solve the Eq. 4.2.1 by utilizing the solutions of the linear wave equation found for both pump and SH wave described in Chapter 3. The nonlinear polarization is generated by a suitable combination of the waveguide modes at the fundamental frequency. The solution of the nonlinear equation is then found as a sum of the waveguide modes at fundamental and SH frequency with spatially dependent amplitudes of electromagnetic fields. Before we proceed, let us define conditions and assumptions relevant for the description of SHG in AlN waveguides. The coordinate system is shown in Fig. 3.1.1. Light propagates in the x-direction and the optical axis of AlN points in the z-direction. The incident light has a frequency ω and is chosen to be TM polarized with nonzero components E_z , E_x and H_y . Only the largest nonlinear coefficient d_{33} is relevant in AlN material which couples the z-components of the

electric fields at ω and 2ω . Consequently the Eq. 4.2.1 simplifies to a scalar equation. With this in mind we search for the solutions of the nonlinear wave equation. The z-components of the fields at frequency ω and 2ω are in general composed of several modes denoted with the indices p , and s and are written as [34]

$$E_\omega(x, z, t) = \sum_p \frac{1}{2\varepsilon_\omega(z)} (E_\omega^p(x)\psi_\omega^p(z)e^{i(\beta_\omega^p x - \omega t)} + c.c.), \quad (4.2.2)$$

$$E_{2\omega}(x, z, t) = \sum_s \frac{1}{2\varepsilon_{2\omega}(z)} (E_{2\omega}^s(x)\psi_{2\omega}^s(z)e^{i(\beta_{2\omega}^s x - 2\omega t)} + c.c.), \quad (4.2.3)$$

where the electric field amplitudes $E_\omega^p(x)$ and $E_{2\omega}^s(x)$ vary with x-coordinate in contrast to the solution defined in Eq. 3.2.1 where $E_\omega = \frac{\beta H_y^0}{\omega}$ is constant. Nonlinear polarization that oscillates with 2ω is expressed as

$$P_{2\omega}^{\text{NL}}(x, z, t) = \frac{\epsilon_0}{4\varepsilon_\omega^2(z)} \sum_{pr} d_{33} E_\omega^p(x) E_\omega^r(x) \psi_\omega^p(z) \psi_\omega^r(z) e^{i[(\beta_\omega^p + \beta_\omega^r)x - 2\omega t]} + c.c. \quad (4.2.4)$$

Following the standard procedure, Eq. (4.2.4) is inserted into nonlinear wave equation (4.2.1). For the frequency 2ω , taking into account the non-depleted pump and slowly varying envelope approximation, the following expression is derived

$$\sum_s \frac{\partial E_{2\omega}^s(x)}{\partial x} \frac{\psi_{2\omega}^s(z)}{\varepsilon_{2\omega}(z)} e^{i\beta_{2\omega}^s x} n_{\text{eff}}^{2\omega, s} = \frac{i\omega d_{33}}{2c_0\varepsilon_\omega^2(z)} \sum_{pr} E_\omega^p E_\omega^r \psi_\omega^p(z) \psi_\omega^r(z) e^{i(\beta_\omega^p + \beta_\omega^r)x}. \quad (4.2.5)$$

We are interested in the development of individual SHG modes, so in the next step Eq. (4.2.5) is multiplied with $\psi_{2\omega}^s(z)e^{-i\beta_{2\omega}^s x}$ and integrated over the xz-plane. The electric field amplitude of the s-th mode, $E_{2\omega}^s$, is then

$$E_{2\omega}^s(x) = \frac{i4\omega d_{33}}{3\pi c_0 n_{\text{eff}}^{2\omega, s} \varepsilon_\omega^2} \sum_{pr} E_\omega^p E_\omega^r \sqrt{\Gamma_{p,r;s}} \frac{e^{i\Delta\beta_{p,r;s}x} - 1}{i\Delta\beta_{p,r;s}}, \quad (4.2.6)$$

where the orthonormalization of the transverse field distributions of the waveguide modes defined in Eq. 3.2.3 was taken into account. Two terms were introduced, namely the phase mismatch term

$$\Delta\beta_{p,r;s} = \beta_{2\omega}^s - \beta_\omega^p - \beta_\omega^r, \quad (4.2.7)$$

and the overlap integral

$$\Gamma_{p,r;s} = \frac{9\pi^2}{16h^2} \left[\int_0^h \psi_\omega^p(z) \psi_\omega^r(z) \psi_{2\omega}^s(z) dz \right]^2 \quad (4.2.8)$$

which is the dimensionless quantity normalized to 1 when three fundamental modes perfectly overlap. From Eq. (4.2.6) we can derive the power density (power per unit length in y-direction) carried by the s-th SH waveguide mode as

$$P_{2\omega}^s(x) = \frac{64\omega^2 d_{33}^2 n_{\text{eff}}^{\omega, p} n_{\text{eff}}^{\omega, r}}{9\pi^2 h \varepsilon_0 c_0^3 (n_{\text{eff}}^{2\omega, s})^3 \varepsilon_\omega^4} P_\omega^p P_\omega^r \Gamma_{p,r;s} \text{sinc}^2(\Delta\beta_{p,r;s}x) x^2, \quad (4.2.9)$$

where the following definition was used for the power density of the t -th planar waveguide mode where $t = p, r, s$ oscillating with $\Omega = \omega, 2\omega$

$$P_{\Omega}^t(x) = \frac{1}{2} \int (\mathbf{H}_{\Omega}^t)^* (\mathbf{E}_{\Omega}^t)_z dz = \frac{\Omega \varepsilon_0 h}{4\beta_{\Omega}^t} |\mathbf{E}_{\Omega}^t(\mathbf{x})|^2. \quad (4.2.10)$$

The SH power in general oscillates between zero and some value as a function of x . For a special case when phase matching is achieved, $\Delta\beta_{p,r;s} = 0$, it increases quadratically with x -coordinate.

4.3 Modal dispersion phase matching

Phase matching can be achieved in the multimode optical waveguides by selecting a set of modes p, r , and s giving zero mismatch, $\Delta\beta_{p,r;s} = 0$, or in terms of effective refractive indices

$$n_{\text{eff}}^{2\omega,s} = \frac{n_{\text{eff}}^{\omega,p} + n_{\text{eff}}^{\omega,r}}{2} \quad (4.3.1)$$

In this case, $P_{2\omega}^s(x)$ increases quadratically with x -coordinate as

$$P_{2\omega}^s(x) = \frac{64\omega^2 d_{33}^2 n_{\text{eff}}^{\omega,p} n_{\text{eff}}^{\omega,r}}{9\pi^2 h \varepsilon_0 c_0^3 (n_{\text{eff}}^{2\omega,s})^3 \varepsilon_{\omega}^4} P_{\omega}^p P_{\omega}^r \Gamma_{p,r;s} x^2. \quad (4.3.2)$$

Modal dispersion phase matching (MDPM) in materials with normal dispersion relation can be achieved for the combinations p, r , and s that satisfy condition

$$p \leq r < s \quad \text{or} \quad p < r \leq s. \quad (4.3.3)$$

In Fig.4.3.1 modal phase matching points in 550 nm thick AlN film on sapphire substrate are shown. The blue and red curves represent the left and the right side of the Eq.(4.3.1), respectively, as a function of wavelength. In addition to phase matching, the interacting modes should also have a large spatial overlap in transversal direction. In order to estimate the value of overlap integrals for various MDPM combinations, we make the following simplification: if the refractive index of the waveguide core is much bigger than that of the surrounding layers, the transverse distributions of the electromagnetic field simplify into sine functions

$$\psi^n(z) = \sin\left(\frac{\pi}{h}(1+n)z\right), \quad (4.3.4)$$

where n indicates the mode number. The overlap integral is then expressed as

$$\Gamma_{p,r;s} = \frac{9\pi^2}{16h^2} \left[\int_0^h \sin\left(\frac{\pi}{h}(1+p)z\right) \sin\left(\frac{\pi}{h}(1+r)z\right) \sin\left(\frac{\pi}{h}(1+s)z\right) dz \right]^2. \quad (4.3.5)$$

The overlap integrals for the lowest seven waveguide modes are listed in the Table 4.1. It should be emphasized that this simplification gives correct overlap integral values only for the modes that are strongly confined. For poorly confined modes there is a slight deviation from the listed values.

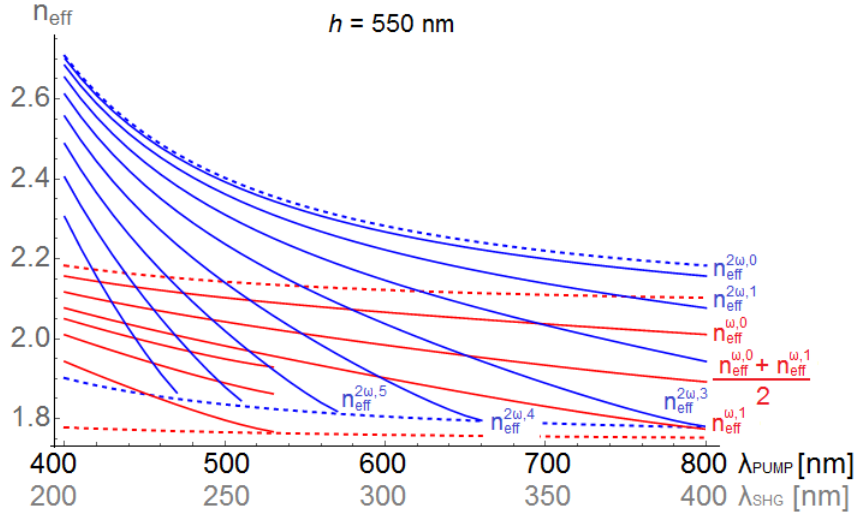


Figure 4.3.1: The dispersion of effective refractive indices in an AlN waveguide of thickness $h = 550 \text{ nm}$ on sapphire substrate. Red solid curves show the effective refractive index dispersions for the zero and first order pump modes and the combination of the two. Blue solid curves show dispersions for different order SH modes. MDPM occurs at the intersections of the curves. Dotted lines represent the dispersions of the extraordinary refractive indices of bulk AlN and sapphire.

$p, r; s$	$\Gamma_{p,r;s}$	$p, r; s$	$\Gamma_{p,r;s}$	$p, r; s$	$\Gamma_{p,r;s}$	$p, r; s$	$\Gamma_{p,r;s}$
0, 0; 0	1	0, 3; 3	0.6	1, 2; 5	0.08	2, 4; 6	0.22
0, 0; 2	0.04	0, 3; 5	0.6	1, 3; 4	0.27	2, 5; 5	0.07
0, 0; 4	0.0008	0, 4; 4	0.57	1, 3; 6	0.08	2, 6; 6	0.07
0, 0; 6	9×10^{-5}	0, 4; 6	0.06	1, 4; 5	0.26	3, 4; 4	0.06
0, 1; 1	0.6	0, 5; 5	0.6	1, 5; 6	0.26	3, 3; 6	0.21
0, 1; 3	0.05	0, 6; 6	0.6	2, 2; 4	0.24	3, 4; 5	0.05
0, 1; 5	0.0015	1, 1; 2	0.3	2, 2; 6	0.09	3, 5; 6	0.048
0, 2; 2	0.61	1, 1; 4	0.07	2, 3; 3	0.08	4, 4; 6	0.044
0, 2; 4	0.06	1, 1; 6	0.0027	2, 3; 5	0.22	4, 6; 6	0.03
0, 2; 6	0.0018	1, 2; 3	0.28	2, 4; 4	0.08	5, 5; 6	0.026

Table 4.1: Approximate values of normalized overlap integrals for different waveguide mode combinations $(p, r; s) = (0, 1, 2, 3, 4, 5, 6)$ for which condition (4.3.3) is true. Calculations were done in the limit of perfect confinement of modes inside the waveguide core.

4.4 Quasi phase matching

Quasi phase matching is achieved in materials with periodic spatial modulation of the nonlinear optical coefficient. In such materials the phases of the pump and SH waves are corrected at regular intervals defined by coherence length l_c , a distance at

which the pump and SH waves reach relative phase shift of π . The advantage of quasi phase matching in AlN waveguides is that all combinations of waveguide modes can be phase matched, particularly the fundamental pump and SH modes that give the highest conversion efficiency.

Fig. 4.4.1 illustrates a periodically poled planar waveguide. It consists of the domains with opposite sign of the nonlinear polarization with periodicity $\Lambda = 2l_c$. We can write the nonlinear coefficient d_{33} as a function of x-coordinate as

$$d_{33}(x) = \begin{cases} -d & \text{if } n\Lambda < x < \frac{(2n+1)\Lambda}{2}, \\ d & \text{if } \frac{(2n+1)\Lambda}{2} < x < (n+1)\Lambda, \end{cases}$$

where $n \in \mathbb{Z}^+$. The periodic function $d_{33}(x)$ can be written as a Fourier series

$$d_{33}(x) = d \sum_{N \in \mathbb{Z}^+} \frac{i[(-1)^N - 1]}{\pi N} e^{-i2\pi Nx/\Lambda} + c.c.. \quad (4.4.1)$$

Following the same procedure as earlier in the text we start with the nonlinear wave

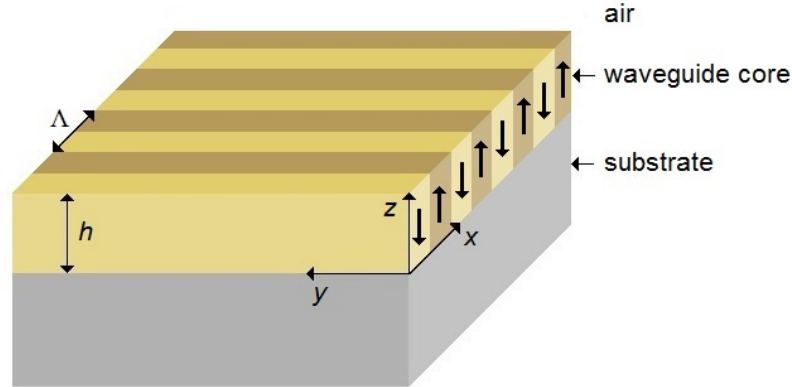


Figure 4.4.1: A LPS-based waveguide waveguide of thickness h . The arrows show the direction of the nonlinear polarization that periodically changes with periodicity Λ .

Eq. (4.2.1) and the electric field amplitudes as defined in Eq. (4.2.3). Using (4.4.1) the amplitude of the electric field at 2ω at the rear end of the waveguide is then

$$E_{2\omega}^s(L) = \frac{i4\omega}{3\pi c_0 n_{\text{eff}}^{2\omega,s} \varepsilon_\omega^2} \sum_{pr} E_\omega^p E_\omega^r \sqrt{\Gamma_{p,r;s}} \int_0^L \sum_{N \in \mathbb{Z}^+} d \frac{i[(-1)^N - 1]}{\pi N} e^{-i2\pi Nx/\Lambda} e^{i\Delta\beta_{p,r;s}x} dx. \quad (4.4.2)$$

Integrating over x-coordinate results in

$$E_{2\omega}^s(L) = \frac{i4\omega}{3\pi c_0 n_{\text{eff}}^{2\omega,s} \varepsilon_\omega^2} \sum_{pr} E_\omega^p E_\omega^r \sqrt{\Gamma_{p,r;s}} d \sum_{N \in \mathbb{Z}^+} \frac{[(-1)^N - 1] e^{i(\Delta\beta - 2\pi N/\Lambda)L} - 1}{\pi N (\Delta\beta - 2\pi N/\Lambda)}. \quad (4.4.3)$$

We are interested in the case where the waveguide length is much larger than the periodicity, $L \gg \Lambda$. Then the value of $E_{2\omega}^s(L)$ is maximal if the following relationship between periodicity and phase mismatch $\Delta\beta_{p,r;s}$ is true

$$\Delta\beta_{p,r;s} = \frac{2\pi N}{\Lambda}, \quad (4.4.4)$$

where $N = 1, 3, 5, \dots$ signifies the quasi phase matching order. In this case

$$E_{2\omega}^s(L) = \frac{i8\omega d}{3\pi^2 N c_0 n_{\text{eff}}^{2\omega,s} \varepsilon_\omega^2} E_\omega^p E_\omega^r \sqrt{\Gamma_{p,r;s}} L. \quad (4.4.5)$$

From this expression we can evaluate SH power per unit length in y-direction as

$$P_{2\omega}^{s,N}(L) = \frac{256 \omega^2 d^2 n_{\text{eff}}^{\omega,p} n_{\text{eff}}^{\omega,r}}{9N^2 \pi^4 h \varepsilon_0 c_0^3 \varepsilon_\omega^4 (n_{\text{eff}}^{2\omega,s})^3} P_\omega^p P_\omega^r \Gamma_{p,r;s} L^2. \quad (4.4.6)$$

From the above analysis it is clear that in periodically poled waveguides phase matching occurs through two mechanisms, MDPM and QPM. The power efficiency is by the factor of $4/(\pi N)^2$ lower compared to the value obtained in single polarity waveguides (Eq. (4.3.2)). However, the advantage of quasi phase matching lies in the fact, that condition (4.3.3) no longer has to be true. This means that combinations of modes p, r , and s that have large overlap integral values, can be phase matched. In particular, we are interested in the mode combination $(p, r; s) = (0, 0; 0)$ that has the highest overlapping. We can rewrite the condition (4.4.4) in terms of effective refractive indices as

$$n_{\text{eff}}^s(\lambda/2) - N \frac{\lambda}{2\Lambda} = \frac{n_{\text{eff}}^p(\lambda) + n_{\text{eff}}^r(\lambda)}{2}, \quad (4.4.7)$$

where λ is the pump wavelength. Comparing the obtained relation (4.4.7) to the relation for single polarity waveguides (4.3.1), we see that for LPS-based waveguides we have to subtract a positive term $N \frac{\lambda}{2\Lambda}$ in the left hand side of the Eq.(4.4.7). Thus, by adjusting the periodicity Λ we can determine the quasi phase matching wavelength. In Fig. 4.4.2 the periodicity Λ is plotted as a function of pump wavelength λ for the case of the first order quasi phase matching of the fundamental modes, $(p, r; s) = (0, 0; 0)$. Four differently thick AlN waveguides on sapphire substrate are considered.

As an example, the analysis of the particular waveguide mode combinations $(p, r; s) = (0, 0; 0)$ for the case of $h = 550 \text{ nm}$ thick AlN waveguide with $10 \mu\text{m}$ periodicity is shown in Fig. 4.4.3. Here, all QPM orders N are considered and Eq. (4.4.7) was used for the graphical representation. A dotted curve is added to represent the modal phase matching in a single polar waveguide. Modal phase matching within single polar waveguides can be viewed as the limiting case of the quasi phase matching where $\Lambda \rightarrow \infty$. Certain phase matching point defined by the mode combinations $(p, r; s)$ shifts towards shorter wavelengths when decreasing the period size Λ . Besides, instead of one phase matching point we can get multiple points as a consequence of the higher order phase matching.

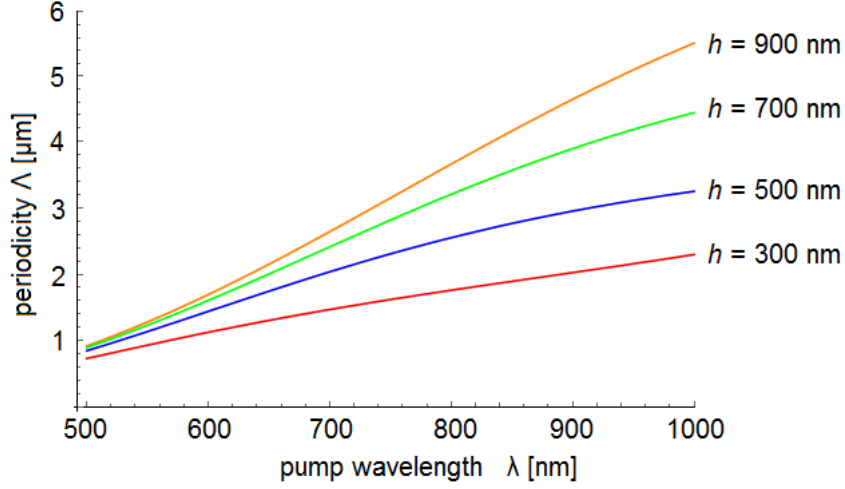


Figure 4.4.2: Periodicity Λ as a function of pump wavelength λ for quasi phase matching between fundamental pump and SH mode combinations, $(p, r; s) = (0, 0; 0)$. Calculations are done for different thicknesses of planar AlN waveguide on sapphire substrate.

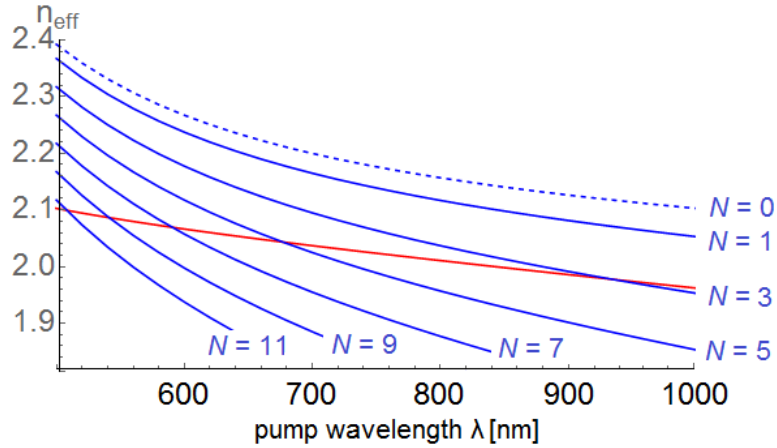


Figure 4.4.3: Quasi phase matching in periodically poled AlN waveguide of thickness $h = 550 \text{ nm}$ and periodicity $\Lambda = 10 \mu\text{m}$. Only the mode combination $(p, r; s) = (0, 0; 0)$ is considered. Red curve represent right side of the Eq. (4.4.7) as a function of wavelength, and blue curves represent the left side of the Eq. (4.4.7) for different QPM orders N .

4.4.1 Errors in domain sizes

During the growth of lateral polar structures it often occurs that the domains are of different length. We can analyse different types of the domain size errors. The domain lengths can be randomly distributed around some average value. Another, more

apparent error is due to the unequal domain sizes where periodicity is kept constant. Both cases were analyzed numerically for the first order quasi phase matching in [24]. Although the first order QPM is only slightly affected by the domain size errors, this is not the case for the higher order QPM. Furthermore, the even orders QPM that are forbidden in the case of equal domain sizes, may appear [54].

The analysis is done for the practical case encountered in lithography prepared samples. The basic period is well defined, however, the domains of opposite polarities have different length along the waveguide direction, as illustrated in Fig. 4.4.4. The

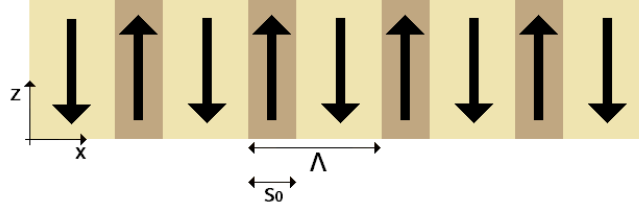


Figure 4.4.4: Periodically poled waveguide with different domain sizes s_0 and $\Lambda - s_0$.

nonlinear coefficient is then of the form

$$d_{33}(x) = \begin{cases} -d & \text{if } n\Lambda < x < n\Lambda + s_0, \\ d & \text{if } n\Lambda + s_0 < x < (n+1)\Lambda, \end{cases}$$

where $n \in \mathbb{Z}^+$. The periodic function $d_{33}(x)$ can be written as a Fourier series

$$d_{33}(x) = d \left(\sum_{N \in \mathbb{Z}^+} \frac{i[(1 - e^{i2\pi N s_0 / \Lambda})]}{\pi N} e^{-i2\pi N x / \Lambda} + \frac{2s_0 - \Lambda}{2\Lambda} \right) + c.c.. \quad (4.4.8)$$

Using the same procedure as before, we derive the expression for the electric field as

$$E_{2\omega}^s(L) = \frac{i4\omega}{3\pi c_0 n_{\text{eff}}^{2\omega, s} \varepsilon_{\omega}^2} \sum_{pr} E_{\omega}^p E_{\omega}^r \sqrt{\Gamma_{p,r;s}} df(L), \quad (4.4.9)$$

where

$$f(L) = \left[\sum_{N \in \mathbb{Z}^+} \frac{(1 - e^{i2\pi N s_0 / \Lambda})(e^{i(\Delta\beta - 2\pi N / \Lambda)L} - 1)}{\pi N (\Delta\beta - 2\pi N / \Lambda)} + \left(\frac{2s_0 - \Lambda}{2\Lambda} \right) \frac{e^{i\Delta\beta L} - 1}{i\Delta\beta} \right]. \quad (4.4.10)$$

According to the last two terms there exist two phase matching conditions. One is the same as for MDPM, and reads

$$\Delta\beta_{p,r;s} = 0. \quad (4.4.11)$$

In this case the SH power is reduced by the factor $((2s_0 - \Lambda)/\Lambda)^2$ compared to the MDPM power,

$$P_{2\omega}^s(L) = \frac{64\omega^2 d^2 n_{\text{eff}}^{\omega, p} n_{\text{eff}}^{\omega, r}}{9\pi^2 h \varepsilon_0 c_0^3 \varepsilon_{\omega}^4 (n_{\text{eff}}^{2\omega, s})^3} P_{\omega}^p P_{\omega}^r \Gamma_{p,r;s} \left(\frac{2s_0 - \Lambda}{\Lambda} \right)^2 L^2. \quad (4.4.12)$$

The second, QPM condition reads

$$\Delta\beta_{p,r;s} = 2\pi N/\Lambda \quad (4.4.13)$$

where N is a positive integer. The SH power is then

$$P_{2\omega}^{s,N}(L) = \frac{256 \omega^2 d^2 n_{\text{eff}}^{\omega,p} n_{\text{eff}}^{\omega,r}}{9\pi^4 h \varepsilon_0 c_0^3 \varepsilon_\omega^4 (n_{\text{eff}}^{2\omega,s})^3} P_\omega^p P_\omega^r \Gamma_{p,r;s} L^2 \frac{\sin^2(\pi N s_0/\Lambda)}{N^2}. \quad (4.4.14)$$

From this relation it is apparent that the the last term, $\sin^2(\pi N s_0/\Lambda)/N^2$, includes the dependence on domain size discrepancy as well as QPM order N . For the case of equal domain sizes, $s_0/\Lambda = 1/2$, we retrieve relation 8.3.10, where only odd QPM orders are possible. In order to compare SH efficiencies for different QPM orders N as a function of s_0/Λ we define a normalized efficiency as

$$\frac{P_{2\omega}^N(s_0)}{P_{2\omega}^1(s_0 = \Lambda/2)} = \frac{\sin^2(\pi N s_0/\Lambda)}{N^2}. \quad (4.4.15)$$

In Fig. 4.4.5 square root of this relation is presented as a function of s_0/Λ . We see that for a random value of s_0/Λ there exist odd as well as even QPM orders. The highest efficiency for a chosen QPM order N is proportional to $1/N^2$.

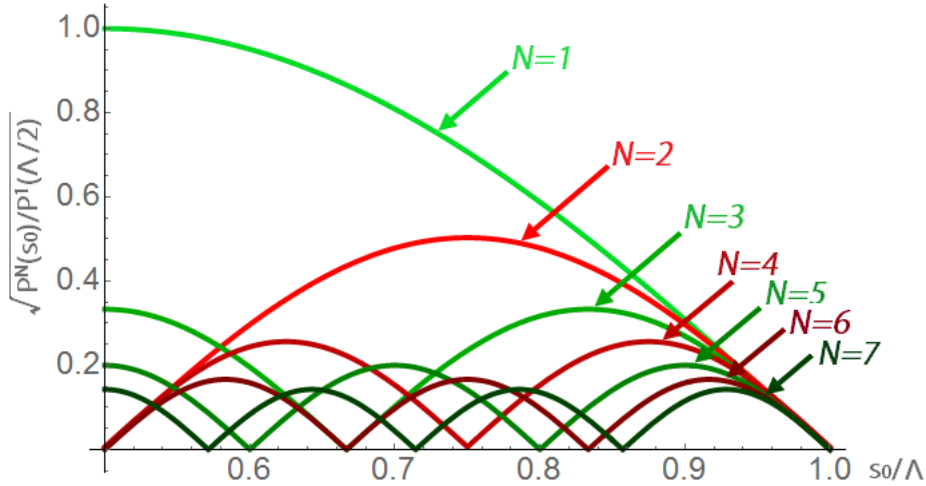


Figure 4.4.5: Higher order QPM ($N = 1, 2, 3, 4$) efficiencies as a function of the ratio s_0/Λ .

In the growth procedure the above described error was the prominent one. So, the opposite polarity domains had slightly different but constant lengths. This type of error again affects the QPM efficiency more for higher orders N .

4.5 Second harmonic generation of ultrashort pulses

So far, only one frequency component was considered to generate a second harmonic wave. Since in experimental part short pulses with a broad frequency spectrum

were used as a pump light source, we want to explore if and under what conditions monochromatic wave approximation provides sufficient description of SHG. We therefore investigate the second order nonlinear conversion of transform-limited fundamental harmonic (FH) pulses with central frequency ω_0 , that generate second harmonic (SH) optical pulses centered around $2\omega_0$ [55, 56]. We will use notation ω_1 for the frequencies of the fundamental pulse and ω_2 for the frequencies of the SH pulse. The derivation is done for the case of a bulk material due to its simplicity. The analysis is further simplified for the case of AlN waveguide by taking into account only the nonlinear coefficient d_{33} and z-polarized electric fields.

Let the z-component of the electric field of the FH pulse at position $x = 0$ be described by a Gaussian function

$$E_{\text{FH}}(0, t) = \frac{1}{2}E_0 e^{i\omega_0 t} e^{-t^2/\tau^2} + c.c., \quad (4.5.1)$$

where τ defines the pulse duration, or in frequency domain, a bandwidth. The electric field in frequency domain is then

$$E_{\text{FH}}(0, \omega_1) = \frac{1}{2}\sqrt{\pi}E_0\tau e^{-(\omega_1-\omega_0)^2\tau^2/4}. \quad (4.5.2)$$

Such a field induces nonlinear polarization oscillating with frequencies centered around $2\omega_0$. A contribution to the chosen spectral component $P^{\text{NL}}(\omega_2)$ comes from all the pairs of FH frequencies whose sum equals ω_2 . Considering that the medium is negligibly dispersive in d_{33} we then have [56]

$$P^{\text{NL}}(x, \omega_2) = d_{33} \int_{-\infty}^{+\infty} E_{\text{FH}}(x, \omega_1) E_{\text{FH}}(x, \omega_2 - \omega_1) d\omega_1 + c.c.. \quad (4.5.3)$$

By explicitly writing the x-dependence of the electric fields, (4.5.3) can be rewritten into

$$P^{\text{NL}}(x, \omega_2) = d_{33} \int E_{\text{FH}}(\omega_1) E_{\text{FH}}(\omega_2 - \omega_1) e^{i[k(\omega_1) + k(\omega_2 - \omega_1)]x} d\omega_1 + c.c.. \quad (4.5.4)$$

Since FH pulse is spectrally located around frequency ω_0 , the wave vector can be expanded in Taylor series around ω_0

$$k(\omega_1) = k_1 + k'_1(\omega_1 - \omega_0) + k''_1(\omega_1 - \omega_0)^2/2 + \dots, \quad (4.5.5)$$

where $k_1 = k(\omega_0)$, $k'_1 = \frac{\partial k}{\partial \omega_1}(\omega_0)$, and $k''_1 = \frac{\partial^2 k}{\partial \omega_1^2}(\omega_0)$. Higher order terms in the expansion are neglected. We insert (4.5.5) and (4.5.2) into Eq. (4.5.4) and obtain

$$P^{\text{NL}}(x, \omega_2) = \frac{d_{33} E_0^2 \tau^2 \pi^{3/2}}{\sqrt{2(\tau^2 - i2k''_1 x)}} e^{-(\omega_2 - 2\omega_0)^2 \tau^2 / 8} e^{i[2k_1 + k'_1(\omega_2 - 2\omega_0) + \frac{k''_1}{4}(\omega_2 - 2\omega_0)^2]x} + c.c.. \quad (4.5.6)$$

We can now solve the nonlinear wave equation 4.2.1 for the SH electric field. We take the ansatz for the SH solution as

$$E_{\text{SH}}(x, \omega_2) = \frac{1}{2}E_0^{\text{SH}}(x, \omega_2) e^{ik(\omega_2)x} + c.c., \quad (4.5.7)$$

where $E_0^{\text{SH}}(x, \omega_2)$ is the electric field amplitude. Since the SH spectrum is located around $2\omega_0$ we can expand the wave vector $k(\omega_2)$ around $2\omega_0$

$$k(\omega_2) = k_2 + k'_2(\omega_2 - 2\omega_0) + \frac{k''_2}{2}(\omega_2 - 2\omega_0)^2 + \dots, \quad (4.5.8)$$

where $k_2 = k(2\omega_0)$, $k'_2 = \frac{\partial k}{\partial \omega_2}(2\omega_0)$, and $k''_2 = \frac{\partial^2 k}{\partial \omega_2^2}(2\omega_0)$. Taking this into account we insert the ansatz Eq. 4.5.7 into the nonlinear wave equation 4.2.1 and obtain

$$\frac{\partial E_0^{\text{SH}}(x, \omega_2)}{\partial x} = \frac{-i\sqrt{\pi^3}\mu_0\omega_2^2 d_{33} E_0^2 \tau}{k(\omega_2)\sqrt{2 - i4k''_1 x/\tau^2}} e^{-(\omega_2 - 2\omega_0)^2 \tau^2 / 8} e^{i\Delta K(\omega_2)x}, \quad (4.5.9)$$

where we introduced the phase mismatch term

$$\Delta K(\omega_2) = \Delta k_0 + \Delta k'(\omega_2 - 2\omega_0) + \Delta k''(\omega_2 - 2\omega_0)^2. \quad (4.5.10)$$

The coefficients of $\Delta K(\omega_2)$ include phase mismatch between center frequencies, $\Delta k_0 = 2k_1 - k_2$, group velocity mismatch, $\Delta k' = k'_1 - k'_2$, and the mismatch of the group velocity dispersion, $\Delta k'' = \frac{k''_1 - 2k''_2}{4}$. Next we integrate Eq. (4.5.9) over x-coordinate from 0 to crystal length L and obtain

$$E_0^{\text{SH}}(L, \omega_2) = \frac{\sqrt{\pi^3}\mu_0\omega_2^2 d_{33} E_0^2 \tau}{k(\omega_2)\sqrt{2}} e^{-\frac{(\omega_2 - 2\omega_0)^2 \tau^2}{8}} e^{\frac{\Delta K(\omega_2)\tau^2}{2k''_1}} F(\omega_2, L), \quad (4.5.11)$$

where

$$F(\omega_2, L) = \frac{\text{Erf}\sqrt{\frac{\Delta K(\omega_2)}{2k''_1/\tau^2}} - \text{Erf}\sqrt{\frac{\Delta K(\omega_2)}{2k''_1/\tau^2}}(1 - i\frac{2k''_1 L}{\tau^2})}{\sqrt{\Delta K(\omega_2)2k''_1/\tau^2}}. \quad (4.5.12)$$

Using (4.5.11) we can derive the SH power per frequency interval as

$$P^{\text{SH}}(L, \omega_2) = \frac{-\mu_0^2 \omega_2^6 d_{33}^2 P_0^2}{S c_0^2 \varepsilon(\omega_2)} e^{-(\omega_2 - 2\omega_0)^2 \tau^2 / 4} \frac{F(\omega_2, L) F^*(\omega_2, L)}{\Delta K(\omega_2) 2k''_1 / \tau^2}, \quad (4.5.13)$$

where S presents the cross section of the light beam. The total optical power of the SH pulse is obtained by integrating 4.5.13 over the entire frequency interval

$$P^{\text{SH}}(L) = \int_{-\infty}^{\infty} P^{\text{SH}}(L, \omega_2) d\omega_2. \quad (4.5.14)$$

The dependence of the SH spectrum on propagation distance L is governed by the last term in 4.5.13, and is graphically presented in Fig. 4.5.1. The calculations are carried out with the following parameters, FH center frequency $\omega_0 = \pi \cdot 10^{15}$ Hz, center wavelength $\lambda_0 = 600 \text{ nm}$ and pulse length $\tau = 30 \text{ fs}$. Phase matching is assumed to be established between the central FH and SH frequencies, $\Delta k_0 = 0$. We took $\Delta k' = 10^{-9} \text{ s/m}$, $\Delta k'' = 10^{-25} \text{ s}^2/\text{m}$ and $k''_1 = 7 \times 10^{-25} \text{ s}^2/\text{m}$ that were calculated from refractive index dispersion in AlN material [25]. The normalized SH power spectrum $P^{\text{SH}}(L, \omega_2)/P^{\text{SH}}(L, 2\omega_0)$ is plotted at different distances in the

crystal L . We see that for very short crystals (in the limit $L \rightarrow 0$) the SH spectrum is broad with $\omega_{\text{FWHM}} = 3.3/\tau$ (FH pulse has $\omega_{\text{FWHM}} = 2.4/\tau$). When increasing L the spectrum gets narrower and some oscillations appear at the main peak edges. In practical experiment where $L \geq 1 \text{ mm}$ the spectral width becomes $\omega_{\text{FWHM}} \leq 0.14/\tau$, which means that only a small spectral part of the initial FH pulse converts to SH pulse.

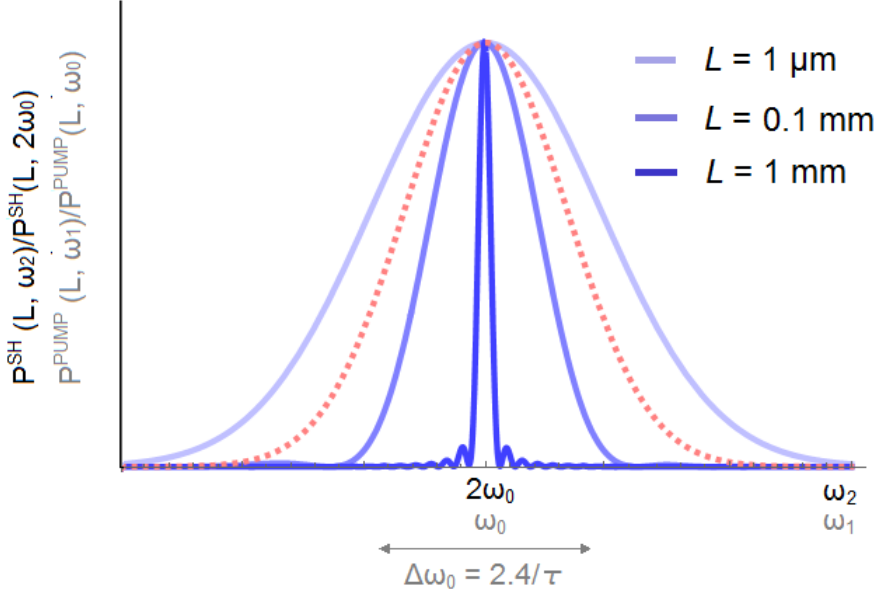


Figure 4.5.1: SH power spectra as a function of position in crystal for $L = 1 \mu\text{m}$, $100 \mu\text{m}$ and 1 mm (blue lines). Red dotted line shows the spectrum of a Gaussian FH pulse centered around ω_0 with $\text{FWHM} = 2.4/\tau$. For the calculations, the following parameters were used, $\omega_0 = \pi \cdot 10^{15} \text{ Hz}$, $\tau = 30 \text{ fs}$, $\Delta k_0 = 0$, $\Delta k' = 10^{-9} \text{ s/m}$, $\Delta k'' = 10^{-25} \text{ s}^2/\text{m}$ and $k_1'' = 7 \times 10^{-25} \text{ s}^2/\text{m}$.

Fig. 4.5.2 shows the dependence of the total SH power on propagation distance L that was calculated from the relations 4.5.13 and 4.5.14 by using the above listed parameters. In the presented range of propagation distances the power increases but its slope decreases with L that is in accordance with the narrowing of the SH spectrum.

The obtained results can be applied for the waveguide geometry. Instead of the plane waves we utilize the solutions representing the waveguide modes. It is expected that the spectral dependence of the SH wave on the propagation distance remains the same. Instead of the wavevectors k_1 and k_2 the appropriate propagation constants β_ω and $\beta_{2\omega}$ have to be taken into account. Besides, the electric fields of the waveguide modes vary in the z -direction, therefore we deduce that the Eq. 4.5.13 should be multiplied by the suitable overlap integral.

On completion of the theoretical part I summarize the main bibliographic sources I have followed. The description of SHG in various waveguide structures was taken from the literature. Modal dispersion phase matching in waveguides is presented in

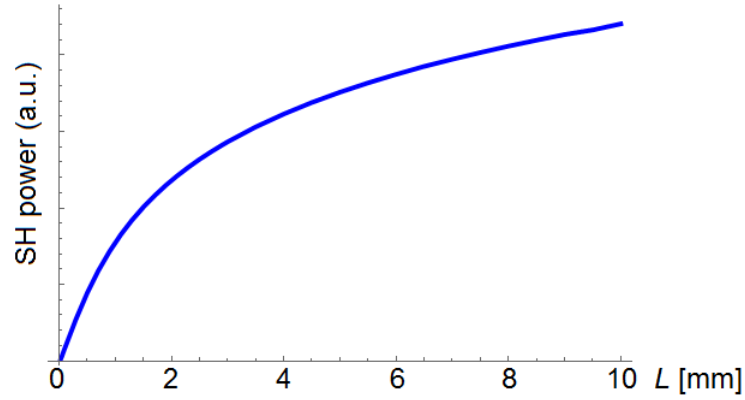


Figure 4.5.2: The dependence of the total SH power as a function of propagation distance L by using the following parameters $\omega_0 = \pi \cdot 10^{15}$ Hz, $\tau = 30$ fs, $\Delta k_0 = 0$, $\Delta k' = 10^{-9}$ s/m, $\Delta k'' = 10^{-25}$ s²/m and $k_1'' = 7 \times 10^{-25}$ s²/m.

the work of Park et. al. [30]. My contribution includes the simplification of the overlap integrals using the assumption of perfect confinement of waveguide modes [34]. Quasi phase matched SHG including domain size errors for the case of bulk material was taken from [54]. By using waveguide geometry I derived similar results. Ultra short pulse SHG is nicely presented in the work of G. Imeshev et. al [56], where the general derivation is given and some particular cases of different pump mode shapes are calculated numerically. The obtained analytical expression based on the assumptions of a transform limited pump beam spectrum and the Taylor series expansion of the wavevectors to the second order was done by myself.

Chapter 5

Experimental

5.1 Laser system

The SHG measurement were performed using a femtosecond laser system. Its high peak power is important for efficient SHG and its tunable wavelength is necessary for investigation of the phase matched points that are spread over appreciable spectral interval. The tunable femtosecond laser system has three units: an optical oscillator, a regenerative amplifier and an optical parametric amplifier and will be described in the next paragraphs.

The first unit is a Ti:sapphire optical oscillator (Coherent Mantis). It is optically pumped by a frequency doubled semiconductor laser emitting at 532 nm. Light amplification takes place inside Ti:sapphire crystal. The oscillator itself employs Kerr lens mode locking to generate around 40 fs long pulses with central wavelength of 800 nm and a repetition rate of 80 MHz. Its average power is around 550 mW.

In the next stage the oscillator output is fed to an amplifier system (Coherent Legend Elite). It uses the regenerative chirped pulse amplification technique in which the initially short pulse is first stretched in time then amplified and compressed back to its initial duration. The stretcher assembly comprises a dispersive line (combination of gratings and mirrors), so that continuous spread in time delay of the spectral components is achieved. The duration of the incoming pulse is stretched up to 10^4 times in order to reduce the pulse peak intensity. The principle of regenerative amplification is to trap a single stretched pulse selected from the modelocked train and amplify it in the laser cavity. The pulse is kept in the resonator until all of the energy stored in the amplification crystal (Ti:sapphire laser rod) optically excited by a pulse from frequency doubled Nd:YLF laser is extracted. The pulse multipasses the rod resulting in the overall gain of about 10^6 . Trapping and extracting the pulse in and out of the resonator is done by using Pockels cells and a broad-band polarizer. Finally, the pulse is recompressed to its original duration. At output 30 - 60 fs long pulses with repetition rate of 1 kHz and average energy of 3 mJ are produced.

The third component consists of a white light continuum generator and subsequently a two stage parametric amplifier that enables wavelength tuning. Before the first amplification stage a portion of the input light beam is used to produce white-

light continuum in a sapphire plate. The white light and another fraction of the pump beam are focused onto the nonlinear crystal, where parametric amplification takes place. Only the signal beam is transported and further amplified in the second amplification stage. The wavelength is selected by setting the delay between the optical beams before reaching the nonlinear crystal where the amplification takes place, and changing crystal angles to optimize phase matching. As a result the outputs are signal and idler beams with tunable central wavelengths. The wavelength of the signal beam ranges from 1175 nm to 1600 nm, and the idler wavelength can be tuned from 1600 nm to 2600 nm. For the conversion to the visible and UV spectral range, the frequency converters are used including the frequency doubling, the sum frequency generation and the difference frequency generation. As a result, the output pulses can be tuned to attain central wavelengths from 290 nm to 1150 nm. The system's repetition rate is 1 kHz, pulse length 30 - 60 fs, and spectral width 30 nm (FWHM). Energy per pulse ranges from 1 to 100 μJ and depends on the chosen wavelength. The intensity profile of the outgoing light is Gaussian and its quality depends on the settings within the laser system.

5.2 Detection system

The detection system for the analysis of the SH signal consists of a spectrograph and a CCD with photon counting capability. The SpectraPro-2300i spectrograph with three different gratings was used: 1200 grooves per mm with the blaze wavelength of 500 nm, 600 grooves per mm with the blaze wavelength 1 μm and UV optimized holographic grating with 1200 grooves per mm. The intensity of the spectrally separated signal was measured with an Andor iStar CCD camera. It was operated in a gated mode and was synchronized with the femtosecond system's repetition rate. The width of the detection gate was adjusted to obtain the maximal signal and was set to 20 ns.

5.3 Setup

The experimental setup for measuring second harmonic generation is presented in Fig. 5.3.1. A low power HeNe laser was used to align the setup. Its output was guided to the sample where it was end-fire coupled into the waveguide using an in-coupling lens. Depending on the waveguide dimensions, lenses with different focal lengths (25 mm and 100 mm) were used in order to adjust the beam width at the waveguide end. The sample was held on a sample holder that enabled adjustments in xyz-directions. Coupling was controlled by a CCD camera above the sample. The outgoing light was collected and collimated with an out-coupling lens with focal length of 8 mm. Light was led to the detector system comprising of a spectrograph with a CCD camera. A lens with focal length of 25 mm was used to focus the beam into the spectrograph slit.

The defined beam path was marked by two pinholes positioned in front of the coupling system. The laser system producing femtosecond pulses with tunable central wavelengths was then aligned to match the HeNe beam path. Its output power was controlled by the variable neutral density filter. The out-coupled pump light was suppressed by using appropriate filters, and the remaining SH light was led to a detector system.

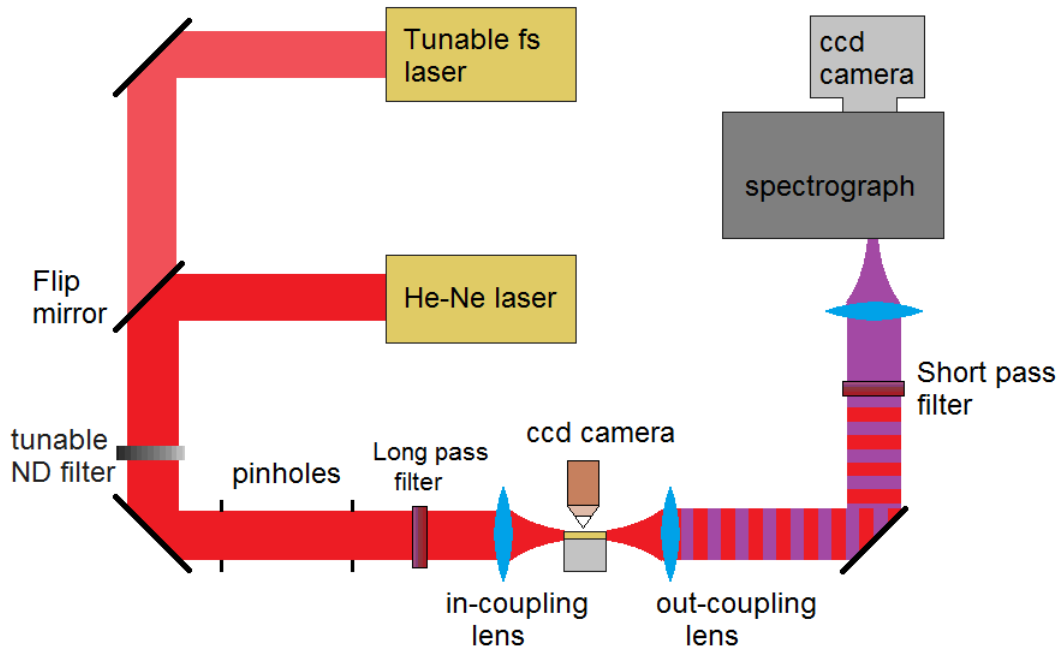


Figure 5.3.1: Experimental setup.

Chapter 6

Second harmonic generation in AlN waveguides

6.1 Introduction

This chapter provides experimental results of measurements of second harmonic generation in different AlN waveguides. The first SHG measurements were carried out using single polar AlN waveguides, where phase matching is achieved through MDPM. The different waveguide modes propagate with different propagation constants therefore certain combination of pump and SH modes can be phase matched. The progress in the growth technique provided good quality LPS waveguides with $10\ \mu\text{m}$ periodicity that were investigated for SHG. Different waveguide modes can be phase matched due to the additional phase shift provided by the periodical structure. Consequently, phase matching occurs as a combination of MDPM and QPM. The detailed description of MDPM and QPM SHG is given in Chapter 3. The final experimental examination was done using the LPS waveguides with $1.2\ \mu\text{m}$ periodicity, where larger propagation losses were present and prevented the observation of SH light.

6.2 Single polar AlN waveguides

Single polar AlN waveguides were fabricated first in order to probe them for second harmonic generation through modal dispersion phase matching. The used waveguides were rectangular and were fabricated from the planar AlN film (its growth is described in Chapter 2) by the standard photolithography process as follows. First the AlN film was coated with a photoresist. Next a metal mask with several areas containing different widths of $2\ \mu\text{m}$, $5\ \mu\text{m}$, $10\ \mu\text{m}$ and $20\ \mu\text{m}$ was placed on top of it. The sample was exposed to UV light and the unprotected parts of the photoresist dissolved afterwards during developing. In the following step the AlN film not covered with the photoresist was etched by plasma and reactive-ion-etching process. Finally, the remaining photoresist was removed by acetone. The final sample consisted of the rectangular waveguides with the thickness $h = 550\ \text{nm}$ and widths $w = 2, 5, 10$ and

20 μm (see Fig. 6.2.1). The rectangular waveguides used in our experiment were

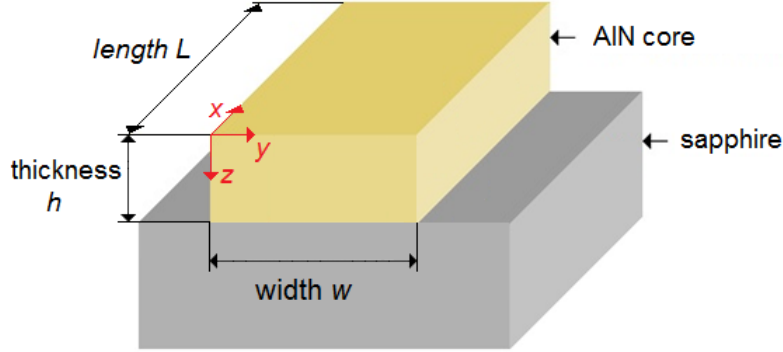


Figure 6.2.1: A sketch of an rectangular AlN waveguide with thickness h , width w and length L .

10 μm wide. The preparation of the waveguides of certain length was done by the following procedure. In order to get a smooth front and end surfaces, we used a UV laser to inscribe parallel lines normal to the waveguide direction at the sapphire side of the wafer, along which the samples were cleaved afterwards. The length of the waveguides was around 3 mm.

The laser beam was focused onto the front face of the waveguide using a lens with a 10 mm focal length. The diameter of the beam at the waveguide facet was around 10 μm , equal to the waveguide width, in order to excite dominantly the fundamental mode in the y -direction (see Fig. 6.2.1). The polarization was chosen such that the TM modes were excited.

The possible modal phase matching conditions are shown in Fig. 6.2.2 with a horizontal axis showing pump and SH wavelengths. The refractive index values for the AlN thin films are taken from the ellipsometry measurements and extrapolated to UV spectral region [25]. The dispersion relation for sapphire is taken from the literature [59]. As expected, the SH modes have a higher n_{eff} , that decreases faster as the mode order increases. Figure 6.2.2 shows n_{eff} for the two lower-order modes of the pump wavelength, as well as the average value of the two. Both the pump and SH modes show normal dispersion. Dotted lines are added in order to show the limits of n_{eff} represented by the refractive indices of bulk AlN and sapphire. At wavelengths where the n_{eff} curves for the pump and SH intersect, the phase matching condition, $\Delta\beta_{p,r,s} = 0$, is satisfied. Out of all the intersections, the three marked with circles are the ones with a relatively large overlap integral, as seen in Table 4.1. The other four intersections, labeled with squares, have negligible overlap integrals.

The explanation for the use of the planar waveguide approximation is given by the following consideration. Firstly, the pump used was a well centered Gaussian beam with a diameter equal to the waveguide width, therefore mainly the y -direction-zero-order mode was excited. The amplitudes of the higher-order modes decrease with increasing order. The situation is similar with higher SH modes where only the low-order modes have to be considered due to very low overlap integrals with the pump.

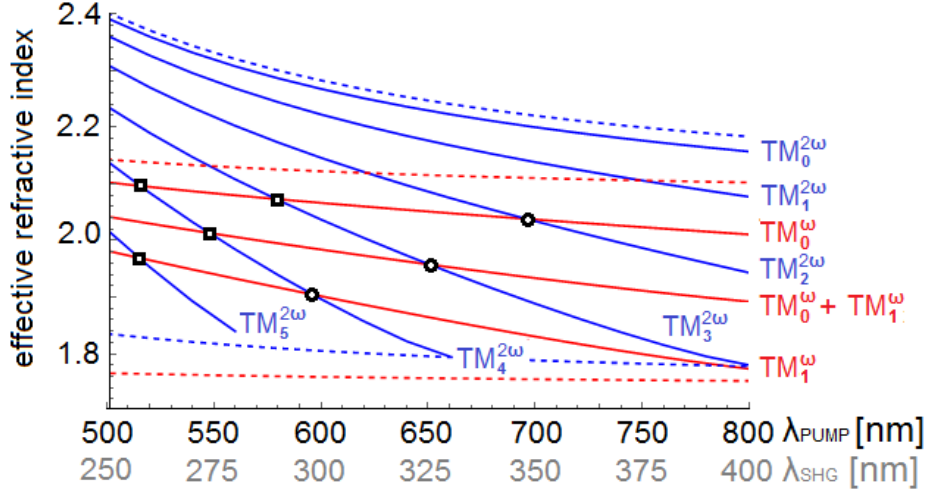


Figure 6.2.2: The dispersions of n_{eff} for the pump (red lines) and SH (blue lines) waveguide modes in AlN planar waveguide with a thickness of 550 nm. Dotted lines represent the dispersions of the extraordinary refractive indices of bulk AlN and sapphire. At wavelengths where blue and red lines intersect, phase matching occurs. The black circles indicate the MDPM interactions with significant overlap integrals which are responsible for the experimentally observed SH signal. The other four interactions marked with squares, have negligible overlap integrals.

Secondly, due to a large width to thickness ratio (18:1) the y-direction-low-order modes propagate with n_{eff} very close to the n_{eff} of the zero-order mode and therefore do not affect the phase matching intersection points considerably, as is schematically shown in Fig. 6.2.3.

6.2.1 Measurements

In order to check the waveguide quality, a SEM image of an AlN waveguide was taken and is shown in Fig. 6.2.4. The front and top surfaces are almost atomically smooth whereas the side walls exhibit a relatively rough surface. This is in agreement with Fig. 6.2.4b that shows the scattering of a HeNe laser light coupled into the waveguide. The image was taken by a CCD camera above the sample. Scattering is observed from the front surface and along the waveguide arising from random but low density defects on the top surface, and from the sidewalls. From a set of the produced waveguides only the smoothest were used for SHG.

The results of the SHG measurements are presented in Fig. 6.2.5. We observed three main SH peaks at wavelengths of 306 nm, 331 nm and 356 nm that we assign to mode-combinations $2\text{TM}_1^\omega \rightarrow \text{TM}_4^{2\omega}$, $\text{TM}_0^\omega + \text{TM}_1^\omega \rightarrow \text{TM}_3^{2\omega}$ and $2\text{TM}_0^\omega \rightarrow \text{TM}_2^{2\omega}$ respectively, marked with circles in Fig. 6.2.2. The excitation of the zero and first order pump mode was accomplished by slightly shifting the in-coupling lens in the z-direction.

The SHG spectra presented in Fig. 6.2.5 show some structure in addition to

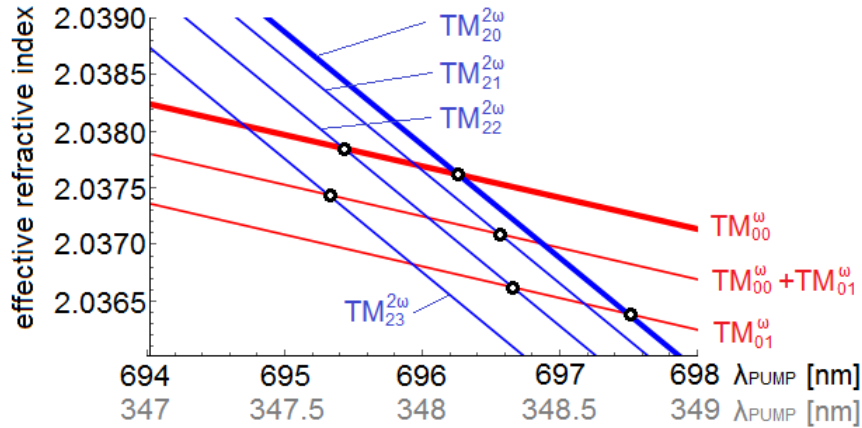


Figure 6.2.3: The dispersions of n_{eff} for the pump (red lines) and SH (blue lines) waveguide modes in AlN rectangular waveguide with a thickness of 550 nm and width of 10 μm . The planar waveguide modes TM_0^{ω} and $\text{TM}_2^{2\omega}$ present a good approximation of the zero order y-modes in rectangular waveguide, TM_{00}^{ω} and $\text{TM}_{20}^{2\omega}$, respectively (bold lines). Besides, the first order y-mode of the pump wave is taken into account, thus two dispersion curves are added for TM_{01}^{ω} and $\text{TM}_{00}^{\omega} + \text{TM}_{01}^{\omega}$. The dispersions of n_{eff} for four lowest order SH modes are shown due to the significant overlap integrals (marked with circles) with the considered pump modes. The calculations were done using Marcatilli method [58].

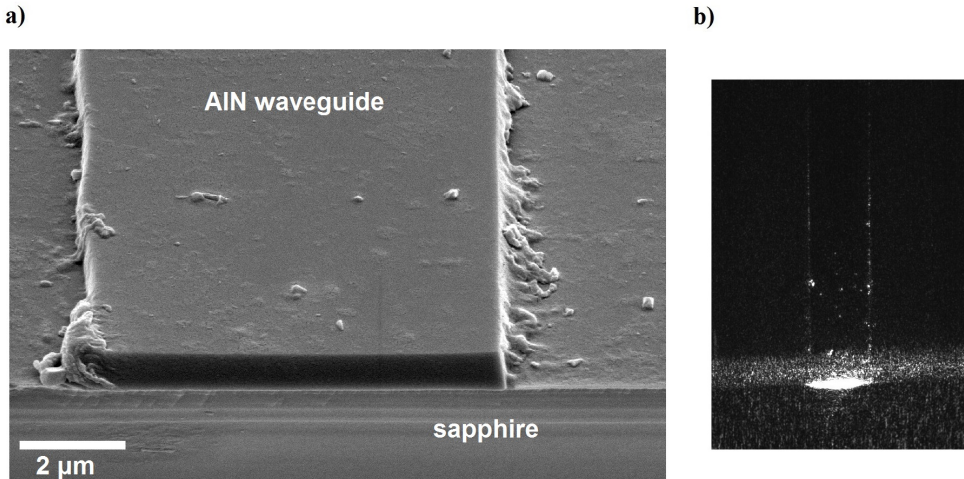


Figure 6.2.4: a) SEM image of a rectangular AlN waveguide on sapphire substrate. b) Picture taken by a camera above the sample showing light coupling and scattering of a HeNe laser beam. The horizontal scattering line is coming from the sapphire substrate.

the main peaks. This structure was studied in more detail and is presented in Fig. 6.2.6. For the SHG peak at 356 nm, the pump spectrum was varied in the vicinity of the MDPM wavelength in order to observe the change of the structure of the SH

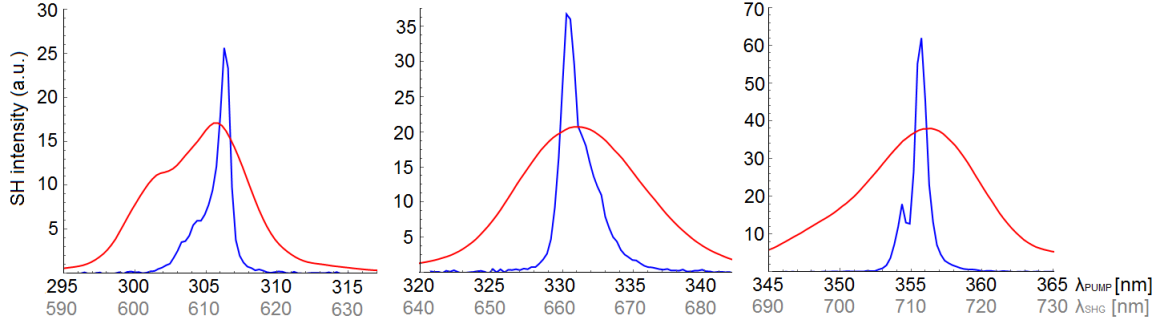


Figure 6.2.5: Second harmonic generation spectra in rectangular Al-polar AlN waveguide with thickness of 550 nm and width of 10 μm for three different pump center wavelengths. Blue curves show the SH spectra and the red curves the pump spectra. The SH response is a consequence of MDPM between the mode combinations a) $2 \text{TM}_1^\omega \rightarrow \text{TM}_4^{2\omega}$, b) $\text{TM}_0^\omega + \text{TM}_1^\omega \rightarrow \text{TM}_3^{2\omega}$ and c) $2 \text{TM}_0^\omega \rightarrow \text{TM}_2^{2\omega}$ denoted with circles in Fig. 6.2.2.

response. The maximum power of the SH signal was observed for the pump spectrum with central wavelength at 713 nm (Fig. 6.2.6(c)), which is in good agreement with the predicted MDPM. A lower intensity side peak on the shorter wavelength side of the main SH peak can be observed in Figs. 6.2.6 (a)–(d). We explain this peak as the nonlinear coupling of the fundamental modes TM_{00}^ω and TM_{01}^ω with the SH mode $\text{TM}_{01}^{2\omega}$, where the second number in subscript defines the number of nodes in the y-direction. The effective refractive index of the y-excited mode is slightly lower than the fundamental mode in the y-direction, therefore a peak is observed at a shorter wavelength. Keeping this in mind we can amend Fig. 6.2.2 by adding additional curves for the y-excited modes for both the fundamental and SH modes. One example is shown in Fig. 6.2.3. The number of intersections increases and additional spectral features may appear, as observed in Fig. 6.2.6. Additional support for our explanation comes also from the observation that the SH spectrum varies with focusing and lateral displacement of the pump beam, therefore exciting higher-order modes.

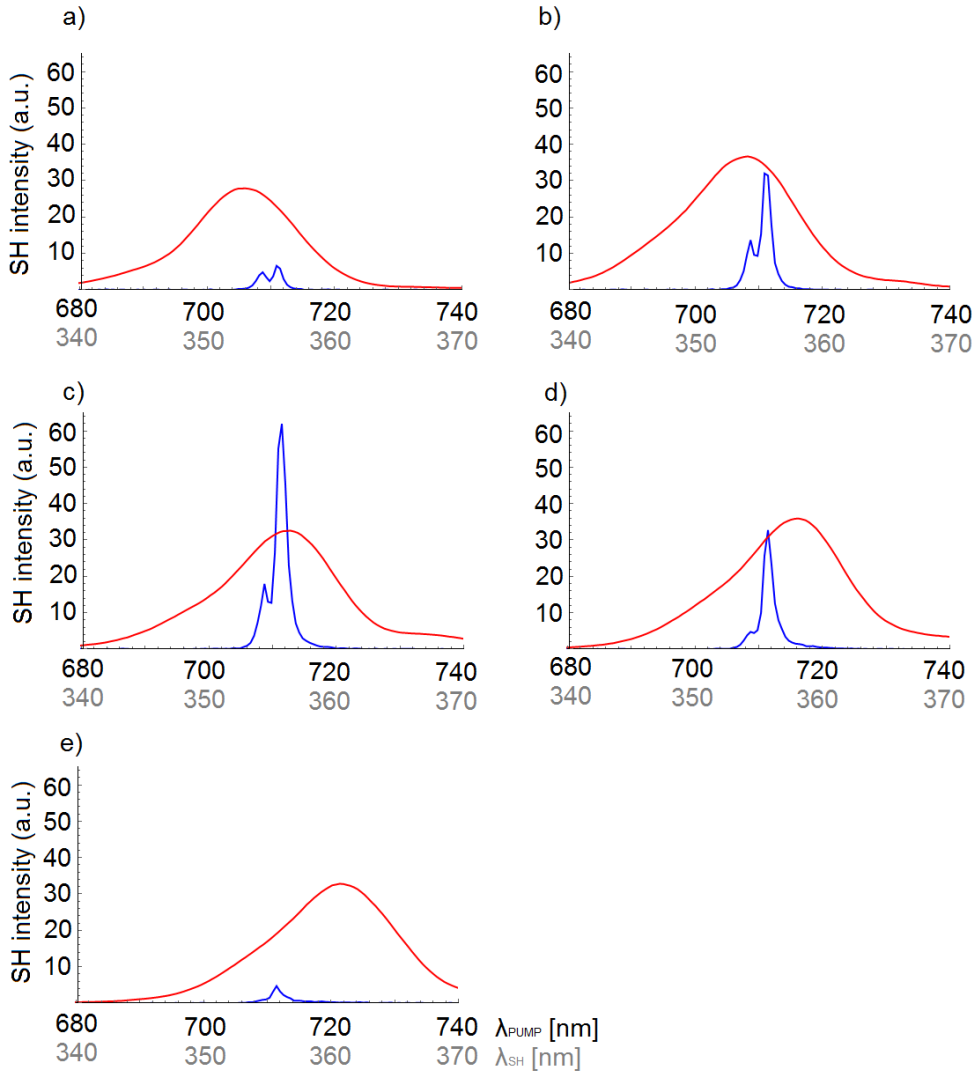


Figure 6.2.6: The SH response in 550 nm thick and 10 μm wide Al-polar AlN waveguide at different central wavelengths of the pump wave spectra. The blue lines show the spectrum of the SH signals and the red lines show the pump spectra. The strong SH peak at around 356 nm is (dis)appearing and reaches its maximum c) when the pump wavelength is centered at twice the SH wavelength, 712 nm. It originates from the interaction $2 \text{TM}_{00}^{\omega} \rightarrow \text{TM}_{20}^{2\omega}$. A smaller SH peak at around 354 nm is supposed to occur due to the interaction of higher order modes, most likely due to the interaction $2 \text{TM}_{02}^{\omega} \rightarrow \text{TM}_{26}^{2\omega}$.

6.3 Lateral polar structure-based AlN waveguides

Lateral polar structured AlN waveguides were investigated in order to search for quasi phase matched second harmonic generation. As explained in Section 4.4 the periodicity of LPS determines the wavelength where phase matching occurs. For planar LPS-based waveguides the dependence of periodicity on the pump (SH) wavelength was plotted in Fig. 4.4.2. In order to convert visible light into UV light through first order QPM, the periodicity should be of the order of $1 \mu m$. The fabricated waveguides that showed adequately smooth surfaces had a relatively large period size $\Lambda = 10 \mu m$. Shorter 1 mm long waveguides were used due to the larger propagation losses compared to single polar AlN waveguides. Waveguides with shorter periodicity of $1.2 \mu m$ were also fabricated.

6.3.1 Theoretical predictions for $10 \mu m$ periodic structured waveguides

The theoretical predictions for phase matching were based on the measured thickness of the waveguides. The thickness varies across the sample and was measured to be (500-600) nm. For the calculations I picked the value of 590 nm within that interval that best agrees with the experimental results. The analysis of phase matching in 590 nm thick LPS AlN waveguide is presented in Fig. 6.3.1 using the planar waveguide model. Its justification is similar as in the case of single polar waveguides. In LPS-based waveguides QPM occurs as presented in Chapter 4. In the shown wavelength range two lowest order pump modes can propagate with the corresponding effective refractive index dispersions shown with red. In addition their average value is also plotted. The four lowest order SH modes shown with blue can be phase matched with pump modes through several QPM orders N . Fig. 6.3.1 shows:

- a) the dispersion of n_{eff} for the SH mode $s = 0$ and $N = 1, 2, \dots, 11$,
- b) the dispersion of n_{eff} for the SH mode $s = 1$ and $N = 1, 2, \dots, 9$,
- c) the dispersion of n_{eff} for the SH mode $s = 2$ and $N = 1, 2, \dots, 7$ and
- d) the dispersion of n_{eff} for the SH mode $s = 3$ and $N = 1$,

where the odd (even) QPM orders are presented with the solid (dashed) curves. Even QPM orders occur only when the two opposite polarity domains are of different lengths. The crossing points correspond to phase matched interactions, where the combinations with appreciable efficiency are labeled with circles. Due to the large number of phase matched interactions, a clear presentation of phase matching points as a function of wavelength is given in Fig. 6.3.2. The vertical axis shows the efficiency of the interaction calculated from the relation

$$\eta = \Gamma_{p,r;s} \frac{\sin^2(\pi N s_0 / \Lambda)}{N^2} \quad (6.3.1)$$

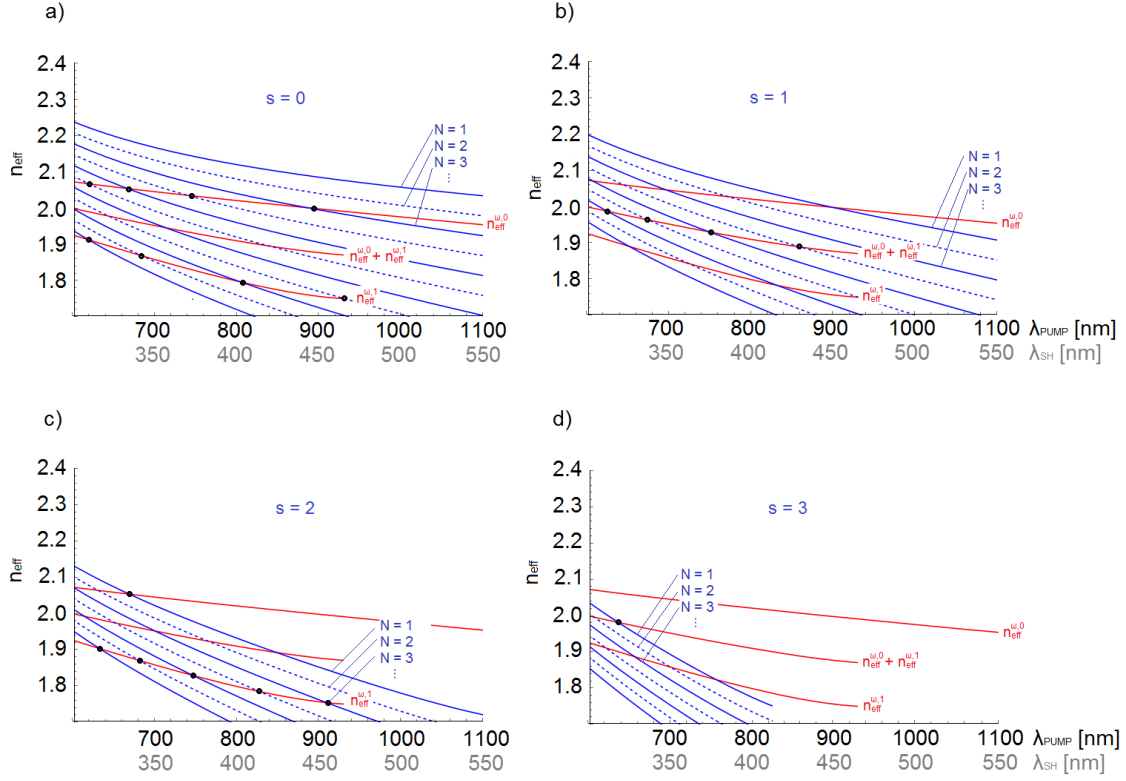


Figure 6.3.1: Phase matching points in structured AlN waveguide for quasi phase matching with periodicity $\Lambda = 10 \mu m$ and thickness of 590 nm. Red curves show the effective refractive index dispersions of the pump modes. Blue curves show the dependence $n_{\text{eff}}^s - N \frac{\lambda}{2\Lambda}$ for four lowest order SH modes s (from a) - d), respectively), where each SH mode couples to the pump through several QPM orders N .

that is a product of the MDPM efficiency defined by overlap integral $\Gamma_{p,r;s}$ and QPM efficiency depending on N and the duty cycle $s_0/(\Lambda - s_0)$. The shown efficiency interval in Fig. 6.3.2 extends from the perfect duty cycle 50:50 to the experimentally observed duty cycle 45:55. Note that for odd QPM orders the efficiency η is maximal for the duty cycle of 50:50 and reverse is true for the even QPM orders. Numbers in brackets of the form $(p, r; s; N)$ denote phase matching points, where p and r denote the interacting pump modes, s denotes SH mode and N is QPM order.

6.3.2 Topography of the rectangular $10 \mu m$ periodic structured waveguides

Before starting SHG experiments the quality of the waveguides was assessed by coupling the HeNe light into the waveguides. Fig. 6.3.3 a) and c) show top view images of two typical waveguides observed across the wafer. Light enters the waveguide from the left where a strong scattering is observed and then propagates within the waveguide with attenuation. Fig. 6.3.3 b) and d) show the corresponding scattering

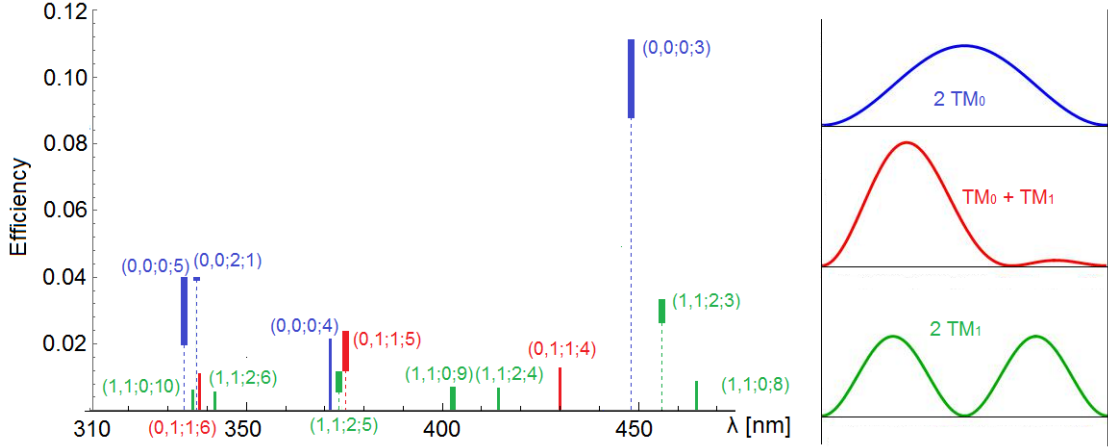


Figure 6.3.2: Phase matching points of a 590 nm thick planar LPS AlN waveguide with 10 μm periodicity as a function of SH wavelength. Numbers in brackets $(p, r; s; N)$ denote waveguide modes of the pump (p and r), SH (s) waves and QPM order N . The efficiency intervals extend from maximum (minimum) at perfect duty cycle 50:50 to minimum (maximum) at the duty cycle of 45:55 for odd (even) N . To distinguish between the odd and even QPM orders, thick and thin lines are used, respectively. From experimental point of view different modes are excited to different extent as determined by the pump beam spatial profile, thus contributing to the total efficiency. Pump mode combinations consisting of the pairs 2 TM_0 , $\text{TM}_0 + \text{TM}_1$ and 2 TM_1 are represented with blue, green and red lines, respectively. On the right side the intensity profiles for different combinations of the pump modes are illustrated.

intensity profiles integrated over the waveguide width for a 150 μm large segments of a 1 mm long waveguides. In case b) a clear periodic pattern of the scattering intensity profile is observed matching the AlN LPS periodicity of 10 μm . The scattering is stronger in one polarity of the domains than in the other. Besides that, there are intensity spikes at the interfaces between the domains. The first observation is in accordance with the known difference in roughness of the polarities, N-polar top surface being rougher than Al-polar [25]. In some waveguides shown in d) different scattering profile is observed indicating different topography of the top surface. The scattering intensity profile appears random on that scale. By fitting the data with exponential function of the form given by Eq. 3.3.1 we obtain the coefficients b) $\alpha = (11 \pm 2)/\text{mm}$ and d) $\alpha = (6.3 \pm 2)/\text{mm}$. Due to the lower scattering losses of the waveguides shown in b) these were used for SHG experiment.

Sample topography was studied in more detail by atomic force microscopy. We used the Veeco Dimension 3100 atomic force microscope at JSI, CENN Nanocenter. It was operating in the tapping mode, where the cantilever is driven to oscillate near its resonance frequency. The interaction forces acting on the cantilever when the tip comes close to the surface cause the amplitude of the cantilever's oscillation to change. Through the electronic mechanism this change is detected and the height of the cantilever is adjusted in order to maintain the set amplitude. The image is

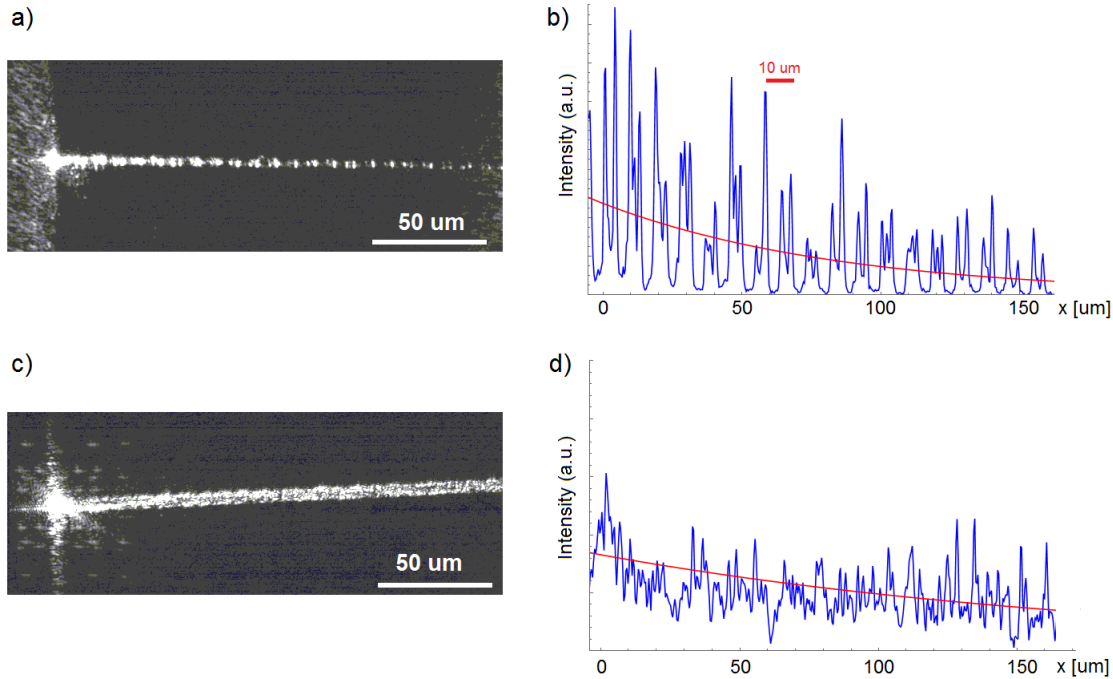


Figure 6.3.3: Light scattering in LPS-based AlN waveguides with $10 \mu\text{m}$ periodicity. Two characteristic scattering intensity profiles were observed across the sample. a) and c) show HeNe light scattering images taken by a CCD camera above the sample. The corresponding graphs b) and d) show scattering intensity profiles as a function of position along the waveguide (blue) and fitted exponential function (red) with $\alpha = (6.3 \pm 2)/\text{mm}$ and $\alpha = (11 \pm 2)/\text{mm}$, respectively.

produced by imaging the force of the intermittent contacts of the tip with the sample surface.

First, waveguide dimensions were measured. The thickness across the sample varied in the range between 500 nm and 600 nm , and their width was constant and equals $5 \mu\text{m}$.

The analysis of the surface topography is presented in Fig. 6.3.4. Image a) shows a $20 \times 20 \mu\text{m}^2$ section with rectangular $5 \mu\text{m}$ wide and 590 nm thick waveguides separated by $5 \mu\text{m}$. The line indicated by green markers extends along the top waveguide surface and the line indicated by red markers runs along the area between adjacent waveguides. The height difference of 590 nm is subtracted from the image in order to show the small variations in roughness occurring at the two surfaces.

The periodical structure of the top waveguide surface is clearly seen. Approximately 80 nm high pairs of bumps are observed with the periodicity of $10 \mu\text{m}$. The cross section of the area between adjacent waveguides shows step-like structure with the height difference of approximately 66 nm . This is the consequence of the different etching rates of the N- and Al- polarities that was performed in KOH solution in order to fabricate rectangular waveguides from the planar film. The etching rates of the N- and Al- polar AlN are $500 \text{ nm}/\text{min}$ and $10\text{-}25 \text{ nm}/\text{min}$, respectively, while

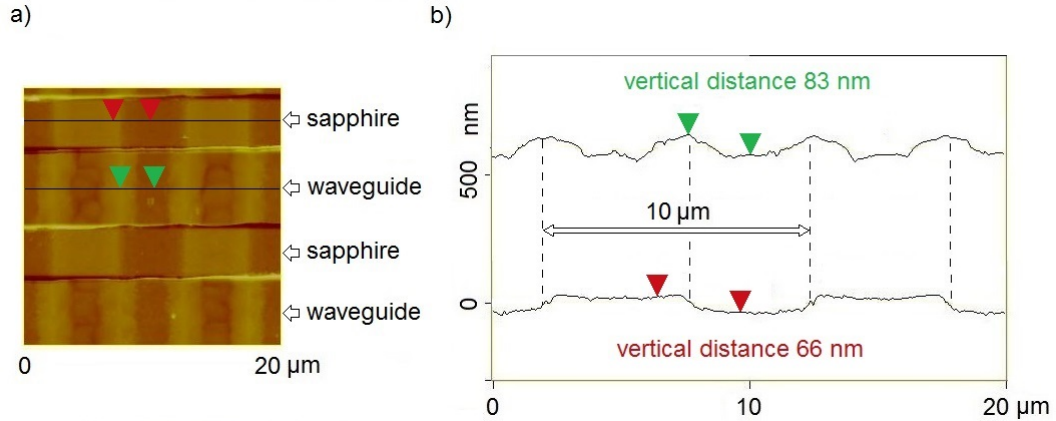


Figure 6.3.4: a) AFM topographic image of a $20 \times 20 \mu\text{m}$ sample with $5 \mu\text{m}$ wide, 590 nm thick LPS-based AlN waveguides with $10 \mu\text{m}$ periodicity. The two lines marked with green and red arrows extend over the waveguide top surface and the region between adjacent waveguides, respectively. b) The corresponding cross-section profiles exhibit periodic structure and the arrows locate the positions such that approximately the highest and the lowest vertical points on the surface are shown. The top waveguide surface exhibits a periodical structure with the period size of $5 \mu\text{m}$ and the height deviations around 83 nm . The intermediate area marked with red clearly shows step like structure with height differences of around 66 nm and $10 \mu\text{m}$ periodicity. The dotted lines denote the boundaries between the N-polar and Al-polar domains. Mean vertical distance of 590 nm between the upper and the lower curve is taken to be the waveguide thickness.

the sapphire etching rate is $1 \text{ nm}/\text{min}$ [57]. From these data the topography of the area between the neighbouring waveguides can be assessed. The initial ($500 - 600$) nm thick LPS film was etched for 40 min , therefore $\sim 39 \text{ nm}$ of sapphire was removed under the N-polar domain. Since the height difference measured along the line b) equals 66 nm and is larger than the depth of the etched sapphire below the N-polar domain 39 nm , obviously the Al-polar domain did not etch completely. From that we estimate that around 27 nm thick layer of Al-polar domain remained unetched which corresponds to the etching rate of the Al-polar AlN to be around $12 \text{ nm}/\text{min}$. Additionally, we see that the ratio between N-polar and Al-polar domain length is around $45 : 55$. However, this value varies across the sample, the highest ratio observed was $60 : 40$. Since it is the lower step that appears shorter, the measured domain length difference could be a very common artefact that occurs due to the finite dimension of the AFM tip, as sketched in Fig. 6.3.5. Since it was shown in papers [61,62] that both domains grow vertically to the substrate, we can extrapolate the position of the domain boundaries from the steps observed on sapphire to the waveguide top surface. Then by looking again Fig. 6.3.4 a) we see that the central area of each domain is approximately of the same height, whereas the bumps occur at the domain boundaries. On the basis of the previous discussion an illustration of the AlN waveguide on sapphire is shown in Fig. 6.3.6.

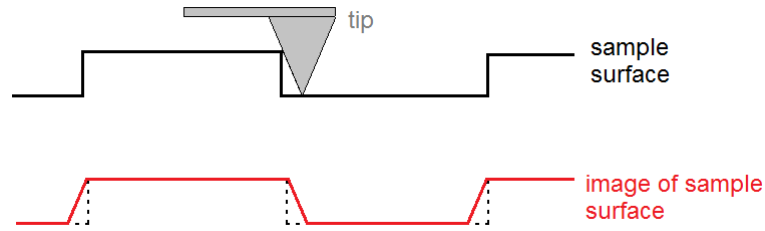


Figure 6.3.5: Resultant image artefact due to tip dimension.

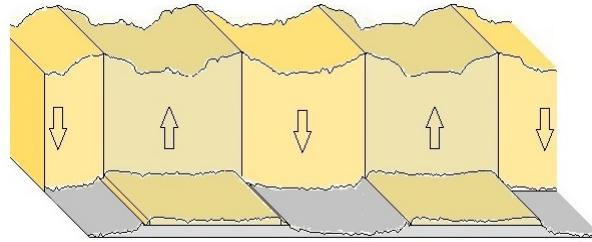


Figure 6.3.6: A drawing of the AlN waveguide and the area between the adjacent waveguides. The arrows show the orientation of the crystallographic c -axis, therefore the arrow pointing up refers to Al-polar and the opposite N-polar AlN.

6.3.3 SHG measurements using rectangular $10 \mu\text{m}$ periodic structured waveguides

Light was end-fire coupled into the waveguide with a lens having focal length of 25 mm. The beam diameter entering the waveguide was around $5 \mu\text{m}$ equal to their width in order to fit the zero-order y -mode.

SH measurements were done by varying the pump beam central wavelengths between 680 nm and 1000 nm. The selection of these spectral interval was based on the expected phase matching wavelengths presented in Section 6.3.1. When decreasing pump wavelength the intensity of the measured SH signal decreased and below 680 nm no SHG was detected anymore. This could be explained with the fact that propagation losses that increase with decreasing light wavelength become too high.

Before presenting the measurements in detail let me give a general remark to the experimental approach. Experiment started by coupling the pump light into the waveguide where the position of the incident beam was monitored with the CCD camera above the sample. This initial settings enabled observation of some SH signal that did not necessarily match the most intense phase matching point. This adjustment usually excited phase matching points with higher order y - modes. They have lower efficiency but may be observed as well. In the next step fine setup adjustments were done, which include positioning the sample with respect to the pump beam, adjustment of the out-coupling lens and optimization of the beam path to the spectrograph. The SH signal was constantly monitored until the strongest signal was obtained. It is assumed that the described procedure leads to the observation of the

correct phase matching point with zero order modes in y-direction. According to the observations this procedure was relatively easy executable for phase matching interactions with high conversion efficiency and well separated wavelengths from other interactions.

Fig. 6.3.7 shows SH response to the excitation spectra with central wavelengths changing from 880 nm to 930 nm in 10 nm steps. A very strong and relatively broad

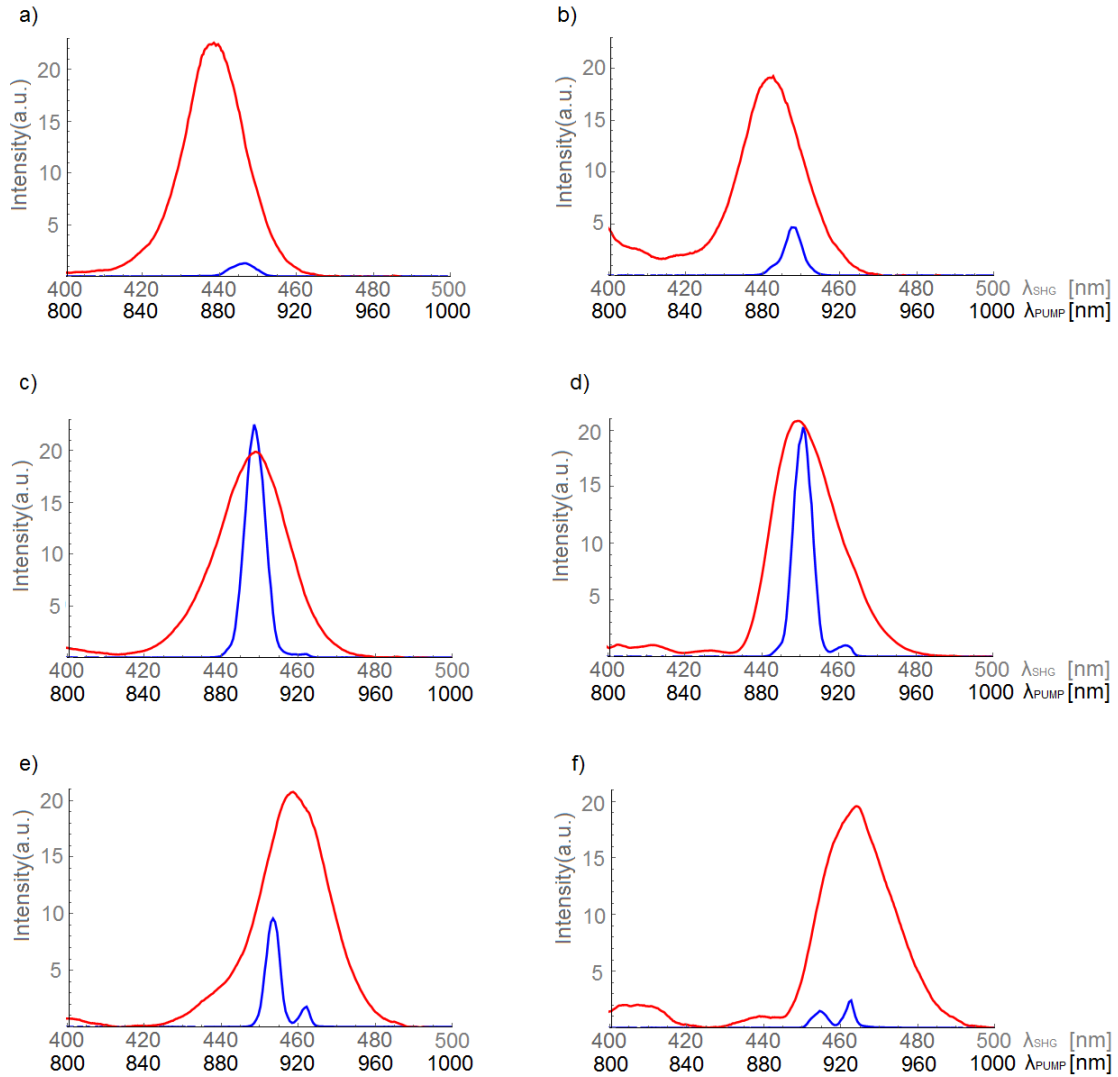


Figure 6.3.7: Measured SH response in the 590 nm thick and 5 μm wide rectangular AlN LPS waveguide with 10 μm periodicity. Excitation spectrum (red) with the central wavelengths varied from 880 nm to 930 nm and the SH response (blue curve). The high intensity SH peak occurs at 450 nm and a lower intensity SH peak at 462 nm.

SH peak was detected at around 450 nm accompanied by lower intensity SH peak at around 462 nm. According to calculation results presented in Fig. 6.3.1 the SH peak at 450 nm originates from the interaction between the fundamental pump and SH

modes, $2\text{TM}_0^\omega \rightarrow \text{TM}_0^{2\omega}$, where $N = 3$. SH peak at 462 nm fits to the combination of first order pump modes and second order SH mode, $2\text{TM}_1^\omega \rightarrow \text{TM}_2^{2\omega}$, where $N = 3$. The presented SHG measurements were done by maximizing the SH signal at 450 nm. The relative intensity between the two peaks changed if the position of the incident beam was displaced with respect to the waveguide. This observation is in favour of the theory predicting that the two SH peaks at 450 nm and 462 nm are the consequences of two different pump mode combinations.

In the pump wavelength range between 780 nm to 880 nm some low intensity SH signal was observed but no SH peak could be maximized by using the procedure described above.

Next excitation interval shows phase matched SHG as a response to the pump spectra with center wavelengths from 740 nm to 780 nm in Fig. 6.3.8. A strong

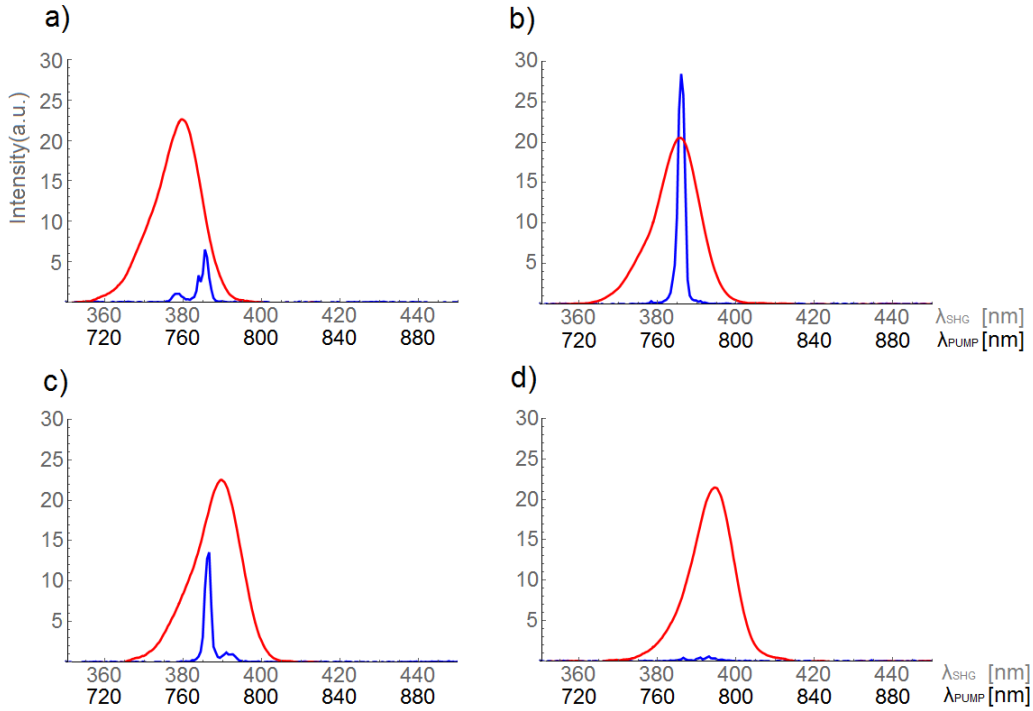


Figure 6.3.8: SH signal (blue) obtained in the 590 nm thick and 5 μm wide LPS-based AlN waveguide with 10 μm periodicity while scanning the center excitation wavelength from 750 nm to 780 nm (red). A phase matched SH peak appears at 385 nm.

and narrow SH peak appears at 385 nm. According to the predictions in Fig. 6.3.2 the closest phase matched interactions are due to the two processes, the first is $\text{TM}_0^\omega + \text{TM}_1^\omega \rightarrow \text{TM}_1^{2\omega}$ of the order $N = 5$ predicted at 376 nm and the second is $2\text{TM}_1^\omega \rightarrow \text{TM}_2^{2\omega}$ of the order $N = 5$ predicted at 373 nm. The efficiency calculated from Eq. 6.3.1 is higher for the first process. Besides that, it is more likely that the excitation efficiency is higher as well due to the used width of the Gaussian beam fitting better to the spatial beam profile of the pump mode combination $\text{TM}_0 + \text{TM}_1$

than 2TM_1 (see Fig. 6.3.2). There are some lower intensity side peaks that occur on each side of the main peak. Similarly as before, their excitation could be enhanced by changing the beam position. They are believed to be the consequences of some higher order y-mode combinations of the rectangular waveguide.

Finally, SH response was measured to the pump spectra with central wavelengths from 680 - 740 nm and is shown in Fig. 6.3.9. The three SH peaks occur at 370 nm, 355 nm and 350 nm. Again we refer to Fig. 6.3.2 to find the corresponding phase matching interactions. The origins of the observed SH response can be only roughly related to the predictions. The SH peak at 370 nm (shown in a) and b)) could be the consequence of the process $2\text{TM}_0^\omega \rightarrow \text{TM}_0^{2\omega}$ of the order $N = 4$ and predicted at 372 nm, or $2\text{TM}_1^\omega \rightarrow \text{TM}_2^{2\omega}$ of the order $N = 5$, predicted at 374 nm. In the vicinity of SH peak detected at 355 nm (shown in c)) no phase matching is theoretically expected. A peak at 350 nm (shown in e) and f)) is assumed to originate from the process $2\text{TM}_1^\omega \rightarrow \text{TM}_2^{2\omega}$ of the order $N = 6$, which is predicted at 342 nm. SH signal at 340 nm was the lowest observable wavelength and is shown in Fig. 6.3.9 g). Note the low intensity compared to other SH peaks.

To summarize, several SH peaks were detected in rectangular LPS-based waveguides and are listed in Table 6.1. Each peak is assigned to the phase matched mode

λ_{SH} [nm]	$(p, r; s; N)$
462	(1, 1; 2; 3)
450	(0, 0; 0; 3)
385	(0, 1; 1; 5) (1, 1; 2; 5)
370	(0, 0; 0; 4) (1, 1; 2; 5)
355	/
350	(1, 1; 2; 6)

Table 6.1: SH peaks observed in 10 μm periodic LPS-based AlN rectangular waveguide. The corresponding suggestions for the phase matched interactions between the modes $(p, r; s)$ of the order N are listed in the second column. The second suggestion for the 385 nm and 370 nm peaks is less probable.

combination $(p, r; s; N)$ that best explains its origin according to theoretical analysis presented in Section 6.3.1. In case where more than one explanation is possible the first one listed is more probable. After all, from the several phase matching possibilities shown in Fig.6.3.2 not all of them were detected or just could not be extracted from the many higher order y-mode interactions that took place. Note that among the odd QPM interactions only the lowest efficiency process, $2\text{TM}_1^\omega \rightarrow \text{TM}_0^{2\omega}$ of the order $N = 9$, and predicted at 403 nm was not detected. On the contrary, even order QPM interactions were almost absent except of SH peak at 350 nm. This observa-

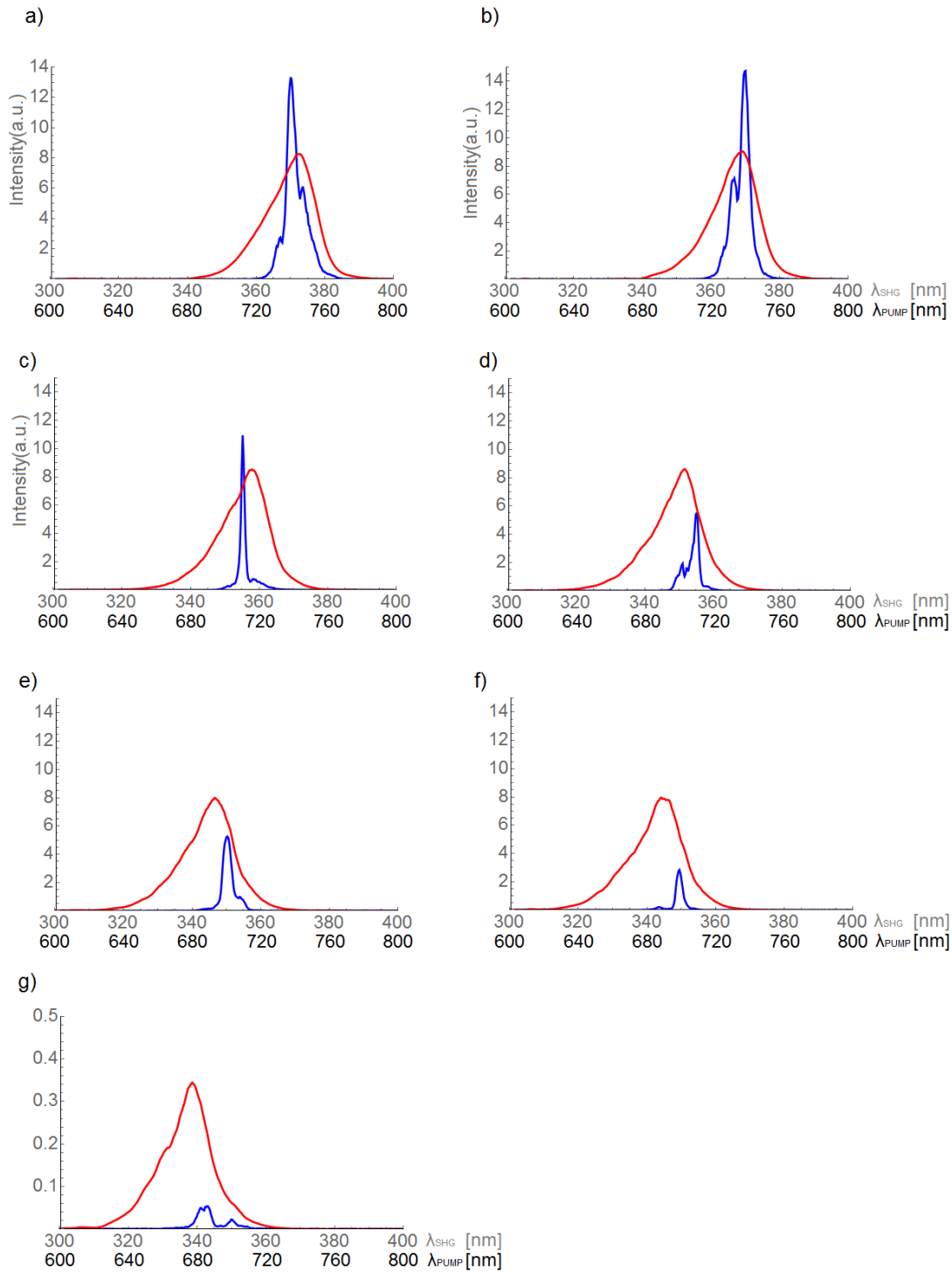


Figure 6.3.9: SH response in the 590 nm thick and 5 μm wide LPS-based AlN rectangular waveguide with 10 μm periodicity. Excitation spectrum (red) with the central wavelengths varied from 680 nm to 740 nm (red). SH peaks appear at 370 nm, 355 nm and 350 nm.

tion lead us to the conclusion that the duty cycle of the LPS waveguides was close to 50:50.

6.3.4 Measurements using planar 10 μm periodic structured waveguides

Light propagating in planar waveguides experiences less attenuation due to the absence of the sidewalls. In addition light may propagate in a better approximation of planar waveguide modes. Contrary to the assumption that the large beam size at the rectangular waveguide front surface prevents the formation of the higher order modes in y-direction, this was not the case in our sample. The higher order modes can be excited due to the irregularities of the front surface or can develop within the waveguide due to the surface roughness that could couple light to these undesired modes. Therefore, the comparison of the results measured in 10 μm periodicity LPS planar and rectangular waveguides enables the separation of QPM points that occur due to the interaction between higher order modes of rectangular waveguide.

The planar waveguides were grown on the same wafer as the rectangular waveguides, therefore their thickness is the same, (500-600) nm. The length of the planar waveguide was determined by the sample preparation: a diamond pen was used to inscribe lines parallel to the LPS domains at the back side of the wafer. In the following step waveguides were cleaved obtaining around 1 mm long pieces that were used in the experiment.

For SHG experiment the appropriate beam size entering the planar waveguide have to be considered. Since the planar waveguide modes are infinite in one direction, they are well enough approached with the Gaussian beam that is well collimated during the propagation distance. In order to achieve that, the in-coupling lens with 100 mm focal length was used so that the beam waist diameter in the focal point was around 30 μm . The evolution of the Gaussian beam width inside the planar waveguide is governed by the following equation

$$w^2(z) = w_0^2 \left(1 + \left(\frac{z\lambda}{\pi w_0^2} \right)^2 \right), \quad (6.3.2)$$

where w_0 is the radius of the beam waist and λ light wavelength inside the waveguide. From this relation the beam radius at the rear side of the waveguide is calculated. Inserting the values $w_0 = 15 \mu\text{m}$, pump wavelength $\lambda = 900 \text{ nm}$ and AlN refractive index $n = 2.0$, the beam size after propagation distance of 1 mm equals $w = 17.8 \mu\text{m}$. The change of the beam width after propagating through 1 mm long waveguide is negligibly small therefore planar approximation can be used.

Fig. 6.3.10 shows HeNe light coupling and propagation in the planar waveguide. By changing the beam position with respect to the front waveguide surface in horizontal direction, light propagates at different angles within the waveguide due to the roughness of the front surface. The entire front surface area was therefore scanned and the smoothest part was chosen for SHG measurements.

SHG measurements were performed in the pump wavelength range with central wavelengths ranging from 680 nm to 950 nm. The same spectral interval was used

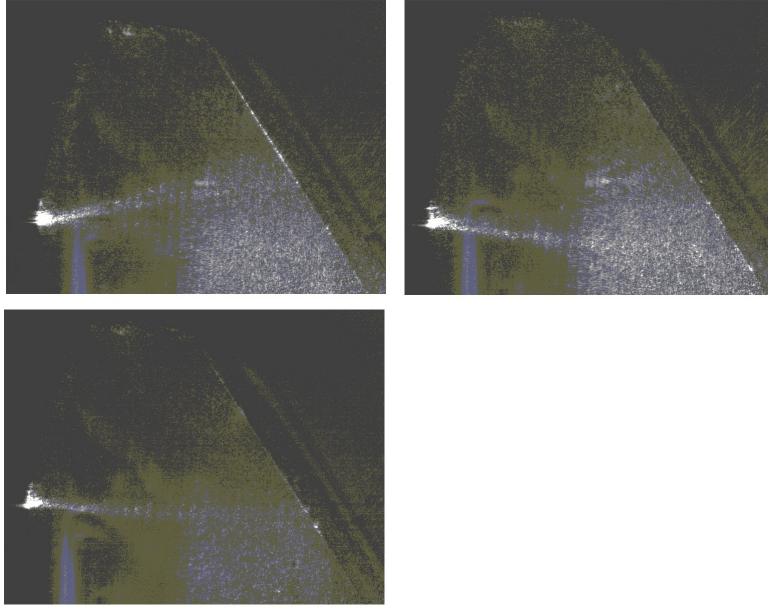


Figure 6.3.10: Light coupling into the planar 590 nm thick AlN waveguide with 10 μm periodicity. The HeNe light impinges from the left and due to the surface imperfections refracts at different angles.

in case of the rectangular waveguides with equal thickness in order to compare the results. Due to the described issues regarding the roughness of the front surface of the planar waveguides, the SH response was not so clear as expected. More than just the calculated number of SH peaks occurred and their intensity changed if the beam was displaced in y -direction. These results can be attributed to the change of the LPS periodicity that is experienced by the parts of the beam that refract at different angles at end surface imperfections. The phase matching points are therefore shifted to longer or shorter wavelengths. Since SH signal depends on the front surface shape, the relations between the measurements and theoretical predictions were hindered.

However, an unambiguous SH response was found to the pump spectra with central wavelengths ranging from 880 nm to 910 nm and is presented in Fig. 6.3.11. Two SH peaks are detected at 450 nm and 462 nm. In cases a) - d) the beam position was adjusted such that the SH peak at 450 nm is maximized. According to the Fig.6.3.2 it originates from the process $2\text{TM}_0^\omega \rightarrow \text{TM}_0^{2\omega}$ of the order $N = 3$. In case e) -h) the position of the beam was changed in order to maximize the SH peak at 462 nm belonging to the phase matched process $2\text{TM}_1^\omega \rightarrow \text{TM}_2^{2\omega}$ of the order $N = 3$.

To revise, two SH peaks were detected in planar 10 μm periodic LPS-based AlN waveguides and are listed in the Table 6.2 with the assigned QPM interactions. In fact, both of the SH peaks were observed in rectangular waveguide of equal thickness, which additionally confirms their origin.

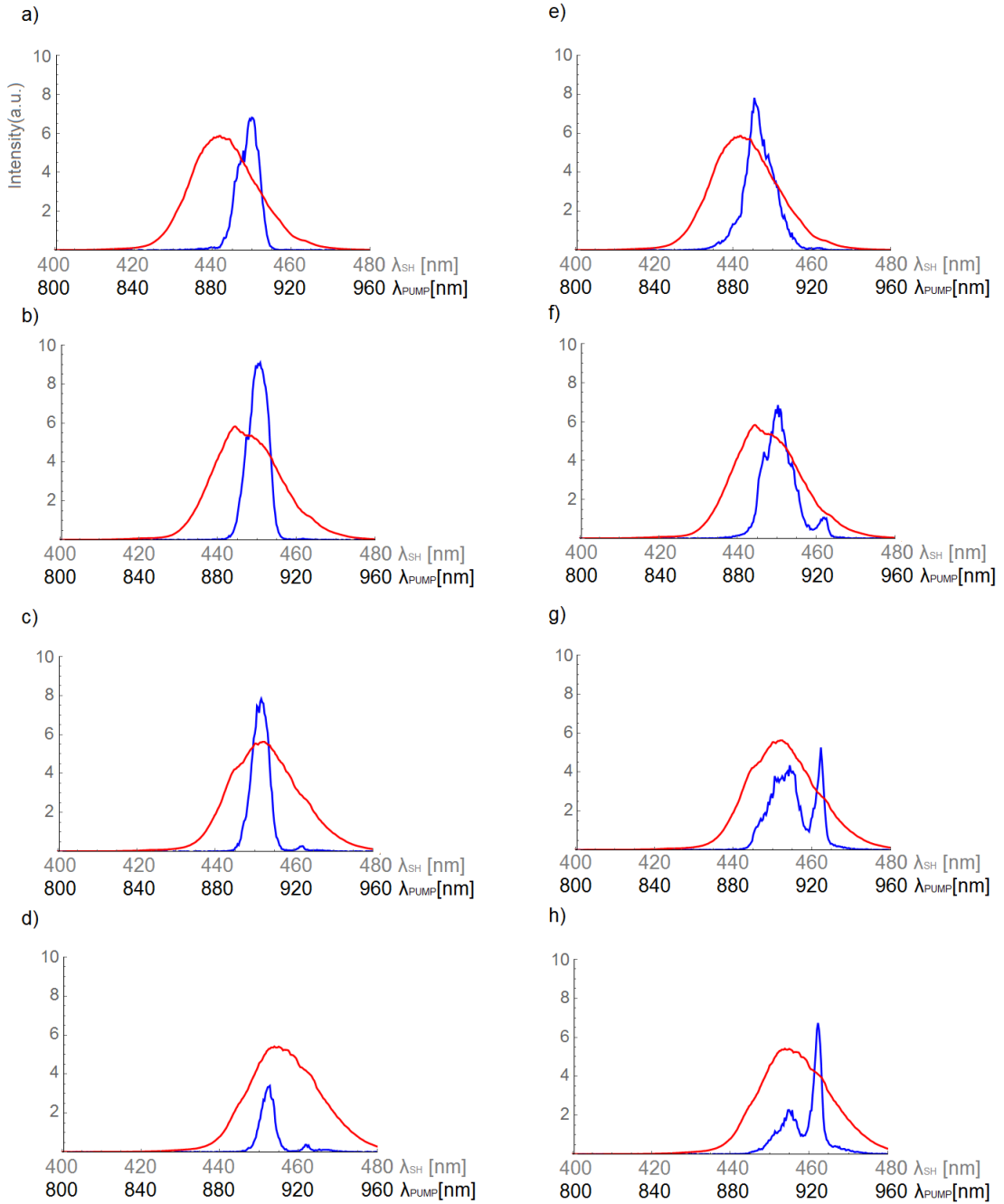


Figure 6.3.11: SH spectra as a function of pump wavelength and sample adjustment. In case a) - d) beam position was adjusted such that the SH peak at 450 nm was maximized, whereas the other set of measurements e) - h) shows the maximization of the SH peak at 462 nm. The used 10 μm periodic LPS-based AlN waveguide was 590 nm thick.

λ_{SH} [nm]	$(p, r; s; N)$
462	(1, 1; 2; 3)
450	(0, 0; 0; 3)

Table 6.2: SH peaks observed in 10 μm periodic LPS-based AlN planar waveguide and were assigned to the mode combinations. Both SH interactions were measured in rectangular waveguides listed in Table 6.1.

6.3.5 Theoretical predictions for 1.2 μm periodic structured waveguides

SHG into deep UV spectral range through the first order QPM between the fundamental pump and SH waveguide modes requires short periodicities of the order of a micrometer. Therefore 1.2 μm periodic, 550 nm thick and 5 μm wide rectangular LPS AlN waveguides were fabricated. The theoretical predictions for phase matching in planar waveguide with periodicity and thickness matching the produced waveguides are presented in Fig. 6.3.12. Two lowest order pump modes can propagate and the corresponding dispersions of n_{eff} and of their mean value are plotted with red. There are four SH modes of the orders $s = 0, 1, 2, 3$ shown with blue curves that are phase matched through first order QPM. The crossing points show phase matched interactions $(0, 0; s)$ where the ones with prominent overlap integrals are marked with circles. The most efficient conversion corresponds to the process $2\text{TM}_0^\omega \rightarrow \text{TM}_0^{2\omega}$ predicted to convert light wavelength of 554 nm into 277 nm.

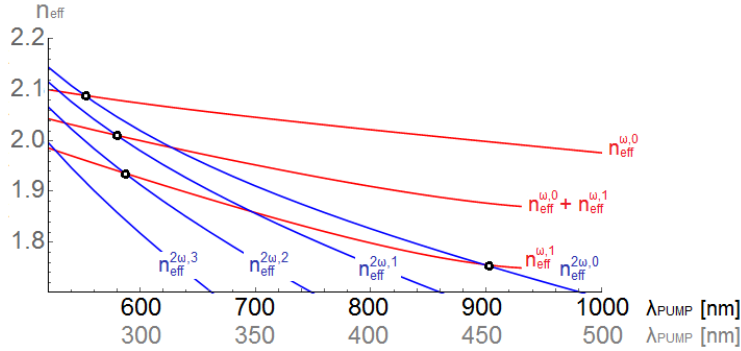


Figure 6.3.12: Phase matching points in 550 nm thick LPS-based AlN waveguide with 1.2 μm periodicity. Refractive index dispersions for the two lowest order pump waveguide modes and their mean value are presented with red curves. The dependences $n_{\text{eff}}^{2\omega,s} - \lambda/2\Lambda$ for the four lowest order SH modes, $s = 0, 1, 2, 3$, are plotted blue. At the crossing points first order quasi phase matching takes place where the four efficient interactions are labeled with circles.

6.3.6 Measurements using $1.2 \mu\text{m}$ periodic structured AlN waveguides

To prepare the samples with appropriate length I used diamond pen to inscribe and then cut the sample into the desired shape. Waveguides of different lengths from few micrometers to 1 mm were obtained.

Before attempting to measure SHG HeNe light was coupled into the waveguides and attenuation was observed. Over propagation distances of 1 mm no visually detected light was out-coupled. In Fig. 6.3.13 HeNe light is in-coupled from the left. The lower graph shows scattered intensity profile. The attenuation constant obtained from the exponential fit to the scattering intensity profile is $\alpha = (23 \pm 4)/\text{mm}$.

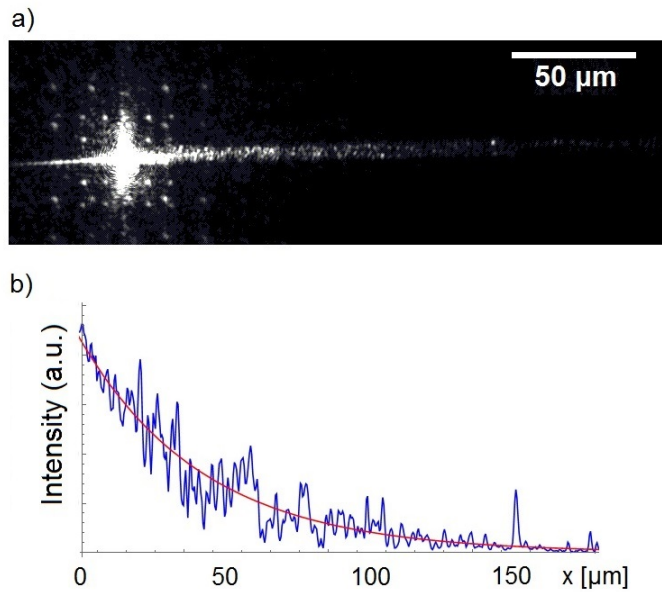


Figure 6.3.13: a) Top view image of an 550 nm thick and $10 \mu\text{m}$ wide LPS-based AlN waveguide with $1.2 \mu\text{m}$ periodicity. b) Scattered light intensity integrated over the waveguide width as a function of a propagation distance (blue) and fitted exponential function with attenuation coefficient $\alpha = (23 \pm 4)/\text{mm}$.

In these waveguides the attempts to measure SHG included the following improvements in comparison with previous measurements. The setup alignment procedure as described previously in section 5.3 where a HeNe was used to trace the beam-path could not be performed because the intensity of the out-coupled light was too low to be visually detected and fed to the detector system. In order to overcome this issue the setup was extended with additional HeNe laser "2" and a flip mirror "2" as seen in Fig. 6.3.14. The following procedure was used to increase the accuracy of the beam alignment. I used a test waveguide with low losses to align the HeNe laser "1" so that light was fed to the detector system. I marked the out-coupled beam path with the two pinholes "2". Then the HeNe laser "2" was directed through the two pinholes "2" in reverse direction by using the flip mirror "2". The sample was

then replaced by the $1.2 \mu\text{m}$ periodic LPS AlN waveguide whose xyz position was adjusted in order to couple the light from HeNe laser "2" into the desired waveguide from the rear end. With this alignment I assured the correct beam path from the waveguide rear end to the detection system. Flip mirror "2" was moved out of the lightbeam and the in-coupling with HeNe "1" was adjusted without moving the sample according to the common alignment procedure. Finally the tunable femtosecond laser was used for the SHG measurements but despite the beam path optimization no SH signal was detected.

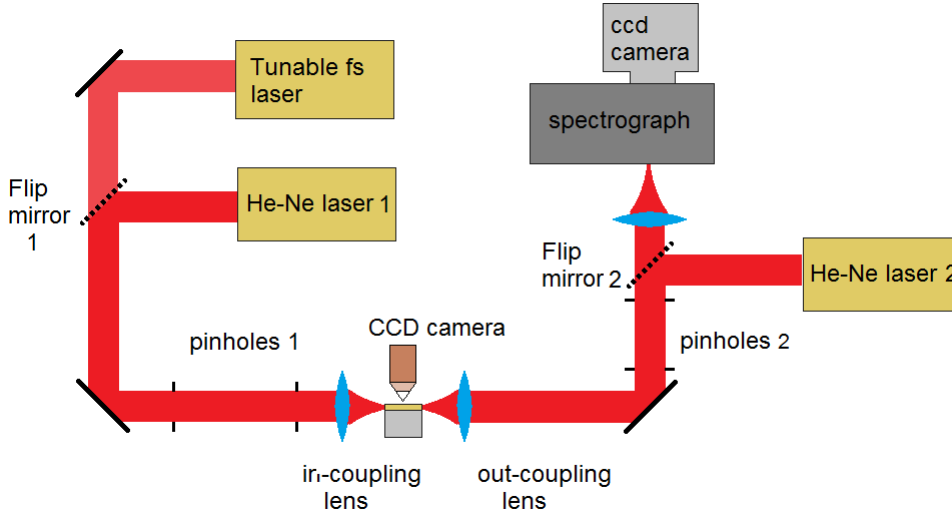


Figure 6.3.14: The setup for the optimization of the beam path from the sample to the detector system.

6.4 Discussion

An explanation is necessary to account for the observed spectral shapes of the SH peaks. As shown in Section 4.4 spectral width of the SH signal depends on the dispersion of propagation constants of the interacting waveguide modes, pump pulse width, waveguide length and propagation losses. The three SH peaks measured in single polar AlN waveguides have $\Delta\lambda_{\text{FWHM}}$ of around 1.5 - 2 nm. The very narrow spectral width is in accordance with the low propagation losses and large propagation distance (3 mm). Both measured and calculated values of spectral widths are displayed in Table 6.3. For the calculations Eq. 4.5.13 was used, which describes SH power as a function of frequency. From this relation $\Delta\omega_{\text{FWHM}}$ was obtained as a difference between the frequencies at which power drops to half of its maximum, which can be converted to wavelength units as $\Delta\lambda_{\text{FWHM}} = 2\pi c_0 / (2\omega_0)^2 \Delta\omega_{\text{FWHM}}$. The dispersions of the propagation constants of the waveguide modes (p, r; s) were used to calculate phase mismatch, defined as $\Delta K(\omega_2) = \Delta\beta'(\omega_2 - 2\omega_0) + \Delta\beta''(\omega_2 - 2\omega_0)^2$, pulse duration was $\tau = 30$ fs and waveguide length $L = 3$ mm. In the case of single

polar waveguides the measured values $\Delta\lambda_{\text{FWHM}}$ are close to the spectral resolution of the spectrograph, and consequently the comparison with the predicted values is unreasonable.

λ_{SH} [nm]	$(p, r; s)$	$\Delta\lambda_{\text{FWHM}}$ [nm]	$\Delta\beta'$ [ns/m]	$\Delta\beta''$ [s ² /m]	β_1'' [s ² /m]	$\Delta\lambda'_{\text{FWHM}}$ [nm]
355	(0, 0; 2)	1.5	1.67	$2.5 \cdot 10^{-25}$	$1.8 \cdot 10^{-25}$	0.11
336	(0, 1; 3)	2	2.12	$3.0 \cdot 10^{-25}$	$3.7 \cdot 10^{-25}$	0.21
306	(1, 1; 4)	1.5	2.8	$6.4 \cdot 10^{-25}$	$14 \cdot 10^{-25}$	0.17

Table 6.3: Spectral widths of the SH peaks in single polar AlN waveguides obtained from the experimental data, $\Delta\lambda_{\text{FWHM}}$, and the calculated values, $\Delta\lambda'_{\text{FWHM}}$. The parameters $\Delta\beta'$, $\Delta\beta''$ and β_1'' were obtained from the propagation constant dispersion relations of the modal phase matched waveguide modes (p, r; s), the pulse duration was $\tau = 30$ fs and waveguide length $L = 1$ mm.

In rectangular LPS-based AlN waveguides with 10 μm periodicity the measured SH signal was broader. The comparison between the measured and calculated values of SH spectral widths is shown in Table 6.4. The SH peaks at 462 nm, 450 nm and 385 nm have $\Delta\lambda_{\text{FWHM}}$ of around 3 nm, 7 nm and 3 nm, respectively. The calculations carried out for the processes $2\text{TM}_0^\omega \rightarrow \text{TM}_0^{2\omega}$ with $N = 3$ at 450 nm, $2\text{TM}_1^\omega \rightarrow \text{TM}_2^{2\omega}$ with $N = 3$ at 462 nm and $\text{TM}_0^\omega + \text{TM}_1^\omega \rightarrow \text{TM}_1^{2\omega}$ with $N = 5$ at 360 nm result in $\Delta\lambda'_{\text{FWHM}} = (3.9, 1.0, 1.7)$ nm, respectively. It is evident that measured values are larger than calculated, which can be attributed to the propagation losses that additionally broaden the SH spectrum. However, the size order of the measured spectral widths agrees quite well with the theoretical predictions.

λ_{SH} [nm]	$(p, r; s; N)$	$\Delta\lambda_{\text{FWHM}}$ [nm]	$\Delta\beta'$ [ns/m]	$\Delta\beta''$ [s ² /m]	β_1'' [s ² /m]	$\Delta\lambda'_{\text{FWHM}}$ [nm]
462	(1, 1; 2; 3)	3	0.6	$23 \cdot 10^{-24}$	$1.0 \cdot 10^{-24}$	1.0
450	(0, 0; 0; 3)	7	1.1	$5 \cdot 10^{-24}$	$51 \cdot 10^{-24}$	3.9
385	(0, 1; 1; 5)	3	0.2	$40 \cdot 10^{-24}$	$9.2 \cdot 10^{-24}$	1.7

Table 6.4: The measured and calculated spectral widths of the SH peaks in LPS-based AlN waveguides denoted by $\Delta\lambda_{\text{FWHM}}$ and $\Delta\lambda'_{\text{FWHM}}$, respectively. The calculations were carried using the dispersions of the propagation constants of the interacting modes (p, r; s), $\tau = 30$ fs and $L = 1$ mm.

Chapter 7

Conclusions

The motivation of this thesis was to devise a compact light source emitting in the deep UV spectral region, that would be useful in numerous technological applications. The idea was to exploit a process of optical second harmonic generation, where a visible laser generates frequency doubled light in the UV region. A widebandgap semiconductor material AlN was implemented as a frequency doubling crystal due to its suitable linear and nonlinear optical characteristics. Waveguide geometry for SHG was selected because high optical quality films of AlN can be grown on sapphire with thicknesses in the range of micrometers and less. In addition, appropriate structuring the substrate stimulates the growth of crystal domains with reversed polarity that can be used for preparing waveguides permitting quasi-phase-matched SHG.

Single polar waveguides were fabricated first. A thickness of 550 nm was selected as a compromise between thicker waveguides that facilitate in-coupling of light and thinner ones with lower number of waveguide modes. Three UV peaks were observed in the frequency doubling experiments with femtosecond pulses. They occurred at wavelengths of 356 nm, 331 nm and 306 nm, and were assigned to phase matching among various waveguide modes that could be well explained by the presented theoretical model for modal dispersion phase matching using the measured refractive index dispersion of the bulk materials. Good agreement between the experimental results and theory confirms the validity of the used theoretical model and the feasibility to employ AlN for the UV laser light generation.

The same thickness was selected in production process giving structured AlN waveguides with 10 μm periodicity. Two different waveguide geometries, rectangular and planar, were used. Several SH peaks were observed in rectangular waveguides in the visible and UV spectral region with minimum wavelength of 350 nm. Two of the SH peaks with highest conversion efficiencies were observed in both planar and rectangular waveguides. The theoretical model including higher order quasi phase matching interactions was used for the interpretation of the resulting SH peaks. By using 1.2 μm periodic structured AlN waveguides, SHG could not be measured due to the high scattering losses.

As shown above, AlN waveguides were demonstrated to be suitable for optical second harmonic generation into the UV spectral region. It is worth to emphasize that this was the first time quasi phase matched SHG was observed in AlN material.

The future work should be focused on minimizing the scattering losses in structured AlN waveguides, especially for short period structures.

In conclusion, we can estimate the performance of the laser based on second harmonic generation in AlN waveguides with negligible propagation losses. For the purpose of the realistic applications the used pump laser would be a continuous wave laser emitting at a wavelength suitable for phase matching. A rectangular waveguide with a $0.5 \mu\text{m} \times 2 \mu\text{m}$ front surface could be used for SHG based on modal phase matching between the modes $(p, r; s) = (0, 0; 2)$ at around 600 nm of pump wavelength. The pump laser emitting at that wavelength with power of 100 mW would be used. The conversion efficiency in such a waveguide grows quadratically with waveguide length and is plotted in Fig. 7.0.1 with blue. For a reasonable waveguide length, i.e. $L = 1 \text{ cm}$, the efficiency increases to around 0.5 %. Similarly, the structured AlN waveguide of the same dimension with $1.5 \mu\text{m}$ periodicity can be used for the conversion of 600 nm light into 300 nm as a consequence of the process $(p, r; s) = (0, 0; 0)$ of the first QPM order. By considering the same pump laser as above the conversion efficiency is plotted as a function of waveguide length in Fig. 7.0.1 with red. The estimated efficiency is around 5 % at $L = 1 \text{ cm}$.

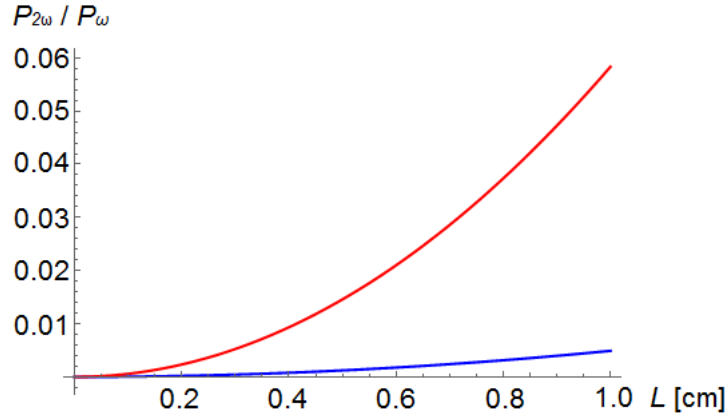


Figure 7.0.1: Efficiency $P^{2\omega}/P^{\omega}$ of the second harmonic generation as a function of waveguide length L for modal phase matching (blue) and quasi phase matching (red). Rectangular AlN waveguide is taken to be $0.5 \mu\text{m}$ thick and $2 \mu\text{m}$ wide. Continuously wave pump laser emitting at 600 nm with 100 mW optical power is considered.

Chapter 8

Extended abstract in Slovene

Razširjen povzetek v slovenskem jeziku

8.1 Uvod

Pričujoče doktorsko delo je rezultat sodelovanja med Univerzo v Severni Karolini in Univerzo v Ljubljani. Povezali smo se, da bi združili znanje iz področja gojenja kristalov in nelinearne optike s ciljem izdelati kompaktni laserski izvor v UV spektralnem območju. UV svetlobo smo pridobili s procesom optičnega podvajanja frekvence svetlobe, to je nelinearne optične pretvorbe vidnega laserja v UV svetlobo. Na ta način se izognemo nekaterim izzivom, s katerimi se srečuje prevladujoča tehnologija izdelave direktnih UV laserjev, kot so visoka črpalna moč, velika občutljivost na defekte v kristalu, površinska hrapavost itd.

Izmed primernih materialov ima aluminijev nitrid (AlN) vse potrebne linearne in nelinearne optične lastnosti za generacijo UV svetlobe. Je polprevodnik z direktno energijsko režo 6.2 eV (pri 300 K), zaradi česar je prepusten vse do valovne dolžine 200 nm. Kristalizira v treh fazah, pri čemer je termodinamsko najstabilnejša "wurtzite" kristalna struktura, prikazana na sliki 8.1.1. Ker nima centra inverzije, ima neničelno optično susceptibilnost drugega reda in je zato primeren za frekvenčno podvajanje svetlobe. AlN ima tri neničelne nelinearne koeficiente drugega reda, d_{15} , d_{31} in d_{33} , med katerimi je slednji največji z eksperimentalno določeno vrednostjo $d_{33} = 4 \text{ pm/V}$ [28].

AlN lahko gojimo v obliki tankih filmov na safirnem substratu, nastala struktura pa za svetlobo predstavlja optični valovod. Prednost uporabe valovoda je v tem, da svetloba v njem potuje brez divergence in s tem ohranja veliko intenziteto na območju sredice, kar je pomembno za učinkovito nelinearno pretvorbo. Obstajata dve različni orientaciji rasti, N-polarna in Al-polarna, prikazani na sliki 8.1.1. Pri N-polarnem kristalu kaže kristalografska c-os v isto smer kot normala na površino substrata, pri III-polarnem pa v nasprotno smer. Lahko pa gojimo tudi obe polarnosti na istem substratu in tako dobimo moduliran oz. strukturiran valovod. Konfiguracija tako dobljene modulacije je določena s predhodnjo obdelavo substrata. III-polaren AlGaN zraste na temperaturno obdelani nukleacijski plasti, medtem ko N-polaren AlGaN

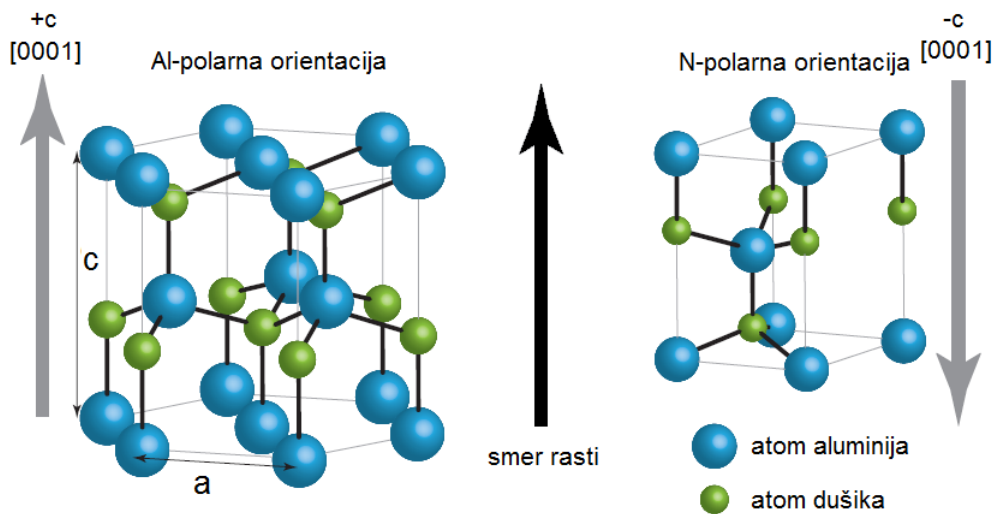


Figure 8.1.1: Wurtzite kristalna struktura aluminijevega nitrida z dvema možnima orientacijama. Al-polarna ($+c$ orientacija) ima kristalografsko c -os poravnano vzporedno s smerjo rasti, medtem ko je N-polarna konfiguracija dobimo z rotacijo za 180° ($-c$ orientacija).

zraste na safirju, ki je bil predhodno obdelan z dušikom. Visoko kvalitetni tanki AlN filmi so bili narejeni s tehniko nanašanja iz plinastih virov dušika (NH_3) in spojine z Al ($\text{C}_6\text{H}_{18}\text{Al}_2$). Strokovnjaki na tem področju so člani skupine Widebandgap iz Severne Karoline, ki so vseskozi razvijali in nas preskrbeli z vzorci. Podrobnosti o tehnikah rasti so navedene v literaturi [21, 22, 25].

Za doseganje visokih izkoristkov frekvenčnega podvajanja svetlobe je ključno ujemanje faz med svetlobnima valoma pri osnovni in podvojeni frekvenci. Žal konvencionalne tehnike ujemanja faz ne moremo uporabiti v tankih AlN filmih. Najučinkovitejša metoda je kvazi fazno ujemanje, ki uporabi periodično modulacijo nelinearnega koeficienta v kristalu, kar je doseženo v prej omenjenem strukturiranem AlN valovodu. S tem dosežemo relativno ujemanje faze v ponavljajočih intervalih, ne da bi se pri tem ujemali fazni hitrosti osnovne in podvojene svetlobe.

V nadaljevanju sledi strnjen opis propagacije svetlobe v valovodih, nato pa optično frekvenčno podvajanje znotraj valovodov. Na kratko opišem dve tehniki za doseganje faznega ujemanja, prva je metoda na podlagi disperzije valovodnih načinov, druga pa kvazi fazno ujemanje. Sledi opis eksperimenta za nelinearni odziv v AlN valovodih in rezultati meritev.

8.2 Optični valovodi

Optični valovodi so strukture, ki omogočajo vodenje svetlobe v optičnem spektru. Najpreprostejši je planarni valovod, skiciran na sliki 8.2.1, kjer je svetlobno valovanje omejeno le v eni dimenziji. Sestavljen je iz treh plasti dielektrikov: sredice z največjim

lomnim količnikom $n_2 = \sqrt{\varepsilon_2}$, ki je umeščena med dve plasti z manjšima lomnima količnikoma, substrat z $n_1 = \sqrt{\varepsilon_1}$ in zrak z $n_3 = \sqrt{\varepsilon_3}$. Oblike elektromagnetnega

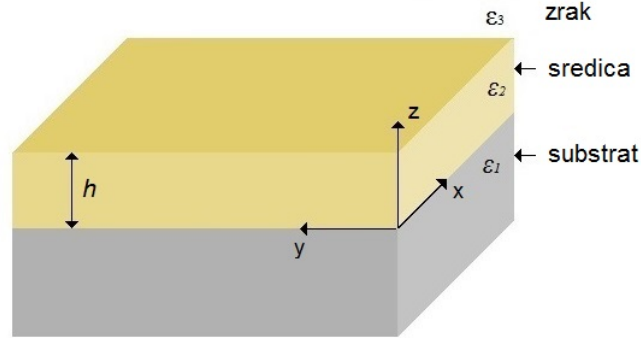


Figure 8.2.1: Planarni valvod sestavlja sredica debeline h , substrat in zrak. Dielektrična konstanta sredice mora biti večja od preostalih dveh dielektričnih konstant, $\varepsilon_2 > \varepsilon_1, \varepsilon_3$.

polja, ki se propagirajo po valvodu, poiščemo z uporabo Maxwellovih enačb. Za homogen in izotropen material z dielektrično in magnetno konstanto ε in μ izpeljemo valovno enačbo

$$\nabla^2 \mathbf{E} - \frac{\mu\varepsilon}{c_0^2} \frac{\partial^2 \mathbf{E}}{\partial t^2} = 0 \quad \text{in} \quad \nabla^2 \mathbf{H} - \frac{\mu\varepsilon}{c_0^2} \frac{\partial^2 \mathbf{H}}{\partial t^2} = 0, \quad (8.2.1)$$

kjer je \mathbf{E} električno in \mathbf{H} magnetno polje. Obstajata dve vrsti neodvisnih rešitev, TE imajo neničelne komponente E_y , H_x and H_z , in TM s komponentami H_y , E_x and E_z . Zanimajo nas rešitve pri določeni frekvenci ω , ki se propagirajo v smeri x . V tem primeru je nastavek za polja \mathbf{E} in \mathbf{H} enak

$$\begin{aligned} \mathbf{E}(x, z) &= \mathbf{E}_0 \psi(z) e^{i(\beta x - \omega t)}, \\ \mathbf{H}(x, z) &= \mathbf{H}_0 \psi(z) e^{i(\beta x - \omega t)}, \end{aligned} \quad (8.2.2)$$

kjer sta \mathbf{E}_0 in \mathbf{H}_0 polarizacijska vektorja električnega in magnetnega polja, β je propagacijska konstanta, $\psi(z)$ pa brezdimenzijska funkcija, ki opisuje prečno porazdelitev elektromagnetnega polja. Navadno uvedemo še efektivni lomni količnik n_{eff} z zvezo

$$\beta = k_0 n_{\text{eff}}, \quad (8.2.3)$$

kjer je $k_0 = \omega/c_0$ valvni vektor svetlobe v vakuumu. Upoštevati moramo še robne pogoje za polja na mejah med sredstvi, iz česar izpeljemo, da je možno le diskretno število vrednosti n_{eff} , ki predstavljajo omejene rešitve. Tem rešitvam pravimo valvodni rodovi, in jih označimo z m . Najnižjemu rodu pravimo osnovni rod in mu pripišemo $m = 0$, sledijo mu $m = 1, m = 2, \dots$. Število rodov je odvisno od debeline valvoda h , frekvence ω in lomnih količnikov n_1, n_2 in n_3 .

8.3 Podvajanje svetlobe v optičnih valovodih

Podvajanje svetlobe je nelinearen optični proces, pri čemer svetloba s frekvenco ω interagira s snovjo in pri tem generira svetlobo s podvojeno frekvenco 2ω . Ta proces postane merljiv le pri zadosti velikih optičnih intenzitetah. Za opis tega pojava zapišemo polarizacijo snovi v odvisnosti od električne poljske jakosti kot

$$P_i = P_i^L + P_i^{\text{NL}} = \varepsilon_0 \chi_{ij}^{(1)} E_j + \varepsilon_0 \chi_{ijk}^{(2)} E_j E_k + \varepsilon_0 \chi_{ijkl}^{(3)} E_j E_k E_l + \dots, \quad (8.3.1)$$

kjer je E_i i-ta komponenta trenutnega električnega polja, koeficienti $\chi_{ij}^{(1)}$, $\chi_{ijk}^{(2)}$ in $\chi_{ijkl}^{(3)}$ pa so susceptibilnosti prvega, drugega in tretjega reda. Za opis frekvenčnega podvojevanja svetlobe je potreben razvoj do drugega reda, ki jo opisuje tenzor $\chi_{ijk}^{(2)}$, višje člene v vrsti pa zanemarimo.

Elektromagnetna polja, ki opisujejo podvajanje svetlobe v valovodih, so rešitve Maxwellovih enačb, kjer moramo kot rečeno upoštevati polarizacijo snovi do drugega reda. V približku izotropne snovi brez prostih nabojev izpeljemo valovno enačbo z nelinearnim členom

$$\nabla^2 \mathbf{E}(\mathbf{r}, t) - \frac{\varepsilon}{c_0^2} \frac{\partial^2 \mathbf{E}(\mathbf{r}, t)}{\partial t^2} = \mu_0 \frac{\partial^2 \mathbf{P}^{\text{NL}}(\mathbf{r}, t)}{\partial t^2}, \quad (8.3.2)$$

kjer je \mathbf{E} električno polje, \mathbf{P}^{NL} nelinearna polarizacija snovi, μ_0 magnetna permeabilnost vakuumu, $\varepsilon = 1 + \chi^{(1)}$ pa dielektrična konstanta. Rešitve linearne valovne enačbe, ki smo jih poimenovali valvodni rodovi, uporabimo kot nastavek za reševanje nelinearne valovne enačbe 8.3.2, s tem da je amplituda EM polj odvisna od x-koordinate. V splošnem se lahko valovanje pri osnovni frekvenci ω propagira v obliki kombinacije več rodov. Za frekvenčno podvajanje so ključne interakcije dveh v splošnem različnih rodov, ki ju označimo z indeksoma p in r, ki prispevata k nastanku valvodnega rodu z indeksom s pri frekvenci 2ω . Izračun nam pove, da je gostota optične moči (to je optična moč na enoto dolžine v y-smeri, ker je v tej smeri valovanje neomejeno) pri frekvenci 2ω enaka

$$P_{2\omega}^s(x) = \frac{64\omega^2 d_{33}^2 n_{\text{eff}}^{\omega,p} n_{\text{eff}}^{\omega,r}}{9\pi^2 h \varepsilon_0 c_0^3 (n_{\text{eff}}^{2\omega,s})^3 \varepsilon_{\omega}^4} P_{\omega}^p P_{\omega}^r \Gamma_{p,r;s} \text{sinc}^2(\Delta\beta_{p,r;s} x) x^2, \quad (8.3.3)$$

Definirali smo

$$\Delta\beta_{p,r;s} = \beta_{2\omega}^s - \beta_{\omega}^p - \beta_{\omega}^r, \quad (8.3.4)$$

ki opisuje razliko propagacijskih konstant med rodovi p, r in s. Za neničelno vrednost $\Delta\beta_{p,r;s}$ moč niha med vrednostjo 0 in neko pozitivno vrednostjo. V posebnem primeru, $\Delta\beta_{p,r;s} = 0$, pa moč narašča s kvadratom razdalje x . Druga pomembna količina je integral prekrivanja

$$\Gamma_{p,r;s} = \frac{9\pi^2}{16h^2} \left[\int_0^h \psi_{\omega}^p(z) \psi_{\omega}^r(z) \psi_{2\omega}^s(z) dz \right]^2 \quad (8.3.5)$$

ki nam pove efektivno prostorsko prekrivanje med valvodnimi rodovi p, r in s. Je brez dimenzije in je normaliziran na 1, kadar so vsi trije interagirajoči rodovi osnovni

$(p, r; s) = (0, 0; 0)$ in se povsem prekrivajo. Za vse druge kombinacije rodov p, r in s pa ima vrednosti med 0 in 1. Za doseganje visokih izkoristkov je zaželjeno frekvenčno podvajanje med tistimi rodovi, ki imajo čimvečji prekrivalni integral.

8.3.1 Fazno ujemanje

Ujemanje faze je v večrodovnem valovnem vodniku možno doseči, če za izbrane rodove p, r in s velja enakost, $\Delta\beta_{p,r;s} = 0$, pravimu mu fazno ujemanje na podlagi disperzije valovnih načinov. V tem primeru $P_{2\omega}^s(x)$ narašča s kvadratom x-koordinate kot

$$P_{2\omega}^s(x) = \frac{64\omega^2 d_{33}^2 n_{\text{eff}}^{\omega,p} n_{\text{eff}}^{\omega,r}}{9\pi^2 h \varepsilon_0 c_0^3 (n_{\text{eff}}^{2\omega,s})^3 \varepsilon_\omega^4} P_\omega^p P_\omega^r \Gamma_{p,r;s} x^2, \quad (8.3.6)$$

Pogoj za fazno ujemanje lahko izrazimo z efektivnimi lomnimi količniki in dobimo

$$n_{\text{eff}}^s(\lambda/2) = \frac{n_{\text{eff}}^p(\lambda) + n_{\text{eff}}^r(\lambda)}{2}. \quad (8.3.7)$$

Poudariti je treba, da zaradi disperzije tovrstnega faznega ujemanja ni mogoče doseči za poljubne rodove p, r in s . V materialih z normalno disperzijo lahko dosežemo fazno ujemanja le, če velja pogoj

$$p \leq r < s \quad \text{ali} \quad p < r \leq s. \quad (8.3.8)$$

Drug način faznega ujemanja se da doseči v materialih s periodično prostorsko modulacijo nelinearnega optičnega koeficienta. V tako pripravljenem materialu se potem faze osnovnega in podvojenega vala ujamejo na vsakem periodičnem intervalu. Temu načinu pravimo kvazi-fazno ujemanje. V tem primeru lahko izpeljemo za pogoj faznega ujemanja enakost

$$\Delta\beta_{p,r;s} = \frac{2\pi N}{\Lambda}, \quad (8.3.9)$$

pri čemer je $N = 1, 3, 5..$ in opisuje red kvazi faznega ujemanja, Λ pa je perioda modulacije nelinearnega koeficienta. Za optično moč frekvenčno podvojene svetlobe dobimo izraz

$$P_{2\omega}^{s,N}(L) = \frac{256\omega^2 d_{33}^2 n_{\text{eff}}^{\omega,p} n_{\text{eff}}^{\omega,r}}{9N^2 \pi^4 h \varepsilon_0 c_0^3 \varepsilon_\omega^4 (n_{\text{eff}}^{2\omega,s})^3} P_\omega^p P_\omega^r \Gamma_{p,r;s} L^2. \quad (8.3.10)$$

Prednost kvazi faznega ujemanja je v tem, da lahko dosežemo fazno ujemanje med katerokoli kombinacijo valovodnih rodov. Posebej zaželjeno je ujemanje med osnovnimi rodovi pri prvotnem in podvojenem valovodnem rodu, torej $(p, r; s) = (0, 0; 0)$, kjer je generacija frekvenčno podvojene svetlobe najučinkovitejša. Če zapišemo pogoj za kvazi fazno ujemanje 8.3.11 z efektivnimi lomnimi količniki, dobimo

$$n_{\text{eff}}^s(\lambda/2) - N \frac{\lambda}{2\Lambda} = \frac{n_{\text{eff}}^p(\lambda) + n_{\text{eff}}^r(\lambda)}{2}, \quad (8.3.11)$$

kjer je λ valovna dolžina osnovnega vala. Zveza 8.3.11 ima v primerjavi z zvezo 8.3.7 dodaten člen $N \frac{\lambda}{2\Lambda}$ na levi strani enačbe. Torej lahko z ustrezno nastavitvijo periode Λ določimo valovno dolžino svetlobe, pri kateri bo potekalo frekvenčno podvajanje.

8.3.2 Meritve frekvenčnega podvajanja v AlN valovodih

Eksperimentalna postavitve sistema za merjenje nelinearnega odziva v AlN valovodih je predstavljena na sliki 8.3.1. Kot izvor svetlobe sem uporabila femtosekundni laser-

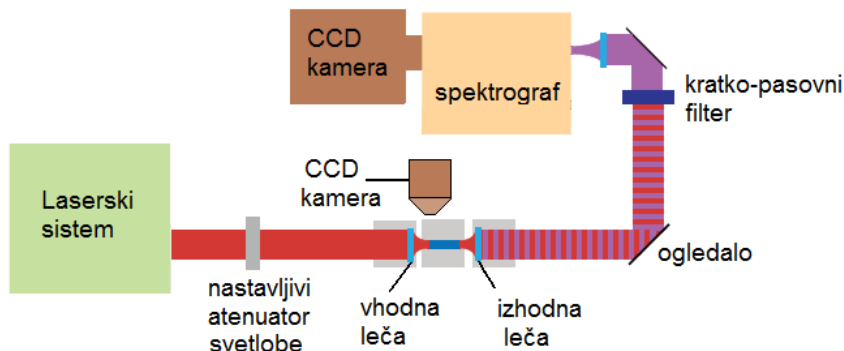


Figure 8.3.1: Eksperimentalna postavitve za merjenje nelinearnega odziva v AlN valovodih.

ski sistem s nastavljivo valovno dolžino. Svetlobo sem sklopila v valvod s pomočjo vhodne leče, tako da je sfokusiran žarek vpadel na prednjo ploskev valvoda. Za opazovanje sklopitve svetlobe sem nad stojalo z vzorcem namestila CCD kamero. Iz valvoda izhajajoč žarek sem s pomočjo izhodne leče kolimirala in ga napeljala do detektorskega sistema, sestavljenega iz spektrografa in CCD kamere.

Prve meritve nelinearnega odziva sem opravila na Al-polarnih AlN valovodih. Pravokotni valvodi so bili visoki 550 nm, široki $5 \mu m$ in dolgi 3 mm. Možne kombinacije faznega ujemanja na podlagi disperzije valovnih načinov so prikazane na sliki 8.3.2. Na x-osi so nanešene valovne dolžine osnovne in frekvenčno podvojene svetlobe, na y-osi pa efektivni lomni količnik valvodnih rodov. Slika prikazuje n_{eff} za dva najnižja rodova pri osnovni frekvenci in njuno povprečje (rdeče). Disperzije n_{eff} za podvojeno frekvenco pa so prikazane za prvih pet najnižjih rodov (modro). Fazno ujemanje, $\Delta\beta_{p,r,s} = 0$, je doseženo pri valovnih dolžinah, kjer se rdeča in modra krivulja sekata. Izmed vseh presešišč so tri z največjim izkoristkom pretvorbe označena s krogci.

Rezultati meritev so prikazani na sliki 8.3.3. V spektru frekvenčno podvojene svetlobe so trije vrhovi pri valovnih dolžinah 306 nm, 331 nm and 356 nm, ki se ujemajo s procesi $2 TM_1^\omega \rightarrow TM_4^{2\omega}$, $TM_0^\omega + TM_1^\omega \rightarrow TM_3^{2\omega}$ in $2 TM_0^\omega \rightarrow TM_2^{2\omega}$, v istem vrstnem redu. Na sliki Fig. 8.3.2 so označeni s krogci. Vzbujevanje ničtega in prvega valvodnega rodu osnovne frekvence sem dosegla z majhnim premikom vhodne leče v smeri z.

Naslednje eksperimente frekvenčnega podvajanja svetlobe sem opravila na strukturiranih AlN valvodih z $10 \mu m$ periodo. V teh valvodih je fazno ujemanje možno kot kombinacija kvazi faznega ujemanja in faznega ujemanja na podlagi disperzije valovnih načinov. Ti valvodi so bili zaradi modulirane strukture na površini bolj hrapavi, zaradi česar so bile propagacijske izgube večje kot pri enopolarnih valvodih. Posledično sem pripravila malo krajše valvode dolžine 1 mm. Pravokotni valvodi

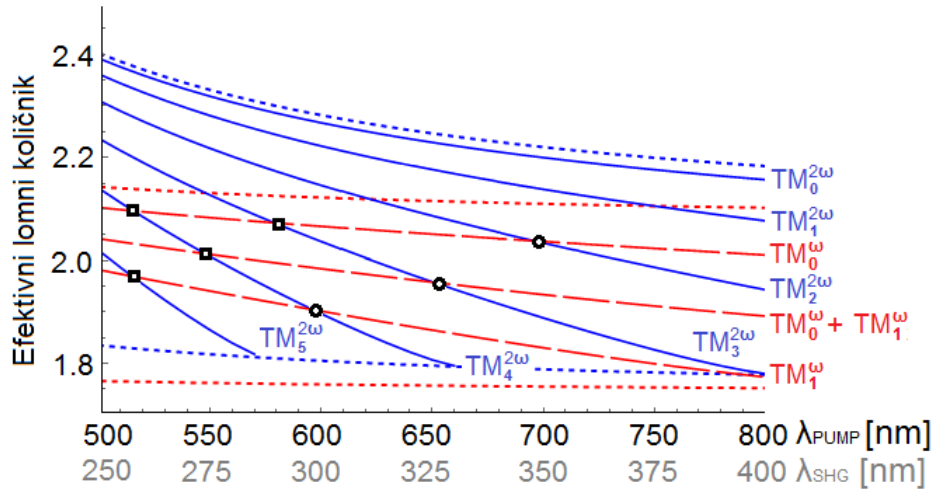


Figure 8.3.2: Disperzije n_{eff} za osnovne (rdeče krivulje) in frekvenčno podvojene (modre krivulje) valovodne rodove v planarnem AlN valovodu debeline 550 nm. Črtkane črte predstavljajo disperzijo izrednega lomnega količnika AlN in safirja. Na mestih, kjer se modra in rdeča krivulja sekata, je izpolnjen pogoj faznega ujemanja. Črni krogi označujejo interakcije z relativno velikim prekrivalnim integralom, ki so bile tudi eksperimentalno izmerjene. Ostale interakcije, označene s kvadratici, pa imajo zanemarljivo majhne prekrivalne integrale.

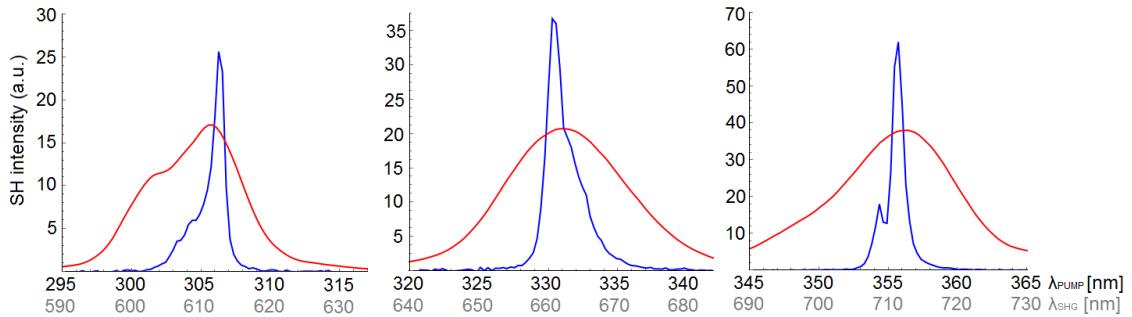


Figure 8.3.3: Spekter frekvenčno podvojenega valovanja v pravokotnem Al-polarnem AlN valovodu debeline 550 nm and širine $10 \mu\text{m}$ pri treh različnih vzbujevalnih centralnih valovnih dolžinah. Modre krivulje prikazujejo spekter frekvenčno podvojene svetlobe, rdeče krivulje pa spekter osnovne svetlobe.

so bili debeli približno 590 nm in široki $5 \mu\text{m}$. Izračunane napovedi za fazno ujemanje so prikazane na sliki 8.3.4. Pri tem je bil uporabljen približek planarnega valovoda debeline 590 nm.

Z merjenjem nelinearnega odziva sem opazila več vrhov v spektru frekvenčno podvojene svetlobe, ki so prikazani na sliki 8.3.5. Primer a) kaže močan signal pri 450 nm, zraven pa še šibkejši signal pri 462 nm. Primerjava z izračuni na sliki 8.3.4 nakazuje, da je vrh pri 450 nm posledica interakcije $2\text{TM}_0^\omega \rightarrow \text{TM}_0^{2\omega}$ reda $N = 3$,

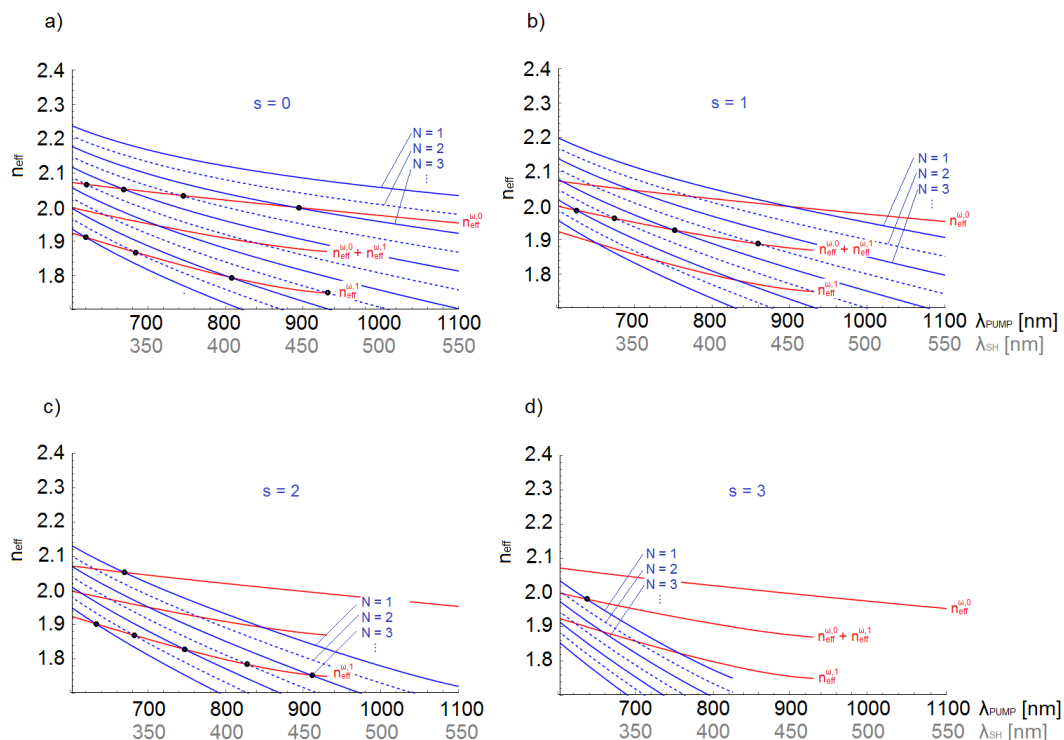


Figure 8.3.4: Dispersijske krivulje za strukturirane AlN valovode s periodo $10 \mu m$ in debelino 590 nm . Rdeče krivulje se nanašajo na disperzije valovnih načinov pri osnovni frekvenci, modre pa prikazujejo odvisnost $n_{\text{eff}}^s - N \frac{\lambda}{2\Lambda}$ za prve štiri rodove ($s = 0, 1, 2, 3$) pri dvojni frekvenci (od a) do d)), kjer se vsak izmed rodov sklaplja z osnovno-frekvenčnim rodom preko različnih redov N kvazi faznega ujemanja. Črtkane modre krivulje označujejo sode, polne modre krivulje pa lihe vrednosti N .

drugi vrh pri 462 nm pa ustreza kombinaciji $2 \text{ TM}_1^\omega \rightarrow \text{TM}_2^{2\omega}$ reda $N = 3$. Relativna intenziteta med omenjenima vrhovoma se je spremenila s spreminjanjem položaja vpadnega svetlobnega snopa glede na valovod. To opažanje ni presenetljivo, saj sta vrhova pri 450 nm in 462 nm posledici dveh različnih kombinacij rodov pri osnovni frekvenci. Naslednji vrh po padajoči valovni dolžini sem izmerila pri 385 nm in je prikazan na sliki 8.3.5 b). Glede na teoretične napovedi se v bližini tega vrha nahajata dva procesa, prvi je $\text{TM}_0^\omega + \text{TM}_1^\omega \rightarrow \text{TM}_1^{2\omega}$ reda $N = 5$ pri 376 nm , drugi proces pa je $2 \text{ TM}_1^\omega \rightarrow \text{TM}_2^{2\omega}$ reda $N = 5$ pri 373 nm . Izkoristek prvega procesa je večji, poleg tega pa je tudi izkoristek vzbujevanja večji zaradi oblike snopa, ki se bolj ujema s kombinacijo $\text{TM}_0 + \text{TM}_1$ kot pa 2 TM_1 . Naslednji trije frekvenčno podvojeni vrhovi pri 370 nm , 355 nm in 350 nm so prikazani na slikah 8.3.5 c) - e). Signal pri 370 nm bi lahko bil posledica interakcije $2 \text{ TM}_0^\omega \rightarrow \text{TM}_0^{2\omega}$ reda $N = 4$, ki je napovedan pri 372 nm , ali pa $2 \text{ TM}_1^\omega \rightarrow \text{TM}_2^{2\omega}$ reda $N = 5$, z napovedjo pri 374 nm . V bližini vrha pri 355 nm ni po teoretični napovedi nobenega faznega ujemanja. Signal pri 350 nm pa je najverjetneje rezultat procesa $2 \text{ TM}_1^\omega \rightarrow \text{TM}_2^{2\omega}$ reda $N = 6$, ki je napovedan pri 342 nm .

Zaradi znatnih propagacijskih izgub v strukturiranih valovodih z $10 \mu m$ peri-

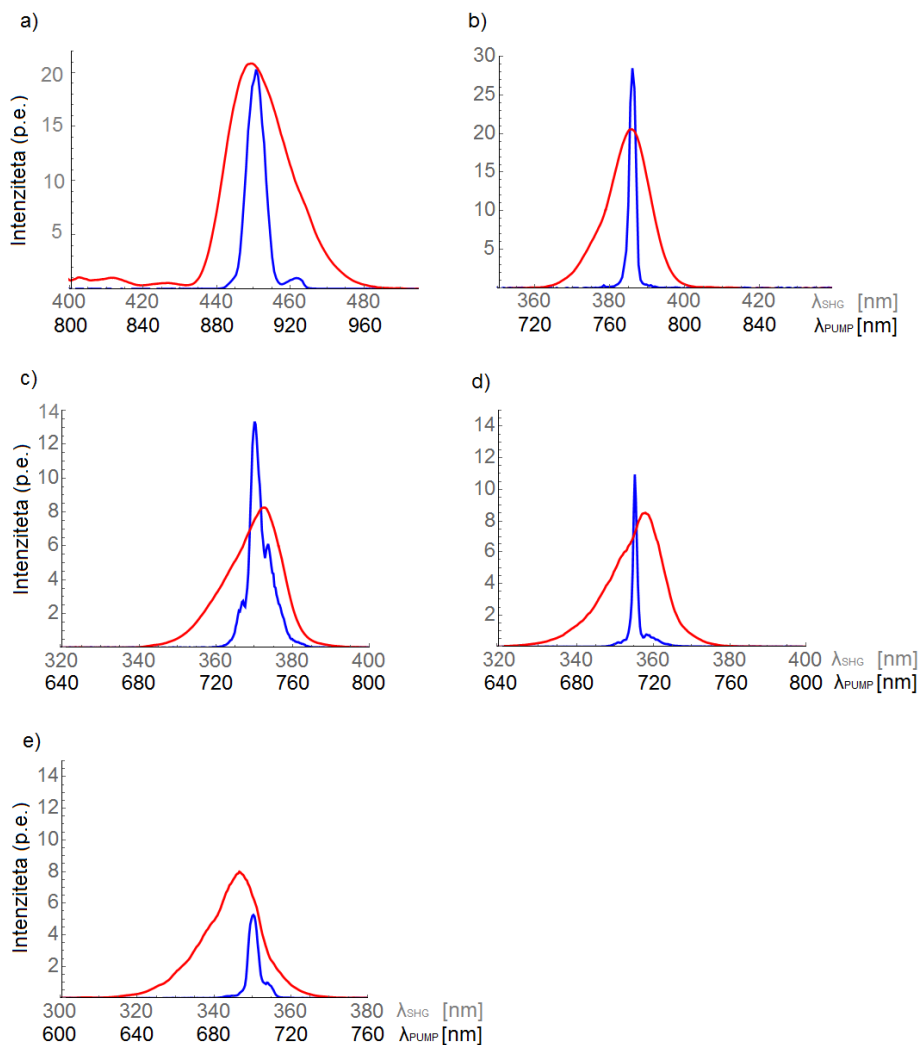


Figure 8.3.5: Signal frekvenčno podvojene svetlobe v 590 nm debelem in $5 \mu\text{m}$ širokem pravokotnem strukturiranem AlN valovodu z $10 \mu\text{m}$ periodo. Vzbujevalni spekter je označen z rdečo, spekter frekvenčno podvojene svetlobe pa z modro barvo. V spektru frekvenčno podvojenega signala se pojavijo vrhovi pri 462 nm, 450 nm, 385 nm, 370 nm, 355 nm, 350.

odo pravokotne oblike sem opravila nelinearne meritve tudi na planarnih valovodih. Planarani valovodi nimajo stranskih ploskev, zato pričakujemo manj sipanja svetlobe. Poleg tega pa se v pravokotnem valovodu lahko formirajo rodovi višjega reda v smeri y , ki ustvarijo nove pogoje za fazno ujemanje. Uporabljeni planarni valovodi so bili enake debeline 590 nm in dolžine 1 mm kot pravokotni valovodi. Meritve frekvenčnega podvajanja svetlobe so prikazane na sliki 8.3.6. Dva vrhova v spektru frekvenčno podvojene svetlobe se nahajata pri 450 nm in 462 nm. Na desni sliki je bil valovod glede na pozicijo žarka postavljen tako, da je bil maksimalen signal pri 462 nm, na levi sliki pa signal pri 450 nm. Po primerjavi s teoretičnimi napovedmi, prikazanimi na sliki 8.3.4 se vrh pri 450 nm ujema s procesom $2\text{TM}_0^\omega \rightarrow \text{TM}_0^{2\omega}$ reda

$N = 3$. Vrh pri 462 nm pa se ujema s procesom $2\text{TM}_1^\omega \rightarrow \text{TM}_2^{2\omega}$ reda $N = 3$. Oba vrhova sta bila izmerjena tudi v pravokotnem valovodu enake debeline, kar dodatno potrjuje skladnost s teoretičnimi napovedmi.

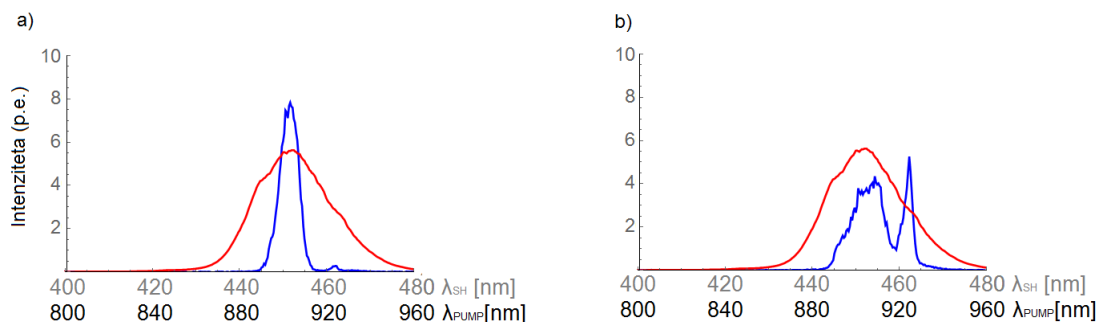


Figure 8.3.6: Signal frekvenčno podvojene svetlobe pri dveh različnih pozicijah valovoda glede na vpadno svetlobo. V primeru a) je pozicija vzorca takšna, tako da je bil vrh pri 350 nm maksimalen, primer b) pa prikazuje maksimalen signal pri 462 nm. Meritve so narejene na planarnem strukturiranem AlN valovodu z $10 \mu\text{m}$ periodo debeline 590 nm.

Nazadnje so bili izdelani strukturirani AlN valovodi s periodo $1.2 \mu\text{m}$, ki so primerni za generacijo UV svetlobe na podlagi kvazi faznega ujemanja osnovnih rodov pri osnovni in podvojeni frekvenci $(p, r; s) = (0, 0; 0)$ v prvem redu $N = 1$. Propagacijske izgube v teh valovodih so bile zaradi hrapavih stranskih ploskev prevelike, tako da frekvenčno podvojene svetlobe ni bilo mogoče detektirati.

8.3.3 Zaključek

V tem delu sem raziskovala potencial AlN za generacijo UV svetlobe s pomočjo procesa optičnega podvojevanja svetlobe. Izbrana je bila valovodna geometrija, saj lahko gojimo AlN v obliki tankih filmov na safirnem substratu. Poleg tega lahko z ustrezno pripravo substrata dosežemo periodično invertirano polarnost kristala, kar je omogočilo frekvenčno podvajanje na podlagi kvazi faznega ujemanja.

Začetne nelinearne meritve sem opravila s pomočjo najpreprostejših enopolarnih AlN valovodov. Debelina 550 nm je bila izbrana kot kompromis med debelejšimi valovodi, ki omogočajo lažje sklapljanje svetlobe v valovod in tanjšimi, ki dopuščajo manjše število valovodnih rodov. Izmerila sem tri vrhove v UV spektru podvojenega valovanja, in sicer pri valovnih dolžinah 356 nm, 331 nm in 306 nm. Detektirane vrhove sem pripisala faznemu ujemanju med različnimi valovodnimi rodovi, ki so razloženi s predstavljenim teoretičnim modelom za fazno ujemanje na podlagi disperzije valovnih načinov. Eksperimentalni rezultati se zelo dobro ujemajo s teoretičnimi napovedmi.

Enako debelino sem izbrala za izdelavo strukturiranih AlN valovodov z $10 \mu\text{m}$ periodo. Uporabila sem dve različni geometriji valovodov, planarno in pravokotno. Z uporabo pravokotnih valovodov sem izmerila več frekvenčno podvojenih vrhov tako

v vidnem kot v UV spektralnem območju do minimalne valovne dolžine 350 nm. Dva izmed vrhov z največjo učinkovitostjo pretvorbe sta bila opažena tako v planarnem kot v pravokotnem valovodu. Za interpretacijo rezultatov nelinearnih meritev sem uporabila teoretični opis, ki vključuje kvazi fazno ujemanje višjih redov. Nazadnje men meritve naredila še na strukturiranih AlN valovodih s periodo 1.2 μm , kjer pa zaradi velikih izgub frekvenčnega podvojevanja svetlobe ni bilo možno detektirati.

Na podlagi predstavljenih meritev lahko zaključimo, da je AlN primeren material za optično frekvenčno podvojevanje v UV spektralnem območju. Velja poudariti, da je bilo prvič s pomočjo AlN prikazano frekvenčno podvajanje svetlobe na podlagi kvazi faznega ujemanja. V nadaljevanju bi bilo raziskave potrebno usmeriti v zmanjševanje izgub zaradi sipanja v strukturiranih AlN valovodih, predvsem tistih s krajšimi periodami.

Za zaključek lahko ocenimo izkoristek laserja na podlagi frekvenčnega podvojevanje svetlobe v AlN valovodih z zanemarljivimi izgubami. V primeru realistične aplikacije bi uporabili kontinuiran monokromatski laser z valovno dolžino, ki ustreza faznemu ujemanju. Za primer vzemimo enopolarni AlN valovod s pravokotnim presekom $0.5 \mu m \times 2 \mu m$, ki ga lahko uporabimo za frekvenčno podvajanje svetlobe iz 600 nm v 300 nm na podlagi disperzije valovnih načinov med rodovi $(p, r; s) = (0, 0; 2)$. Kot izvor osnovnega valovanja bi uporabili laser z valovno dolžino 600 nm in močjo 100 mW. Izkoristek nelinearne pretvorbe v takem valovodu narašča kvadratno z dolžino valovoda kot je prikazano na sliki 8.3.7 z modro krivuljo. Pri dolžini val-

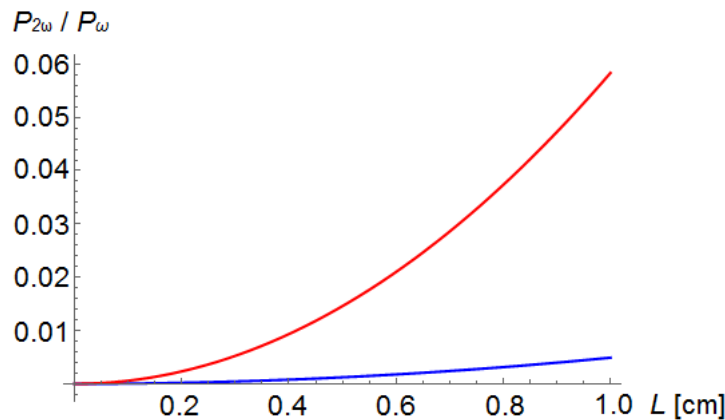


Figure 8.3.7: Efficiency $P^{2\omega}/P^{\omega}$ of the second harmonic generation as a function of waveguide length L for modal phase matching (blue) and quasi phase matching (red). Rectangular AlN waveguide is taken to be $0.5 \mu m$ thick and $2 \mu m$ wide. Continuous wave pump laser emitting at 600 nm with 100 mW optical power is considered.

ovoda enaki $L = 1 cm$ znaša izkoristek okoli 0.5 %. Podobno lahko uporabimo strukturiran AlN valovod enakih dimenzij s periodo modulacije $1.5 \mu m$, ki ga uporabimo za nelinearno pretvorbo svetlobe z valovno dolžino 600 nm v 300 nm kot posledico procesa $(p, r; s) = (0, 0; 0)$ na podlagi kvazi faznega ujemanja prvega reda. Kot izvor osnovnega valovanja uporabimo enak laser kakor v prejšnjem primeru, dobljena odvisnost izkoristka od dolžine valovoda pa je prikazana na sliki 7.0.1 z rdečo krivuljo. Pri

dolžini $L = 1 \text{ cm}$ je ocenjen izkoristek enak okoli 5 %.

Bibliography

- [1] Kneissl M., Rass J. *III-Nitride Ultraviolet Emitters: Technology and Applications*. Springer, New York (2015).
- [2] Morkoc, H. *Nitride Semiconductors and Devices*. Springer, New York (1999).
- [3] Rhodes, C. *Review of ultraviolet lasers*. IEEE J. Quantum Electron. **9** (6), 647 (1973)
- [4] R. Paschotta. *Encyclopedia of Laser Physics and Technology*. Wiley-VCH, Berlin, 1st edition, (2008).
- [5] T. Südmeyer et al. *Efficient 2nd and 4th harmonic generation of a single-frequency, continuous-wave fiber amplifier*. Opt. Express 16 (3), 1546 (2008).
- [6] Yim, W. M. et al. *Epitaxially grown AlN and its optical band gap*. J. Appl. Phys. **44**, 292–296 (1973).
- [7] Cox, G. A., Cummins, D. O., Kawabe, K. and Tredgold, R. H. *On the preparation, optical properties and electrical behaviour of aluminium nitride*. J. Phys. Chem. Solids **28**, 543–548 (1967).
- [8] Pankove, J. I., Maruska, H. P. and Berkeyheiser, J. E. *Optical Absorption of GaN*. Appl. Phys. Lett. **17**, 197–199 (1970).
- [9] Davydov, V. Y. et al. *Absorption and Emission of Hexagonal InN. Evidence of Narrow Fundamental Band Gap*. Phys. Status Solidi B **229**, r1–r3 (2002).
- [10] Nakamura, S., Mukai, T. and Senoh, M. *Candela-class high-brightness In-GaN/AlGaN double-heterostructure blue-light-emitting diodes*. Appl. Phys. Lett. **64**, 1687–1689 (1994).
- [11] Nakamura, S. et al. *InGaN-Based Multi-Quantum-Well-Structure Laser Diodes*. Jpn. J. Appl. Phys. **35**, L74–L76 (1996).
- [12] Taniyasu Y., Kasu M. and Makimoto T. *An aluminium nitride light-emitting diode with a wavelength of 210 nanometres*. Nature **441**, 325–328, (2006).

-
- [13] M. Kneissl, T. Kolbe, C. Chua, V. Kueller, N. Lobo, J. Stellmach, A. Knauer, H. Rodriguez, S. Einfeldt, Z. Yang, N. M. Johnson, and M. Weyers. *Advances in group III-nitride-based deep UV light-emitting diode technology*. Semiconductor Science and Technology, **26**(1), 014036, (2011).
- [14] A. J. Fischer, A. A. Allerman, M. H. Crawford, K. H. A. Bogart, S. R. Lee, R. J. Kaplar, W. W. Chow, S. R. Kurtz, K. W. Fullmer, and J. J. Figiel. *Room-temperature direct current operation of 290 nm light-emitting diodes with milliwatt power levels*. Applied Physics Letters, **84** (17), 3394, (2004).
- [15] J. P. Zhang, A. Chitnis, V. Adivarahan, S. Wu, V. Mandavilli, R. Pachipulusu, M. Shatalov, G. Simin, J. W. Yang, and M. Asif Khan. *Milliwatt power deep ultraviolet light-emitting diodes over sapphire with emission at 278 nm*. Applied Physics Letters, **81**(26), 4910, (2002).
- [16] T. Nishida, H. Saito, and N. Kobayashi. *Efficient and high-power AlGaIn based ultraviolet light-emitting diode grown on bulk GaN*. Applied Physics Letters, **79**(6), 711, (2001).
- [17] M. Kneissl, Z. Yang, M. Teepe, C. Knollenberg, O. Schmidt, P. Kiesel, N. M. Johnson, S. Schujman, and L. J. Schowalter. *Ultraviolet semiconductor laser diodes on bulk AlN*. Journal of Applied Physics, **101**(12), 123103, (2007).
- [18] H. Yoshida, M. Kuwabara, Y. Yamashita, Y. Takagi, K. Uchiyama, and H. Kan. *AlGaIn-based laser diodes for the short-wavelength ultraviolet region*. New Journal of Physics, **11**(12), 125013, (2009).
- [19] R. Collazo, S. Mita, J. Xie, A. Rice, J. Tweedie, R. Dalmau, and Z. Sitar. *Implementation of the GaN lateral polarity junction in a mesfet utilizing polar doping selectivity*. Physica status solidi (a), **207**(1), 45–48, (2010).
- [20] S.-R. Jeon, Z. Ren, G. Cui, J. Su, and M. Gherasimova. *Investigation of Mg doping in high-Al content p-type AlGaIn*. Applied Physics Letters, **86**(8), 082107–082103, (2005).
- [21] R. Dalmau, B. Moody, R. Schlessler, S. Mita, J. Xie, M. Feneberg, B. Neuschl, K. Thonke, R. Collazo, A. Rice, J. Tweedie, and Z. Sitar. *Growth and characterization of AlN and AlGaIn epitaxial films on AlN single crystal substrates*. Journal of The Electrochemical Society, **158**(5), H530, (2011).
- [22] J. Xie, S. Mia, R. Dalmau, R. Collazo, A. Rice, J. Tweedie, and Z. Sitar. *Ni/Au schottky diodes on Al_xGa_{1-x}N (0.7 < x < 1) grown on AlN single crystal substrates*. Physica Status Solidi (c), **8**(7-8), 2407–2409, (2011).
- [23] Yoshida et al. *Demonstration of an ultraviolet 336 nm AlGaIn multiple-quantum-well laser diode*. Appl. Phys. Lett. **93**, 241106 (2008).

BIBLIOGRAPHY

- [24] Rigler M. *Second Harmonic Generation in Blue and Ultraviolet Region Using AlGa_N waveguides*. Doctoral dissertation, (2014).
- [25] M. Rigler, J. Buh, M.P. Hoffmann, R. Kirste, M. Bobea, S. Mita, M. D. Gerhold, R. Collazo, Z. Sitar, and M. Zgonik. *Optical characterization of Al- and N-polar AlN waveguides for integrated optics*. Appl. Phys. Express **8**, 042603 (2015).
- [26] M. Rigler, M. Zgonik, M. P. Hoffmann, R. Kirste, M. Bobea, R. Collazo, Z. Sitar, S. Mita, and M. Gerhold. *Refractive index of III-metal-polar and N-polar AlGa_N waveguides grown by metal organic chemical vapor deposition*. Applied Physics Letters, **102**(22), 221106, 2013.
- [27] M. Rigler, T. Troha, W. Guo, R. Kirste, I. Bryan, M. D. Gerhold, R. Collazo, Z. Sitar, and M. Zgonik. *Second harmonic generation of blue light in GaN waveguides*. Submitted to Physica Status Solidi A (2017).
- [28] Majkič A., Franke A., Kirste R., Schlessler R., Collazo R., Sitar Z. and Zgonik M. *Optical nonlinear and electro-optical coefficients in bulk aluminium nitride single crystals*. Physica Status Solidi (b), 1700077, (2017).
- [29] Kirste, R. et al. *Polarity control and growth of lateral polarity structures in AlN*. Appl. Phys. Lett. **102**, 181913 (2013).
- [30] J. H. Park et. al. *Spatial mode behavior of second harmonic generation in a ridge-type waveguide with a periodically poled MgO-doped lithium niobate crystal*. Japanese Journal of Appl. Phys. **53**, 062201 (2014).
- [31] D. Blanc, A.M. Bouchoux, C. Plumereau, A. Cachard, and J.F. Roux *Phase-matching frequency doubling in an aluminum nitride waveguide with a tunable laser source*. Appl. Phys. Lett. **66**, 659 (1995).
- [32] D.B. Anderson and J.T. Boyd. *Wideband CO₂ Laser Second Harmonic Generation Phase Matched in GaAs Thin-Film Waveguides*. Appl. Phys. Lett. **19**, 266 (1971).
- [33] D. Duchesne et al. *Second harmonic generation in AlGaAs photonic wires using low power continuous wave light*. Opt. Express **19** (13), 12408-12417 (2011).
- [34] T. Troha, M. Rigler, D. Alden, I. Bryan, W. Guo, R. Kirste, S. Mita, M. D. Gerhold, R. Collazo, Z. Sitar, and M. Zgonik. *UV second harmonic generation in AlN waveguides with modal phase matching*. Opt. Mat. Express **6** (6), 2014-2023 (2016).
- [35] T. Sugita, K. Mizuuchi, Y. Kitaoka, K. Yamamoto. *31%-efficient blue second-harmonic generation in a periodically poled MgO:LiNbO₃ waveguide by frequency doubling of an AlGaAs laser diode*. Opt. Lett. **24** (22), 1590 (1999).

-
- [36] Y. L. Lee, W. Shin, B.-A. Yu, C. Jung, Y.-C. Noh, D.-K. Ko. *Mode tailoring in a ridge-tape periodically poled lithium niobate waveguide*. Opt Express, **18** (8), 7678, (2010).
- [37] S. Venugopal Rao, K. Moutzouris, M. Ebrahimzadeh. *Nonlinear frequency conversion in semiconductor optical waveguides using birefringent, modal and quasi-phase-matching techniques*. J. Opt. A, Pure Appl. Opt. **6** (6), 569-584 (2004).
- [38] Ananta R. Acharya. *Group III – Nitride Semiconductors: Preeminent Materials for Modern Electronic and Optoelectronic Applications*. The Himalayan Physics, **4**(4), 22-26 (2013).
- [39] F. Bernardini, V. Fiorentini, and D. Vanderbilt. *Spontaneous polarization and piezoelectric constants of III-V nitrides*. Physical Review B, **56** (16), R10024, (1997).
- [40] G. A. Slack, R. Tanzilli, R. O. Pohl, and J. W. Vandersande. *The intrinsic thermal conductivity of AlN*. Journal of Physics and Chemistry of Solids, **48** (7), 641, (1987).
- [41] Stutzmann, M. et al. *Playing with Polarity*. Phys. Status Solidi B **228**, 505–512 (2001).
- [42] Alden, D. et al. *Fabrication and structural properties of AlN submicron periodic lateral polar structures and waveguides for UV-C applications*. Appl. Phys. Lett. **108**, 261106 (2016).
- [43] A. Yariv, P. Yeh. *Optical Waves in Crystals*. John Wiley & Sons, Inc., (1984).
- [44] K. Kawano and T. Kitoh. *Introduction to Optical Waveguide Analysis: Solving Maxwell's Equation and the Schrodinger Equation*. Wiley-Interscience, New York, (2001).
- [45] Hunsperger R. G. *Integrated Optics*. Springer, New York (2009).
- [46] P.K. Tien. *Light waves in thin films and integrated optics*. Appl. Opt. **10**, 2395 (1971).
- [47] Marcuse D. *Mode Conversion Caused by Surface Imperfections of a Dielectric Slab Waveguide*. Bell Syst. Techn. J. **48**, 3187-3215 (1969).
- [48] Marcuse D. *Radiation Losses of Tapered Dielectric Slab Waveguides*. Bell Syst. Techn. J. **49**, 273-290, (1970).
- [49] Marcuse D. *Higher-order scattering losses in dielectric waveguides*. Bell Syst. Techn. J. **51**, 429-454 (1972).
- [50] P. A. Franken et al. *Generation of optical harmonics*. Phys. Rev. Lett. **7** (4), 118 (1961).

BIBLIOGRAPHY

- [51] Boyd R. *Nonlinear Optics*. Third Edition.pdf (2008).
- [52] Mills D. L. *Nonlinear Optics*. Springer-Verlag Berlin Heidelberg (1998).
- [53] Conwell E. *Theory of second harmonic generation in optical waveguides*. IEEE Journal of Quantum Electronics **9** (9), (1973).
- [54] Fejer M. et al. *Quasi-Phase-Matched Second Harmonic Generation: Tuning and Tolerances*. IEEE Journal of Quantum Electronics **28** (11), (1992).
- [55] Sidick E. et al. *Ultrashort-pulse second-harmonic generation*. J. Opt. Soc. Am. B, **12** (9), (1995).
- [56] Imeshev G. et al. *Ultrashort-pulse second-harmonic generation with longitudinally nonuniform quasi-phase-matching gratings: pulse compression and shaping*. Journal of the Opt. Society of America B, **17** (2), (2000).
- [57] Guo W. et. al. *KOH based selective wet chemical etching of AlN, Al_xGa_{1-x}N, and GaN crystals: A way towards substrate removal in deep ultraviolet light emitting diode*. Appl. Phys. Lett., **106**, 082110 (2015).
- [58] E. Marcatili. *Dielectric rectangular waveguide and directional coupler for integrated optics*. Bell Syst. Tech. J., **48**, 2071–2121, (1969).
- [59] M. Bass, V.N. Mahajan, and E.W. Van Stryland. *Handbook of Optics - Design, Fabrication, and Testing; Sources and Detectors; Radiometry and Photometry*. 3rd ed., McGraw-Hill, Inc., New York, (2010).
- [60] Alden D. *Periodic Lateral Polar Structure-based Waveguides in III-Nitrides for Quasi-Phase Matched Second Harmonic Generation*. Doctoral disertation, (2017).
- [61] Hite J. *Progress in periodically oriented III-nitride materials*. Journal of Crystal Growth (2016).
- [62] Liu et. al. *Direct observation of inversion domain boundaries of GaN on c-Sapphire at sub-angstrom resolution*. Advanced Materials *20*, 2162-2165 (2008).

List of publications

Papers:

1. T. Troha, M. Rigler, D. Alden, I. Bryan, W. Guo, R. Kirste, S. Mita, M. D. Gerhold, R. Collazo, Z. Sitar, and M. Zgonik. *UV second harmonic generation in AlN waveguides with modal phase matching*. Opt. Mat. Express **6** (6), 2014-2023 (2016).
2. M. Rigler, T. Troha, W. Guo, R. Kirste, I. Bryan, M. D. Gerhold, R. Collazo, Z. Sitar, and M. Zgonik. *Second harmonic generation of blue light in GaN waveguides*. Submitted to Physica Status Solidi A (2017).
3. D. Alden, W. Guo, R. Kirste, F. Kaess, I. Bryan, T. Troha, A. Bagal, P. Reddy, L.H. Hernandez-Balderrama, A. Franke, S. Mita, C.-H. Chang, A. Hoffmann, M. Zgonik, R. Collazo, and Z. Sitar *Fabrication and structural properties of AlN submicron periodic lateral polar structures and waveguides for UV-C applications*. Appl. Phys. Lett. **108**, 261106 (2016).
4. T. Troha, D. Alden, R. Collazo, Z. Sitar and M. Zgonik. *Quasi phase matched second harmonic generation in visible spectral region using AlN waveguides*. To be published (2017).

Conferences:

1. T. Troha, M. Rigler, M. Zgonik. *Linearna in nelinearna optična karakterizacija polarno kontroliranih AlGaIn valovodov za integrirano optiko*. 10. Konferenca fizikov v osnovnih raziskavah, Škofja Loka (2014).
2. T. Troha, M. Rigler, W. Guo, R. Kirste, S. Mita, R. Collazo, M. D. Gerhold, Z. Sitar and M. Zgonik. *UV second harmonic generation in AlN waveguides*. E-MRS spring meeting, Lille, France (2016).

Summer schools:

1. 8th International Summer School *New Frontiers in in Optical Technologies*, Tampere, Finland (2015).
2. Internation School *Photonic integration:advanced materials, new technologies and applications*, Erice, Italy (2016).